THE UNIVERSITY *of* EDINBURGH

On-board hydrogen production using multifunctional catalytic hollow fibre-based reactors

Simona Mazzone

THE UNIVERSITY *of* EDINBURGH

Thesis submitted for the degree of
Doctor of Philosophy

The University of Edinburgh

School of Engineering

Year of Submission 2022

Declaration of authorship

I hereby declare that this submission is entirely my work, in my own words, and that all sources used in researching it are fully acknowledged and all quotations properly identified. It has not been submitted, in whole or in part, in any previous application for a degree.

Simona Mazzone

Abstract

Faced with the imminent depletion of fossil resources and the large environmental impact associated with their use, the 21st century society demands a gradual change from an economy based on fossil sources to one based on sustainable resources and processes compatible with the environment. In this respect, green ammonia (NH_3) has been proposed as promising hydrogen (H_2) carrier candidate for on-board application. However, since on-board space constraints represent a significant challenge facing the adoption of NH_3 as a future fuel carrier, this work focused on the design and assessment of a pioneering technology for on-board H_2 production via NH_3 decomposition, *i.e.* multifunctional catalytic hollow fibre-based reactors.

Today, the most prominent technology for hydrogen production via NH_3 decomposition is a traditional catalytic packed bed reactor (PBR) that uses a precious metal-based catalyst. As a result, this expensive technology is outsized, thereby limiting its applicability to NH_3-fuelled vehicles. The use of hollow fibre-based reactors represents a unique opportunity for innovative solutions in the development of a suitable technology for the production of H_2 on-board. This is because they can overcome the limitations of traditional PBRs and allow for decreased required catalyst loading and/or the operating temperatures when compared with a PBR.

However, thermodynamic limitations of NH_3 decomposition reaction at low temperature (*i.e.* x_{NH_3} = 100% at T ≥ 450°C) and the NH_3 poisoning effect on the fuel cell installed on H_2-fuelled vehicles, represent still a barrier for the adoption of NH_3 as a future fuel carrier for vehicular applications. Therefore, to tackle these problems, the development of a hollow fibre palladium-based membrane hollow fibre reactor (MHFR) has been included in this study as well. In this respect, the MHFR would combine both the reaction and separation units integrating a palladium (Pd) membrane with a 100% selectivity to H_2. The approach adopted in this work was to develop a MHFR able to achieve a 99.99999% NH_3 conversion in order to ensure an NH_3 concentration at the exhaust lower than 0.1 ppm. By Le Chatelier's principle, the membrane allows

increasing the NH_3 conversion beyond thermodynamic equilibrium limits by continuously removing the produced H_2, enabling the membrane reactor to produce high-purity H_2 at lower temperatures than conventional catalytic reactors.

This research work has been carried out at three different levels, i) materials development and characterisation (*i.e.* Chapters 2-5), ii) reactor design and performance studies during the NH_3 decomposition reaction (*i.e.* Chapters 4-6), and iii) feasibility study of the different reactors for on-board H_2 production (*i.e.* Chapter 6).

Chapter 2 describes the methods used to synthesise and characterise the catalyst supports proposed, *i.e.* one carbon xerogel (*i.e.* CX), two activated carbon xerogels (*i.e.* ACX_{1h} and ACX_{5h}), and two N-doped carbon xerogels (*i.e.* UCX and NCX). Similarly, the procedures adopted to synthesise and characterise three series of catalysts, *i.e.* un-promoted and sodium-promoted ruthenium-based catalysts (*i.e.* Ru and Ru/Na), and cobalt/molybdenum-based catalysts (*i.e.* Co/Mo), were described in this chapter.

Chapter 3 provides a detailed description of the textural, chemical and structural properties of the carbon xerogels. For example, the nitrogen adsorption and desorption isotherms at -196°C showed that carbon dioxide (CO_2) activation treatment of the carbon xerogels lead to two distinct effects, depending on its duration. Furthermore, it was found that the N-doping of carbon xerogels induced a reduction of the specific surface area and total pore volume of both UCX and NCX due to the addition of heteroatoms to their carbon lattice. Likewise, the Temperature Programmed Desorption and X-Ray Photoelectron Spectroscopy experiments confirmed that due to the presence of fewer oxygen surface groups and more nitrogen groups on their surface, both UCX and NCX exhibit a more basic character compared to CX, $ACX_{1h,}$ and ACX_{5h}. Finally, based on their higher burning temperatures, N-doped carbon xerogels were also found to be more thermally stable than their non-doped counterparts.

Ru-based catalysts were extensively described in Chapter 4 of this thesis. Particular attention was paid to how the properties of the different carbon xerogels and the use of Na as catalyst promoter affected the performance of the catalysts during the NH_3 decomposition reaction. In this respect, it was found that among all un-promoted catalysts, Ru-NCX exhibited the best performance due to, in part, the higher basicity and electron conductivity of NCX when compared to the other carbon xerogels. The performance studies, together with the Transmission Electron Microscopy results, showed that catalysts with a Ru average particle size higher than 2.5 nm exhibited higher reaction rates. Likewise, it was found that the addition of Na had a positive effect on the performance of all catalysts studied during the NH_3 decomposition reaction (*i.e.* at least 3.7 and 1.5 times higher reaction rates at 450°C after the first and second reaction run, respectively). Finally, regardless of the use of Na, all Ru-based catalysts exhibited high thermal stability and catalyst preservability at the operating conditions (*i.e.* 450°C, 1 atm), as shown by 10 h reaction experiments and elemental analysis performed after the stability test.

Similarly, Chapter 5 provides a detailed description of the series of Co/Mo-based catalysts studied in this work. It was found that Co/Mo-NCX was the most suitable catalyst candidate for the NH_3 decomposition reaction and that the optimal metal particle size for Co/Mo-based catalysts is around 2.2 nm. Furthermore, also Co/Mo-based catalysts showed excellent thermal stability, as proven by the constant ammonia conversion achieved during the long-term stability tests (*i.e.* 100 h for Co/Mo-NCX and 10 h for the other Co/Mo-based catalysts).

The design of the hollow fibre reactors (HFRs) and the hollow fibre membrane reactor (MHFR) used in this work was covered in Chapter 6 and Chapter 7, respectively. In order to develop the hollow fibre reactors, the best performing Ru-based and Co/Mo-based catalysts were deposited into a 4-channelled hollow fibre (HF) substrate by adopting a two steps approach that ensured a homogeneous distribution of the catalyst. More specifically, a single HF unit 10

cm long was used for the deposition of Ru/Na-NCX, whereas a module of 10 HF units 5 cm long was used for the deposition of Co/Mo-NCX. Likewise, for the development of the MHFR, the HF was used as a support of a Pd membrane, and Ru/Na-NCX was packed in contact with the membrane in the shell side of the MHFR. The catalysts performance was assessed during the NH_3 decomposition reaction between 100°C and 600°C using HFRs, and between 300°C and 450°C using the MHFR, to prevent damaging the Pd membrane. Furthermore, the thermal stability during the reaction experiments using HFRs was assessed at 450°C.

To conclude, Chapter 6 and Chapter 7 include the feasibility study of the different catalytic reactors presented in this work for on-board H_2 production. With this scope, the PBRs, HFRs, and MHFR were compared in terms of volume, catalyst loading, and efficiency. This investigation demonstrated the superiority of the HF-based reactors over the traditional PBRs, not only in terms of remarkably high NH_3 decomposition reaction rates but also by their noteworthy advantages in terms of costs, volume occupied, and efficiency.

Lay summary

Green hydrogen has been proposed as promising alternative to traditional automotive fuels to help mitigate their impact on climate change. However, due to safety concerns, a “hydrogen-carrier fuel” could be designed to avoid the direct use of hydrogen on-board. In this regard, green ammonia has been suggested as promising hydrogen-carrier fuel, since it carries hydrogen with the main advantage of a safer storage and handling for automotive applications.

Nevertheless, the storage of ammonia on board would need a reactor to convert firstly the ammonia in hydrogen, and then send it to the fuel cell, which is the main motor of the system. Typically, the ammonia decomposition reactor, called packed bed reactor, is made of randomly packed beads coated with precious metals, and its size and cost outrange what economically viable for common vehicles.

It is aim of this project to design and assess an innovative and more affordable technology for this application to make ammonia decomposition a viable option for automotive applications, *i.e.* multifunctional catalytic hollow fibre-based reactors using non-precious metals based catalysts. With this scope, two different hollow fibre-based reactors have been designed in this work, depending on the function of the hollow fibres as catalyst or a membrane support. In the first case, the hollow fibre structure allows for lower energy requirements to run the system and lower catalysts loading. In the second case, the use of a selective membrane able to separate the hydrogen from the reactant ammonia and some by-products allows to obtain the highest conversion of the ammonia even at mild operating conditions.

The promising results obtained from the use of innovative elements of the catalysts, such as unexplored carbon materials as support and non-precious metals as the active phase, suggest that the low-cost catalysts developed in this work have good potential as effective alternative to the more common and more expensive catalysts used so far for the decomposition of ammonia. In

addition, this work demonstrates the advantages of using hollow fibre-based reactors for on board applications over conventional packed bed reactors, as evidenced by the higher efficiency, smaller size and lower costs of the former compared to the latter, when used under the same operating conditions (*i.e.* temperature, pressure and catalyst).

To conclude, the pioneering Multifunctional Catalytic Hollow Fibre-based Reactors proposed in this thesis show superior performance if compared with the state-of-art reactors for ammonia decomposition, opening the doors to a new line of catalytic converters which can face the challenges of on-board hydrogen production.

"Promise me you'll always remember:

You're braver than you believe,

and stronger than you seem,

and smarter than you think."

– A. A. Milne

Acknowledgments

In presenting my PhD thesis, I would like to express my gratitude to those who have supported and guided me during the entire research program and I want to acknowledge the University of Edinburgh for the financial support.

Foremost, I would like to thank my supervisor Dr. García García, also known as Fran, for his invaluable advice, support, and patience during my PhD study. Spending time with you in your office and the laboratory, working closely together, has helped me in realising what I am passionate about, and in growing as a better person and engineer.

I would like to acknowledge also my second supervisor Dr. Lau and Dr. Santori for their support and suggestions during my annual reviews. In addition, I would like to thank Dr. Dimartino and Dr. Orejon Mantecon with whom I have been spending time in these three years teaching to the students, I really appreciated the pleasing moments we spent together.

I also wish to thank the members of The Torch group, to whom I wish all the best, especially Miguel. I am glad for all the fun and unforgettable moments we have shared during this journey we have started together.

Among my colleagues, I would like to give special thanks to Elsa for her friendship and the support shown in every happy and sad moment of my PhD. Our coffee and lunch breaks will always be one of the best memories of the last few years.

A very special thank you to my family, particularly my parents and my sister, for the support and encouragement given, always believing in my potential.

Last but not least, I would like to express my infinite gratitude to my lovely partner and colleague, Roberto, for patiently supporting me throughout all process. Without you as my backbone, I would not have the strength, resilience, and courage to accomplish this far. As you once said, it has been, and it will be, a privilege to share life with you.

Publications

Published

Mazzone, S., Campbell, A., Zhang, G. and García-García, F.R., 2021. Ammonia cracking hollow fibre converter for on-board hydrogen production. *International Journal of Hydrogen Energy*, *46*(76), pp.37697-37704.

Mazzone, S., Goklany, T., Zhang, G., Tan, J., Papaioannou, E.I. and García-García, F.R., 2022. Ruthenium-based catalysts supported on carbon xerogels for hydrogen production via ammonia decomposition. *Applied Catalysis A: General*, p.118484.

Mazzone S, Leishman C, Li K, García-García F.R., 2022. Compact non-PGM catalytic hollow fibre converter for on-board hydrogen production. *Sustainable Energy & Fuels.*

In preparation

Mazzone S, Li K, García-García FR. On-board high purity hydrogen production by low temperature ammonia decomposition using a Hollow Fibre Membrane Converter. *Journal of Membrane Science*

Larkin C, Lampri K, Mazzone S, Oliva F, García-García FR. The role of hollow fibre-based adsorption units and carbon xerogels in the decarbonisation of transport: A study under real vehicle exhaust conditions.

Table of Contents

List of figures

List of tables

Nomenclature

a	Lattice parameter of the ruthenium hexagonal closed pack (hcp) structure (nm)
A	Area of both the sponge-like and finger-like regions of a single hollow fibre unit (m^2)
A_C	Area of one hollow fibre channels (m^2)
$C_{NH_{3_{in}}}$	Inlet concentration of ammonia ($mol \cdot m^{-3}$)
$C_{NH_{3_{out}}}$	Outlet concentration of ammonia ($mol \cdot m^{-3}$)
d	Spacing between crystal planes in a material
d_i	Diameter of the i-th metal particle (nm)
d_{max}	Maximum reactor diameter allowed (m)
d_p	Catalyst pellets diameter (m)
D	Metal particles dispersion (%)
D_e	Effective diffusivity ($m^2 \cdot s^{-1}$)
D_m	Metal average particle size (nm)
D_P	Pore size (μm)
E_a	Activation Energy ($kJ \cdot mol^{-1}$)
$\dot{F_{NH_3}}$	Ammonia molar flowrate ($mol \cdot min^{-1}$)
$GHSV$	Ammonia gas hourly space velocity ($ml_{NH3} \cdot g_{cat}^{-1} \cdot h^{-1}$)
k	Reaction rate constant ($h^{-1} \cdot g_{cat}^{-1}$)
k_{HFR}	Reaction rate constant in a Hollow Fiber Reactor ($h^{-1} \cdot g_{cat}^{-1}$)
k_{PBR}	Reaction rate constant in a Packed Bed Reactor ($h^{-1} \cdot g_{cat}^{-1}$)
K	Scherrer equation constant $(-)$
K_{pred}	Equilibrium constant for the predicted ammonia decomposition for a MHFR $(-)$
L_c	Apparent crystallite size along the c-axis (Å)
L_{HFR}	Hollow Fibre Reacor length (m)
L_{MHFR}	Hollow Fibre Membrane Reactor length (m)
L_{max}	Maximum reactor length allowed (m)
L_{PBR}	Packed Bed Reactor length (m)

n	Diffraction order $(-)$
n_i	Number of particles with diameter d_i $(-)$
n_{Ru}	Ruthenium loading in moles (mol)
N_{HF}	Number of hollow fibre units $(-)$
P/P_0	Relative vapour pressure $(-)$
r_{HFR}	Reaction rate in a Hollow Fibre Reactor ($mol \cdot m^{-3} \cdot h^{-1} \cdot g_{cat}^{-1}$)
r_{NH_3}	Ammonia decomposition reaction rate ($mol \cdot m^{-3} \cdot h^{-1} \cdot g_{cat}^{-1}$)
r_{PBR}	Reaction rate in a Packed Bed Reactor ($mol \cdot m^{-3} \cdot h^{-1} \cdot g_{cat}^{-1}$)
r_p	Catalyst pellets radius (m)
R_{H_2}	Hydrogen recovery (%)
S_{BET}	Specific surface area ($m^2 \cdot g_{cat}^{-1}$)
T_{10}	10% conversion temperature (°C)
TOF	Turnover Frequency ($mol_{NH3} \cdot mol_{Ru}^{-1} \cdot h^{-1}$)
U	Superficial fluid velocity ($m \cdot s^{-1}$)
V	Reactor volume (L)
V_{HFR}	Hollow Fibre Reactor volume (L)
V_{max}	Maximum reactor volume allowed (L)
V_{MHFR}	Hollow Fibre Membrane Reactor volume (L)
V_{PBR}	Packed Bed Reactor volume (L)
$\dot{V_{H_{2,P}}}$	Hydrogen flowrate in the shell of the reactor ($L \cdot min^{-1}$)
$\dot{V_{H_{2,R}}}$	Hydrogen flowrate in the lumen of the reactor ($L \cdot min^{-1}$)
$\dot{V_{NH_3}}$	Ammonia volumetric flowrate ($L \cdot min^{-1}$)
W	Catalyst loading (kg)
W_{HF}	Amount of catalyst per cm of hollow fibre (mg)
W_{HFR}	Catalyst loading in the Hollow Fibre Reactor (kg)
W_{MHFR}	Catalyst loading in the Hollow Fibre Membrane Reactor (kg)
W_{PBR}	Catalyst loading in the Packed Bed Reactor (kg)
x_{NH_3}	Ammonia conversion (%)
x_{pred}	Predicted equilibrium ammonia conversion in a MHFR (%)

Greek symbols

β	Full-width half-max (FWHM) of the peak of interest (°)
γ	Mercury surface tension (N/m)
$\frac{\Delta P}{L}$	Pressure drop per reactor length (bar·m^{-1})
ε_b	Catalyst bed porosity (−)
ε_{HF}	Hollow fibre porosity (−)
θ	Angle of the incident light (°)
λ	Wavelength of the radiation (nm)
μ_f	Dynamic viscosity of ammonia (Pa·s)
ρ_b	Density of the catalytic bed (kg·m^{-3})
ρ_f	Ammonia density (kg·m^{-3})
φ	Contact angle between mercury and the sample (°)
ϕ^2	Thiele modulus (−)

Abbreviations

AC	Active Carbon
ACX$_{1h}$	1 hour carbon dioxide activated carbon xerogel
ACX$_{5h}$	5 hours carbon dioxide activated carbon xerogel
Al$_2$O$_3$	Alumina oxide
Air-TGA	Thermogravimetric analysis in air atmosphere
Ar	Argon
BET	Brunauer – Emmett – Teller
BJH	Barrett-Joyner-Halenda
CNF	Carbon Nanofiber
CNT	Carbon Nanotube
Cl	Chlorine
CO	Carbon oxide
CO$_2$	Carbon dioxide
Co	Cobalt
CoO	Cobalt(II) Oxide
Co$_3$O$_4$	Cobalt(II,III) Oxide

$CoMoO_4$	Cobalt Molybdate
$Co_2Mo_3O_8$	Dicobalt Trimolybdenum(IV) Oxide
CX	Carbon xerogel
EDS	Energy Dispersive X-ray Spectroscopy
ELP	Electroless Plating
Fe	Iron
GHG	Greenhouse Gas
H	Hydrogen atom
H_2	Hydrogen molecule
HAADF	High-Angular Annular Dark-Field
HCl	Hydrochloric acid
HF	Hollow Fiber
HFR	Hollow Fiber Reactor
Hg	Mercury
HSAG	High Surface Area Graphite
ICP-MS	Inductively coupled plasma mass spectrometry
MHFR	Hollow Fiber Membrane Reactor
MIP	Mercury Intrusion Porosimetry
Mo	Molybdenum
MoO_2	Molybdenum(IV) Oxide
MoO_3	Molybdenum(VI) Oxide
N	Nitrogen atom
N_2	Nitrogen molecule
N_2-*TGA*	Thermogravimetric analysis in nitrogen atmosphere
Na	Sodium
Na_2O	Sodium Oxide
NaOH	Sodium Hydroxide
Ni	Nickel
NH_3	Ammonia
NCX	Carbon xerogel doped with nitrogen by Ammonia/Air activation
O_2	Oxygen

PBR	Packed Bed Reactor
Pd	Palladium
Ru	Ruthenium
SD	Standard Deviation
SEM	Scanning Electron Microscopy
Sn	Tin
STEM	Scanning Transmission Electron Microscopy
STP	Standard Temperature and Pressure
TEM	Transmission Electron Microscopy
TPD	Temperature Programmed Desorption
TPR	Temperature Programmed Reduction
TW	This work
UCX	Carbon xerogel doped with nitrogen by using urea
XPS	X-Ray Photoelectron Spectroscopy
XRD	X-Ray Powder Diffraction

Chapter 1 Introduction

1.1 Research Background

1.1.1 Hydrogen as automotive fuel

Today the way energy is produced and consumed is under debate as it is increasing the emissions of GHGs, which dangerously interferes with the climate system. This means that a de-carbonisation of the global energy system is required. The need to move from an economy based on fossil sources to one based on sustainable resources to minimize the environmental impact caused by the energy production, lead the scientific community to investigate the use of alternative fuels to traditional carbon-based ones [2].

With this scope, the use of H_2 as fuel for vehicular applications has been widely investigated over the past years, and it is now considered a promising mitigation solution for the environmental pollution and greenhouse gases emissions [3,7,8]. For instance, several vehicles manufacturers, such as Toyota, Aston Martin, BMW, Hyundai offer H_2 fuelled-vehicles commercially [5,9–11].

However, safety issues associated with the H_2 storage, thereby its transportation, still represent one of the main challenges limiting its use as fuel for on-board applications [2,3,7,8]. In this respect, to store a functional amount of H_2 on a vehicle, it has been reported that it must be stored to pressure of 700 bar in approximately 90 L (volume data extrapolated from [5]), which not only represents a significant safety risk but also leads to refuelling issues. To face this challenge, it has been proposed to safely store and transport H_2, by using either adsorptive storage materials or chemical storage molecules. Adsorptive storage materials, such as MOFs and porous carbon structures [12–14], are a group of materials exhibiting high surface area and porosity, which store H_2 molecularly through physisorption by van der Waals interaction, whereas chemical storage molecules, such as hydrocarbons and NH_3 [13,15], contain hydrogen atoms and form molecular H_2 when releasing it. In particular, as will be discussed in more detail in the next sections, this work focuses on

the use of NH_3 as an H_2 storage and carrier molecule for on-board H_2 production.

1.1.2 Ammonia as hydrogen-carrier molecule

NH_3 has been identified as a promising H_2 storage and carrier molecule for on-board applications due to its physical and chemical properties, including high H_2 content (*i.e.* 17.8 wt.%), high gravimetric energy density (*i.e.* 4318 $Wh \cdot kg^{-1}$), narrower flammability range in air (*i.e.* 16-25%) compared to H_2 (*i.e.* 4-75%). Furthermore, NH_3 can be stored in liquid form at ambient temperature and low pressure conditions (*i.e.* 108 kg of H_2 per m^3 at 20°C and 8.6 atm) [16–20]. In addition, NH_3 has an extensive and well-developed manufacturing distribution infrastructure worldwide to guarantee uninterrupted fuel supply, and its production capacity continues to grow by more than 20% [21].

It is worthy to highlight that on-board H_2 production via NH_3 decomposition presents the advantage over steam reforming that it does not need to use an additional reactant such as steam. Hence, when NH_3 as a H_2 carrier, an additional infrastructure to fit the water tank and steam generator system in the vehicle is not needed [22,23]. This is particularly beneficial considering the on-board space constraints of commercial vehicles to be respected (*i.e.* available volume of ~ 63L [5]).

However, the use of NH_3 for on-board applications presents some drawbacks. For instance, the fact that the most prominent technology for H_2 production via NH_3 decomposition is a traditional catalytic PBR that used a precious metal-based catalyst, which is expensive and outsized [83]. Therefore, to implement this technology, a catalytic reactor configuration with a compact design and that satisfy the requirements for automotive applications needs to be developed. Likewise, the NH_3 can poison the fuel cell installed into the H_2-fuelled vehicles with a threshold of <1 ppm affecting its efficiency, hence either a reactor able to achieve a minimum NH_3 conversion of 99.9999% or suitable adsorbents and membranes needs to be used to produce high-purity H_2 [17,24,25].

1.1.2.1 Ammonia decomposition reaction – Thermodynamics and Kinetics

NH_3 decomposition into H_2 and nitrogen (N_2), shown in the equation below, is the reverse reaction of NH_3 synthesis used in the well-known Haber-Bosch process:

$$2NH_3 \leftrightarrows N_2 + 3H_2 \quad (1.1)$$

The NH_3 decomposition is an endothermic reaction (*i.e.* $\Delta H_{(298K)}$ = 46.2 $kJ \cdot mol_{NH3}^{-1}$), which requires high temperatures and low pressures to proceed, as by Le Châtelier's principle. In addition, the NH_3 decomposition is a reversible reaction whose conversion at a given temperature is controlled by the thermodynamic equilibrium. In this respect, Yin et al. firstly proposed to adopt the following equation to express the relationship between the NH_3 thermodynamic equilibrium conversion and temperature at normal pressure [26]:

$$40100 - (25.46TlnT) + (0.00917T^2) - \left(\frac{103000}{T}\right) + 64.81T = -RTln\left(\frac{1.3x_{NH_3}^2}{1 - x_{NH_3}^2}\right) \quad (1.2)$$

Likewise, with the scope of investigating the NH_3 decomposition reaction, in 1980 Ertl et al. studied the decomposition of NH_3 on a single crystal of iron (Fe), and proposed the following mechanism [27]:

$$\begin{gathered} NH_3 \leftrightarrows NH_{3,ads} \\ NH_{3,ads} \rightarrow NH_{2,ads} + H_{ads} \\ NH_{2,ads} \rightarrow NH_{ads} + H_{ads} \\ NH_{2,ads} \rightarrow N_{ads} + H_{ads} \\ 2H_{ads} \rightarrow H_2 \\ 2N_{ads} \rightarrow N_2 \end{gathered} \quad (1.3)$$

As schematically represented in Figure 1.1, a molecule of NH_3 adsorbs on the surface (1) and H is sequentially cleaved and forms surface H species (2-4) before combining on the surface to form H_2 and desorbing (5), and then two adsorbed N atoms recombine and desorb as N_2 (6). Note that $*$ refers to an active site and X* refers to the species X adsorbed onto an active site.

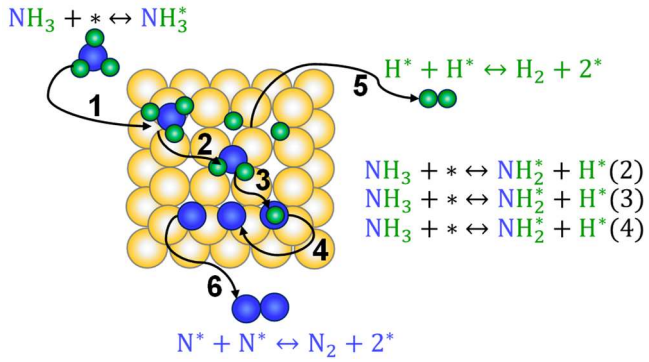

Figure 1.1. NH_3 decomposition reaction mechanism.

Using this mechanism of reaction as a reference, several kinetic studies demonstrated that the final step, *i.e.* the recombinative desorption of N_2, is the rate-limiting step and follows the first order kinetics [28,29]. Particularly, Tsai and Weinberg studied the kinetics of the reaction over a Ru(001) surface and observed that the reaction rate-limiting step was the cleavage of the N-H bond of adsorbed NH_3 molecules at high temperatures (*i.e.* > 480°C), whereas it was the recombinative desorption of N_2 at lower temperatures (*i.e.* < 480°C) [28]. Similarly, Shustorovich and Bell, which studied the decomposition of NH_3 on several transition metal surfaces (*i.e.* platinum Pt(111), Ru(001), Fe(110), and rhenium Re(001)), obtained similar results [29].

1.1.3 Catalyst for the ammonia decomposition reaction

1.1.3.1 Selection of the active phase

The most active and extensively studied catalysts reported in the literature for the decomposition of NH_3 are Ru-based because Ru shows the optimum N_2 binding energy (*i.e.* 544–586 $kJ \cdot mol^{-1}$) to allow both NH_3 adsorption and N_2 molecules desorption [7,26,30]. Likewise, it has been reported that the NH_3 decomposition reaction is structure sensitive, presenting a reaction rate dependent on the geometry of the Ru metal particles. As can be seen in Figure 1.2, Ru particles can cluster into B3 or B4 sites, which consist of an ensemble of three or four coplanar atoms, respectively, or into B5 sites that consist of an ensemble of five edge atoms. In particular, the NH_3 decomposition reaction rate-limiting step is promoted by the presence of B5 sites whose concentration depend on the Ru particle size, and it is maximised when the Ru metal particle size is between approximately 2.5 and 5 nm [31–34].

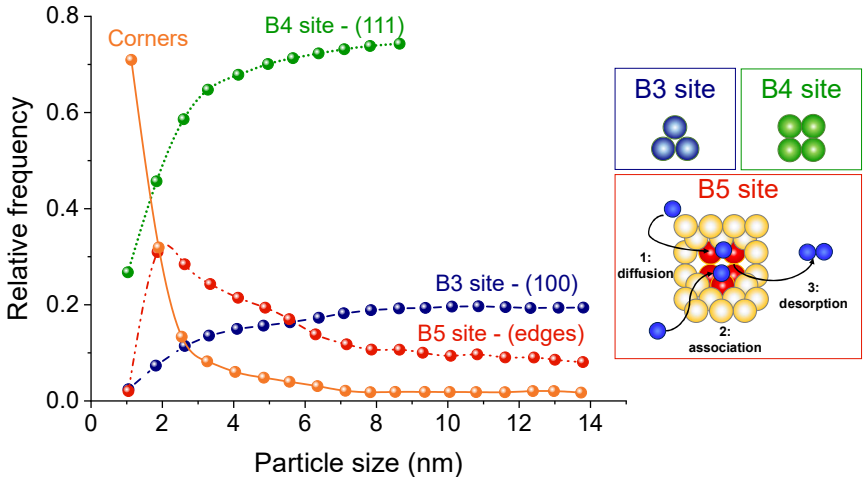

Figure 1.2. B3, B4 and B5-type sites frequencies as a function of the particle size of Ru. Image adapted from [34].

However, the mass production of Ru is restricted by its high cost and scarcity. This has triggered the catalytic community to search for a potential substitute of Ru-based catalysts for the NH_3 decomposition reaction [16,30,35]. In this regard, over the past years (see Figure 1.3), several non-noble metals have been investigated as potential substitutes for Ru, including Fe, cobalt (Co), and nickel (Ni) [30,35–40]. Even though Ni represents the most attractive alternative to Ru in terms of costs and accessibility, it has been determined that metallic nickel may be toxic and carcinogenic to humans. In addition to that, Ni-based catalysts necessitate higher working temperatures than Ru-based ones to show the same catalytic performance, due to the relatively low activity in terms of moles of metal [35,38,40].

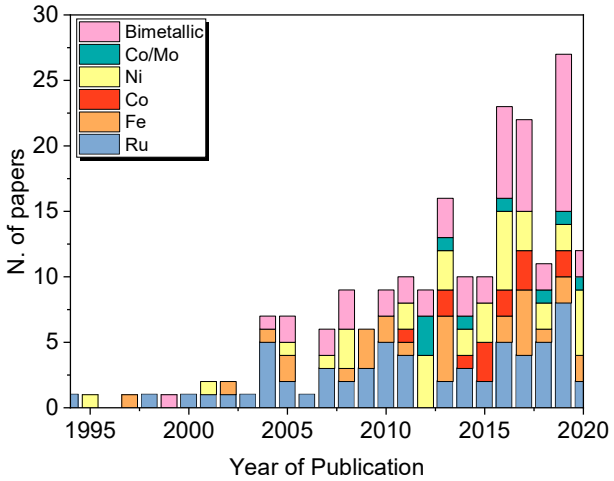

Figure 1.3. Number of research papers on NH_3 decomposition per metal used. Source: Web of Science, 01/2022.

Likewise, previous studies have reported that exists a volcano-type relationship, shown in Figure 1.4, between the N_2 binding energy to a metal surface and the NH_3 decomposition reaction rate [41]. The N_2 binding energy has a crucial influence on the catalytic activity because it affects the rate of N_2 desorption, which is the rate-limiting step of the NH_3 decomposition reaction [42]. Specifically, according to the Sabatier principle, the interaction between the metal catalyst and the NH_3 must not be too strong, otherwise, N_2 will fail to dissociate, nor too weak, otherwise NH_3 will not bind to the catalyst.

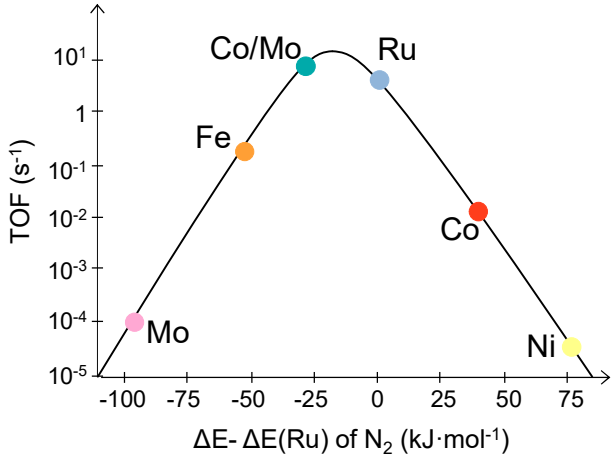

Figure 1.4. Relationship between the turnover frequency (TOF) of different metals for the NH_3 synthesis reaction at 400°C with respect to their N_2 binding energy. Image adapted from Jacobsen et al. [41].

Based on the finding that the synergetic effect of two single metals is generally more active than the equivalent monometallic catalysts [43,44], this volcano-type relationship has been widely used to investigate several bimetallic systems as potential substitutes for Ru. With this scope, according to the concept of periodic table interpolation, two metals with lower and higher N_2 binding energy than Ru were mixed to obtain similar electronic properties of Ru. For instance, Zhang et al. observed that FeCo/CNT are active as Co monometallic catalysts, but more stable under reaction conditions due to the addition of Fe [43].

However, as can be seen in Figure 1.4, among the several alternatives proposed, the combination of Co and molybdenum (Mo) results in the bimetallic system of intermediate N_2 binding energy that best mimics the electronic properties of Ru [45]. Particularly, Duan et al. Ji et al. shown, via

experimental and simulation studies, that the combination of these metals, in a Co/Mo atomic ratio of 7/3, shown a N_2 binding energy that is as close to that of Ru one as can be achieved [36,41,45–47]. Therefore, based on that, the performance of both Ru-based and Co/Mo-based catalysts will be assessed during NH_3 decomposition reaction experiments.

1.1.3.2 Selection of the support

Previous studies demonstrated that the performance of the catalysts during the NH_3 decomposition reaction is support-dependent [26,35,48,49]. For instance, Ni-based catalysts were found to be inactive when supported on carbon materials, and highly active during the NH_3 decomposition when supported on ceramic materials [26]. On the contrary, it has been reported that the ideal support of catalysts based on Fe, Co and Ru for the decomposition of NH_3 should feature several properties, such as i) thermal stability under the reaction conditions, ii) large specific surface area, iii) electron conductivity, iv) low concentration of electron-withdrawing functional groups, and v) high basicity [16,26,50–52]. By these properties, carbonaceous materials, including active carbons (ACs), high surface area graphite (HSAG), carbon nanotubes (CNTs) and carbon nanofibers (CNFs) have been considered as the most suitable support for Ru-based catalysts for the NH_3 decomposition reaction [16,33,53–56].

Raróg et al. proposed the use of ACs as catalyst support for this decomposition reaction due to their high surface area, responsible for an enhanced metal dispersion, which increases the catalytic activity during the reaction [53]. To improve the electronic conductivity of ACs, thermal treatment at high temperature in an inert atmosphere have been used [51,52]. Particularly, the thermal treatment resulted in ACs with higher graphitisation degree and fewer electron-withdrawing groups on the surface, which are requirements for the NH_3 decomposition reaction [51]. Despite the AC-supported catalysts were found to be highly active for this reaction, their difficult reproducibility makes challenging their use as catalyst support [57].

As an alternative to ACs, Sørensen et al. proposed HSAG as catalyst support for the NH_3 decomposition reaction [56]. In addition to the high surface area, HSAG offers high conductivity and high thermal stability under reaction conditions, which is beneficial for the inhibition of the support gasification and the suitability of HSAG as catalyst support in wider temperature range applications. In this respect, Rossetti et al. [58] indicated that the gasification rate of the carbon support is reduced by increasing its graphitisation degree.

Successively, Yin et al. proposed CNTs as optimal catalyst support for the NH_3 decomposition reaction, due to their excellent conductivity [16,26,48,54]. For instance, the CNTs-supported catalyst gave rise to an NH_3 decomposition reaction rate three times higher than that of the AC-supported catalyst. This was mainly attributed to the higher electron transfer between CNTs and the metal, which promote the N_2 desorption, known as the reaction limiting step [59]. However, CNTs present several drawbacks, including high cost, difficulty to synthesise on large scale, and support gasification at low temperature (*i.e.* 423°C), which have always limited their use in industrial applications [60,61].

Based on their physical-chemical properties, Duan et al. proposed CNFs as promising alternative catalyst support to CNTs for this reaction [55]. Indeed, their study revealed that CNFs-supported Ru catalysts were highly active for H_2 production via NH_3 decomposition. Moreover, despite the lower graphitisation degree of CNFs compared to CNTs, the former lead to higher catalytic activities. This was attributed to the peculiar surface properties of CNFs, which enhanced the metal dispersion and the electronic properties of the catalyst, as well as their higher stability [55]. Even though CNFs could be considered as highly effective catalyst support for the NH_3 decomposition, similarly to CNTs, their use in industrial-scale applications is hindered by their poor reproducibility and their high cost [57].

Recently, in order to enhance the physical and chemical properties of conventional carbon materials (*i.e.* basicity and electrical conductivity), their N functionalisation has been studied [33,62,63]. Stöhr et al. showed that N doping resulted in carbon materials with higher thermal stability and resistance

to oxidation [62]. Moreover, the incorporation of N atoms in the carbon lattice has been found to enhance surface basicity and graphitisation degree of carbon materials [64–67]. In this respect, García-García et al. showed that Ru catalysts supported on N-doped CNTs were more active than their non-doped counterparts [33]. This can be explained due to the electron donor effect of N atoms, which modify the electronic structure of the catalyst support enhancing its interaction with metal particles [33,68].

Among the several carbon supports investigated so far, CNTs have been proposed as the most efficient catalysts support for this reaction due, in part, to their outstanding electrical properties [33,35,48,69]. However, in addition to their high cost/performance ratio, CNTs are challenging to uniformly deposit inside the hollow fibre due to their low-density sponge structure [61]. In this respect, although some impregnation methods allow the deposition of powder catalyst inside the hollow fibre substrate (*i.e.* dip coating for CNTs), the sol-gel Pechini impregnation method is preferred as it results in the catalyst being homogeneously dispersed [70,71].

A promising alternative to CNTs are carbon xerogels, which not only have been proven to be efficient catalyst supports but also offer a unique opportunity for addressing this challenge. As a matter of fact, due to their synthesis method, carbon xerogels could be deposited in the HF substrate via the sol-gel method and successively impregnated with the catalyst solution. Furthermore, carbon xerogels offer a wide range of textural and structural properties. Tailoring of these properties can be achieved by using different synthesis methods and post-synthesis treatments [63,72–74]. Over the last years, carbon xerogels have gained considerable interest in the catalysis research field due to their structure and surface versatility [63,75–79]. They are obtained from the carbonisation of organic xerogels, which are synthesised by the conventional sol-gel method originally proposed by Pekala, using resorcinol and formaldehyde as organic starting monomers [80]. Maldonado-Hódar et al. firstly proposed the use of carbon xerogels as catalyst support since they show large specific surface area, excellent electrical conductivity and high purity

[81]. These properties can be adapted according to the requirements of a specific application, which is indicative of a considerable advantage of carbon xerogels being a porous carbon material [81]. The hierarchical pore structure of carbon xerogels permits the fine-tuning of micro- and mesoporosity during synthesis and carbonisation processes, as well as by means of physical or chemical activation treatments [72,73,82], allowing to control their surface area, surface chemistry and conductivity. Additionally, several synthesis and/or post-synthesis methods can be employed to induce surface basicity via functionalisation and N doping, to improve their suitability as catalyst support for the NH_3 decomposition reaction [63,74,78,83,84]. Despite the interest in utilising carbon xerogels as catalysts support for a wide range of reactions, including oxidation [76], hydrogenation [77,85,86], and ozonation [79], their use in the NH_3 decomposition reaction, which is the case study investigated in this thesis, has never been reported.

1.1.3.3 Selection of the promoter

It is well known that high electron transfer from electropositive elements to the active metal surface is needed to promote the NH_3 decomposition reaction rate-limiting step, *i.e.* the recombinative N_2 desorption [35,87]. In this respect, the use of alkali promoters, such as caesium, barium, and sodium (Na), has been widely proposed in order to further improve the performance of catalysts based on Ru during the NH_3 decomposition [35,52,53,88–90]. Particularly, it has been widely reported that the Na can act as both structural and electronic promoter, not only encouraging the recombinative N_2 desorption but also avoiding sintering and agglomeration of Ru metal particles [87–89]. Based on that, although the Na possess a higher electronegativity than the cesium (*i.e.* 0.93 and 0.79, respectively), thereby a weaker electronic promoting effect [53,88,91], the effects of using the Na as a promoter for Ru-based catalysts have been further investigated with the scope of synthesising highly stable catalysts.

Three possible locations of the alkali promoters in the catalytic system were proposed by Tennison, where the promoter is i) adsorbed within the bulk of the

transition metal particle, ii) adsorbed on the support but in contact with the transition metal, or iii) adsorbed on the surface of the metal particle, as schematically represented in Figure 1.5 [92].

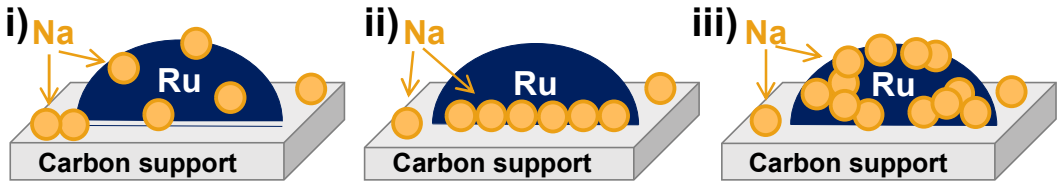

Figure 1.5. Proposed locations for alkali metals: i) adsorbed within the bulk of the metal particle, ii) adsorbed on the support but in contact with the transition metal, or iii) adsorbed on the surface of the metal particle.

1.1.4 Catalytic Reactors

As mentioned before, the most prominent technology for H_2 production via NH_3 decomposition consists of a catalytic PBR that uses Ru-based catalysts. As a result, this expensive technology is outsized and compromise its applicability to NH_3-fuelled vehicles [4]. This scenario represents a unique opportunity for innovative solutions in the development of a suitable technology for on-board H_2 production via NH_3 decomposition.

Over the past years, different reactors designs for NH_3 decomposition such as monolithic and microreactors have received a lot of attention due to their compact design, reduced weight, and improved conversion compared to traditional PBRs [22,23,93,94]. For instance, Wang et al. developed a monolithic-base “miniature” NH_3 cracker for portable fuel cell power supply. This cracker was able to produce roughly 158 W equivalents of H_2 via NH_3 decomposition at high temperatures [22]. Likewise, Chiuta et al. developed a super-compact NH_3-fuelled microchannel reactor unit (*i.e.* a plate consisting of 80 microchannels) wash-coated with a commercial 8.5 wt% Ru-based catalyst for H_2 production [94].

More recently, the interest in continuous catalytic HF-based reactors has increased due, in part, to the narrower residence time distribution when compared with PBRs that suffer from recirculation and generation of preferential paths and stagnant regions. The high thermal/mechanical stability and large area/volume ratio of the HFs allow operation with a decreased

catalyst metal loading and/or lower operating temperatures compared to traditional catalytic PBRs, while easy control of reactant/catalyst contact time can be used to fine tune selectivity [70,95,96]. Moreover, the HF-based reactors exhibit exceptional area/volume ratio without compromising pressure drop and efficiency. Furthermore, the fact that the HFs are made of ceramic, generally alumina oxide (Al_2O_3), which is resistant to corrosive reaction environments [2], make them the most suitable candidate for developing innovative catalytic converters for on-board H_2 production via NH_3 decomposition.

1.1.4.1 Catalytic hollow fibre reactor

Ceramic HFs, which can present symmetric, asymmetric, and “sandwich” porous structure, have been employed as a catalyst substrate and/or membrane support for the development of catalytic HFRs [70,71,95–101]. As schematically represented in Figure 1.6A, a symmetric HF consists of a sponge-like structure with small pore size, low porosity and high mass transfer resistance, an asymmetric HF consists of a sponge-like region and a finger-like region consisting of a plurality of self-organised micro-channels perpendicularly distributed around the lumen of the HF, whereas the “sandwich” HF consists of a sponge-like region separating two finger-like regions in which the micro-channels are perpendicularly distributed also around the outer surface of HF. Note that the finger-like region greatly contributes to increasing its surface area to volume ratio.

While the incorporation of the catalyst into a symmetric HF usually occurs via sol-gel method or incipient impregnation [102], the incorporation of catalyst into the micro-channels of an asymmetric (or “sandwich”) HF can be carried out also via dip coating and infiltration [71,97]. However, the sol-gel Pechini impregnation method is preferred as it results in the catalyst being homogeneously dispersed inside the HF substrate [70].

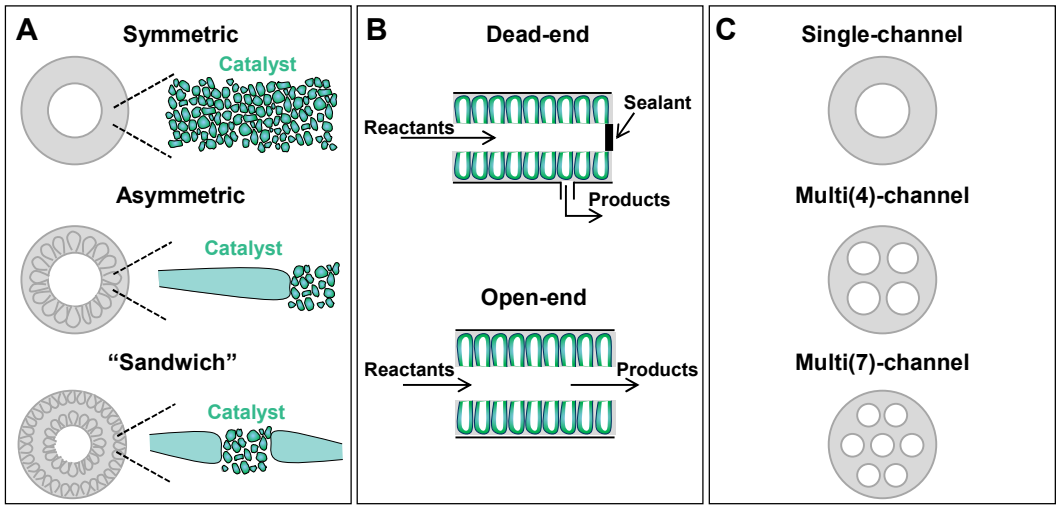

Figure 1.6. Schematic representation of different (A) morphologies, (B) configurations, and (C) geometries of the HF substrates.

In addition to the HF substrate structure, the performance of catalytic HFRs is also affected by the configuration (*i.e.* open-end or dead-end, see Figure 1.6B), the morphology and the geometry (*i.e.* single-channel or multi-channel, see Figure 1.6C) of the HF substrate, the distribution and loading of the catalyst, and the operating conditions [71,97,98]. Generally, it was found that the enhanced performance of asymmetric and "sandwich" HFRs compared to the symmetric counterparts, was attributed to the improved heat and mass transfer efficiencies and higher mixing and contact between catalyst and reactant, ascribed to the presence of the finger-like region in the HF substrate. Based on that, in this work, 4-channel asymmetric Al_2O_3 HFs will be used as catalyst support in order to develop catalytic HFRs for H_2 production via NH_3 decomposition. However, despite the several advantages that HFRs offer over traditional PBRs, the overall performance of HFRs is still limited by the thermodynamic behaviours of the catalytic reactions.

1.1.4.2 Catalytic hollow fibre membrane reactor

Membrane reactors combine a reaction and a separation process in a single unit, allowing to intensify a process and reduce its costs. The feasibility of membrane reactors depends on the properties of the membranes such as selectivity, permeability and stability under the operating conditions [8,103,104].

The classification of the membranes can be based on their i) geometry, *i.e.* disk, tubular or hollow fibre, ii) microstructure, *i.e.* dense or porous and symmetric or asymmetric, iii) positions with respect to the catalyst, and v) material, *i.e.* polymer, ceramic or metal [105], whereas the classification of membrane reactors can be based on the operation mode of the membrane, *i.e.* as an extractor, distributor or contactor (see Figure 1.7). Specifically for the NH_3 decomposition reaction, the use of metallic membranes, preferred due to their high thermal stability [107], as an extractor would be beneficial for overcoming the thermodynamic limitations of the reaction, due to the preferential removal of the H_2 from the reaction zone.

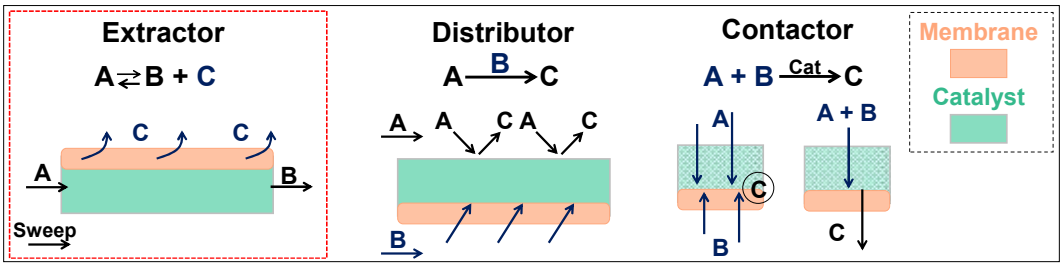

Figure 1.7. Membrane reactors classification based on the membrane operation mode.

The mechanism of H_2 permeation through metallic membranes follows the multistep process illustrated in Figure 1.8. Hydrogen molecules (H_2) from the feed are adsorbed on the membrane surface where they dissociate into hydrogen atoms (H), the hydrogen atoms diffuse through the membrane, and finally the hydrogen atoms emerging at the permeate side of the membrane reassociate to form hydrogen molecules, then desorb, completing the permeation process [106].

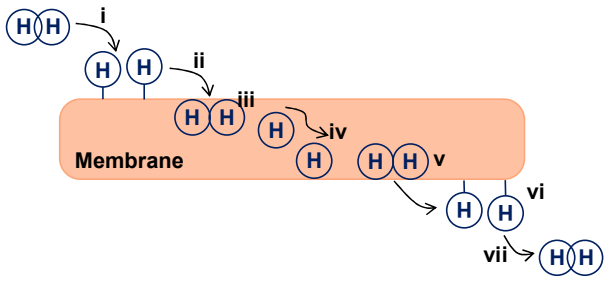

Figure 1.8. H_2 permeation through metallic membranes. Adapted from [106].

The steps involved in the hydrogen transport through the membrane are: i) diffusion of H_2 from the bulk of the gas to the membrane surface, ii) dissociation of H_2 to H and adsorption on the membrane surface, iii) dissolution of H into

the bulk metal, iv) diffusion of H through the bulk metal to the permeate side, v) association of H on the membrane surface at the permeate side, iv) desorption of H_2 from the surface to bulk of the gas, and vii) diffusion to the bulk of the gas from the membrane surface (see Figure 1.8). Note that the bulk diffusion step can be enhanced either by increasing the temperature, which is known to accelerate the adsorption and desorption processes and increase the solubility of H_2, or by reducing the membrane thickness, which reduces the diffusion distance [107].

So far, for H_2 separation, several metals have been extensively studied, including palladium, nickel, platinum, iron, silver, niobium, vanadium and tantalum [108]. The performance of a membrane is largely defined by the selectivity and permeability, which determine the purity and recovery of H_2, respectively. Furthermore, the thermal and mechanical stabilities of the membrane at the desired operating conditions are crucial. Among all the metal membranes for H_2 separation studied, Pd-based membranes have been reported with 100% selectivity to H_2, as well as with high permeability due to the great solubility of H_2 in Pd. However, Pd membranes suffer from several limitations such as α-β phase transition and H embrittlement phenomena [106–108]. As shown in Figure 1.9, at temperatures equal or lower than 295ºC and pressures less than 20 atm, dissociation and diffusion of H_2 in Pd promote a phase transformation from an α-phase to a β-phase [109,110]. Since the β-Pd hydride has a lattice parameter bigger than α-Pd hydride, *i.e.* 0.410 nm and 0.389 nm, respectively, the Pd atoms tend to elongate, causing distortion and hardening of the bulk and, in turn, leading to the fracture of the membrane and loss of selectivity [106,109]. Therefore, in order to avoid such failure, the operating temperature must be kept above 300 °C under an H_2 atmosphere and the membrane should be carried out in an atmosphere H_2-free.

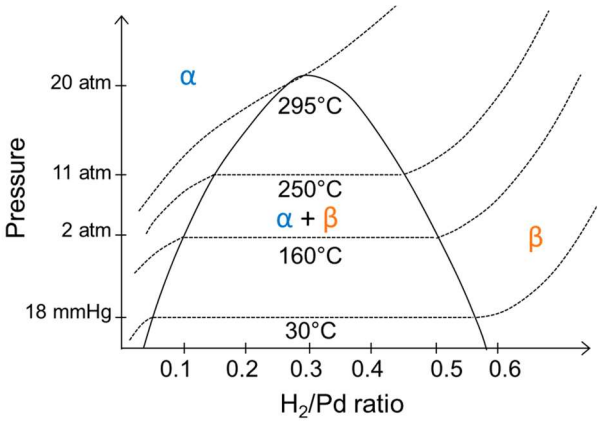

Figure 1.9. Adsorption relationship in Pd-H_2 systems. Adapted from [107].

As an alternative, the use of Pd-alloyed membranes has been suggested to improve the thermal and mechanical stability of the membranes without significantly compromise their selectivity, allowing for their use in a wider temperature range. For instance, Grashoff et al., which investigated the H_2 permeability and stability of several Pd-alloyed membranes, pointed out that palladium-silver alloys that contain ~23% of silver lead to i) a reduction in the critical temperature for the α to β hydride phase transformation from 300°C to 25°C, ii) the possibility to work at higher temperatures than Pd-membrane (*i.e.* T > 550°C) without compromising the mechanical strength of the membrane, and iii) a higher permeability than Pd-membrane [107].

Nevertheless, Pd membranes were selected as the separation layer in this study since the membranes were not subjected to thermal or stress cycles; furthermore, the maximum operating temperature for the NH_3 reaction experiments using the MHFR has been set at 450°C, which is lower than the maximum operating temperature of Pd membranes (*i.e.* 550°C) [110,111].

It is worthy to highlight that the morphological properties of the membrane support, *i.e.* pore size distribution, porosity, roughness of the substrate, mechanical and chemical stabilities, and thermal expansion coefficient play a crucial role in determining the permeability and the selectivity of a membrane, hence its efficiency [112,113]. For instance, according to Mardilovich et al., the selection of a defect-free substrate with an adequate pore size is crucial, being the optimal pore size at least three times smaller than the thickness of the membrane [114].

Several supports for Pd membranes have been already investigated, including ceramic, stainless steel and porous glass, whose properties have been listed in Table 1.1. It can be seen that despite porous stainless steel supports being mechanically and chemically stable, they exhibit large pore size and non-uniform pore size distribution, which are detrimental for the deposition of a thin, uniform and defect-free membrane. Hence, the thickness of metallic membranes supported on porous stainless steel is generally large [5]. In comparison, porous glass supports present a remarkably low thermal expansion coefficient, narrow pore size distribution and pore size between 4 to 5 nm, but they offer lower mechanical strength and chemical stability [15].

Table 1.1. Properties of inorganic supports for Pd membranes. Adapted from [101].

Properties	Porous Stainless Steel	Porous Glass	Ceramic Composite	Al_2O_3 Hollow Fibre
Mechanical stability	High	Low	Medium	Medium
Chemical stability	High	Medium	High	High
Expansion Coefficient	~9.9-17.3 ppm·ºC^{-1}	~0.8 ppm·ºC^{-1}	~0.1-10.5 ppm·ºC^{-1}	~7.2 ppm·ºC^{-1}
Pore size distribution	Large Dp = 5-10 µm	Narrow Dp ≈ 0.3-0.5 µm	Narrow Dp = 0.1-10 µm	Narrow Dp ≈ 0.1 µm
Production costs	High (Multi-step fabrication)	-	High (Multi-step fabrication)	Low (Single-step fabrication)
Module fabrication	Unsuitable (low S/V ratio)	-	Unsuitable (low S/V ratio)	Suitable (high S/V ratio)

Ceramic HFs represent a valid alternative as support for metallic membranes. Although they present a higher thermal expansion coefficient than the porous glass, ceramic HFs not only offer all advantages of a typical ceramic support in terms of mechanical and chemical stability and pore size distribution but also in terms of low production costs and high surface area to volume ratio, facilitating to scale up the process.

As already mentioned in the previous section, asymmetric Al_2O_3 HFs have been widely employed as membrane support to develop MHFRs for catalytic reactions with thermodynamic limitations [104,112,115,116]. As

schematically shown in Figure 1.10, two main configurations have been designed so far. In the first configuration (*i.e.* A) the catalyst, either in pellets or powder form, is packed in the shell side of the reactor and in contact with the membrane, whereas in the second configuration (*i.e.* B), the catalyst is deposited inside the micro-channels of the HF substrate.

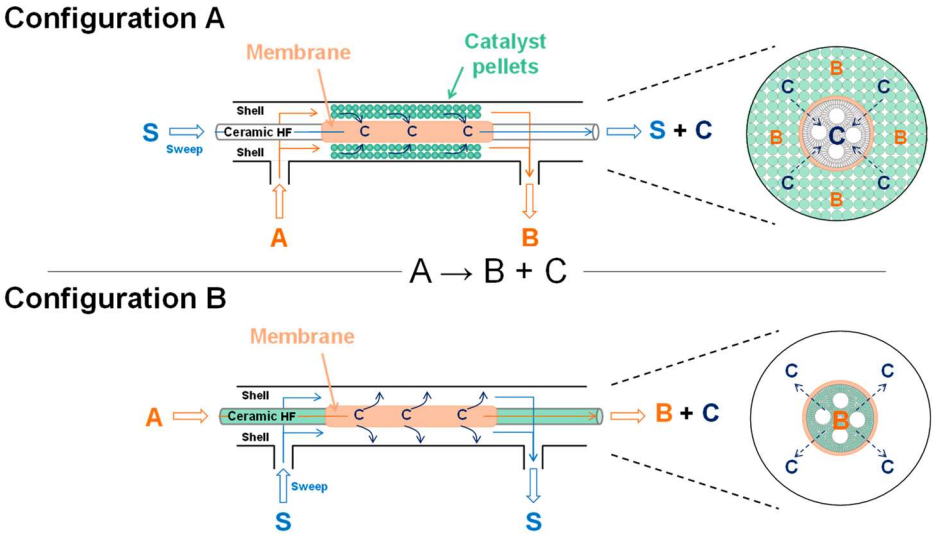

Figure 1.10. Schematic representation of the two configurations of a MHFR. Adapted from [70].

Despite both configurations leading to an improvement of the catalytic performance, exceeding the thermodynamic equilibrium limitations, configuration B offers additional advantages when compared to both a traditional PBR and configuration A. For instance, in agreement with what was discussed in Section 1.1.4.1, configuration B allows for improved internal mass transfer and kinetics of reaction, having the catalyst dispersed inside the micro-channels of the HF substrate rather than packed in the shell side of the reactor [99–101,115,117]. In this respect, as per configuration A, the mass transfer limitations inside the catalyst bed cannot be neglected as they may affect the H_2 diffusion through the membrane, thereby the membrane efficiency. Likewise, the use of HFs as support for both the catalyst and the membrane allows working at lower catalyst loading due to their large area/volume ratio of (*i.e.* > 1000 $m^2 \cdot m^{-3}$ [118]) and intensifying the contact between the reactant gases and the catalyst during the reaction.

However, in this work, only the MHFR in configuration A has been developed and tested for H_2 production via NH_3 decomposition. Due to the lower accessibility to the laboratory facilities and the higher difficulty in sourcing the HFs, together with the higher complexity of the development process of the MHFR presented in the configuration B, this decision relied on the willingness to prove at least in one scenario (*i.e.* configuration A) that MHFR can be effectively proposed as a potential technology for the on-board H_2 production. In particular, in order to develop the MHFR schematically represented in the configuration B in Figure 1.10, it would have been necessary to conduct a series of experiments to find the best procedure to deposit the catalyst inside the HF and the Pd membrane on the outer surface of the HF substrate without damaging or compromising the properties of both, taking into account that the membrane can be exposed to temperatures of up to 550°C and the carbonisation of the xerogel takes place at 800°C. For example, if the catalyst were deposited first, the risk would be that the membrane's ELP solution would react with the catalyst, damaging it and compromising the membrane's deposition at the same time. Similarly, if the membrane were deposited first, the catalyst support's carbonisation temperature would have to be lowered, compromising its properties and the performance of the catalyst during the NH_3 decomposition reaction.

1.2 Research Objectives

Although NH_3 has been proposed as a promising H_2 carrier candidate for vehicle applications [18–20], its commercial use is hindered by space constraints and the inefficiency in terms of volume, weight, and performance of the most common catalytic reactor employed for the NH_3 decomposition reaction, *i.e.* PBRs [4]. This scenario offered an excellent opportunity for the development of new technologies for on-board H_2 production via NH_3 decomposition. In this respect, the main objective of this study was to develop a series of Multifunctional Catalytic Hollow Fibre-based Reactors, which can satisfy the demands of NH_3-fuelled vehicles. In order to fulfil this aim, the effects of each reactor component, *i.e.* catalyst active phase, support and

promoter, HF substrate and Pd membrane, in catalytic performance were investigated.

With this purpose, this research work has been carried out following a bottom-up approach, consisting of four stages. The first stage focused on the synthesis and characterisation of a series of carbon xerogels, in order to investigate the effect of their textural and structural properties on the catalytic performance and thermal stability of the catalyst during the NH_3 decomposition reaction. The second and third stages consisted in the design, synthesis and characterisation of two series of catalysts (*i.e.* Ru-based and Co/Mo-based) supported on carbon xerogels and in the study of their catalytic activity and stability during the NH_3 decomposition reaction in a PBR. Finally, in the fourth stage, the best performing Ru-based and Co/Mo-based catalysts were tested using HF-based reactors, which were first designed to target on-board H_2 production in an NH_3-fuelled car, and then compared against the PBRs in terms of catalyst loading, volume and efficiency, in order to suggest the most suitable catalytic reactor for this application.

1.3 Thesis structure and presentation

As schematically represented below, this thesis consists of 8 chapters, which includes introduction (*i.e.* Chapter 1), experimental methods (*i.e.* Chapter 2), results and discussion chapters (*i.e.* Chapters 3-5), feasibility studies for on-board H_2 production (*i.e.* Chapters 6-7), and final conclusions (*i.e.* Chapter 8).

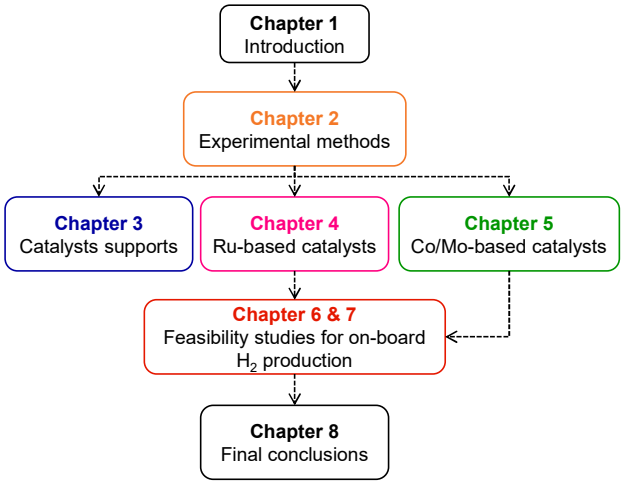

Figure 1.11. Schematic representation of the thesis structure.

Chapter 2 Experimental methods

This chapter provides an overview of the materials, techniques, and methods adopted in the experimental work carried out.

The procedures followed to synthesise the catalyst supports are described in detail. The techniques used to characterise them, as well as the apparatuses and the procedures used, are extensively explained. Similarly, the description of the experimental procedure adopted to synthesise both the Ru-based and Co/Mo-based catalysts, and the techniques used to characterise them, are covered in this chapter.

The following material characterisation techniques were implemented in this research project to thoroughly determine the textural and structural properties of the catalyst supports, and their effect on the catalytic activity of the catalysts during the NH_3 decomposition reaction. In addition, this chapter addresses the development of catalytic HF based reactors for the NH_3 decomposition reaction.

2.1 Synthesis of the catalyst supports

Resorcinol-formaldehyde xerogels were synthesised by the conventional sol-gel method, originally proposed by Pekala [80]. A starting 60 ml solution of resorcinol, sodium carbonate, formaldehyde and water, containing 30 wt. % solids was prepared. The molar ratios of resorcinol to sodium carbonate (R/C) and resorcinol to formaldehyde (R/F) were fixed at 200 and 0.5, respectively.

To begin making the xerogels' precursors solution, 50 ml of deionised water were pipetted into a clean glass jar with a sealable lid. The required mass of resorcinol (SigmaAldrich, ReagentPlus, 99 %) was weighed out accurately and added to the jar along with a magnetic stirrer bar. After placing on a magnetic stirrer plate, the contents of the jar were stirred to encourage the complete dissolution of resorcinol. Once the resorcinol was dissolved, the sodium carbonate (Sigma Aldrich, anhydrous, ≥ 99.5 %) was added to the reaction mixture in the jar with continued stirring, again until complete dissolution was

achieved. Then, the remaining deionised water and required volume of formalin (SigmaAldrich, 37 wt. % formaldehyde and 10-15% methanol as a stabiliser) were added to the jar, which was tightly sealed and allowed to stir for 30 min to ensure thorough mixing. Afterwards, the solution was left in a ventilation oven (SciQuip Oven 55S) for 3 days at 85°C and 3 days at 100°C to allow for gelation, curing and drying, as shown in Figure 2.1.

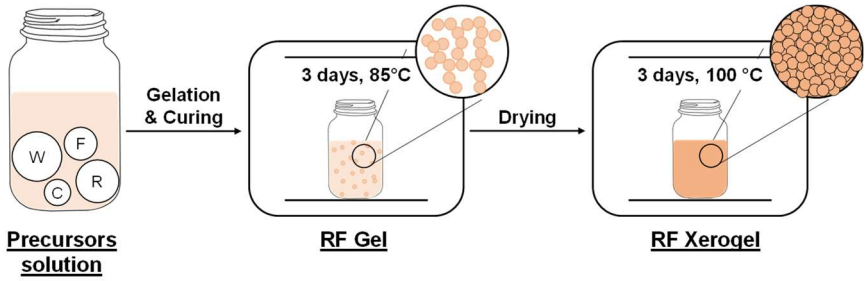

Figure 2.1. Schematic of the procedure followed to synthesise the resorcinol-formaldehyde xerogel.

To obtain the carbon xerogels starting from the organic resorcinol-formaldehyde xerogels, several methods have been adopted, as schematically represented in Figure 2.2. In particular, to study the influence of the support's textural and structural properties on the catalysts' performance during the NH_3 decomposition reaction, one carbon xerogel, two activated carbon xerogels and two N-doped carbon xerogels have been synthesised.

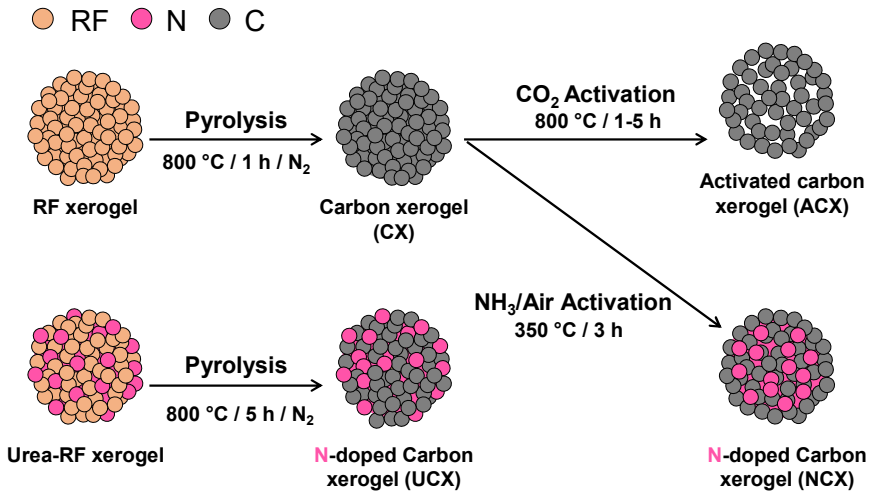

Figure 2.2. Schematic of the treatments used to synthesise the different carbon xerogels here studied.

The carbon xerogel labelled as CX, was obtained by carbonisation of the dried xerogel at 800°C in a N_2 atmosphere (*i.e.* 100 $cm^3 \cdot min^{-1}$ (STP)) using a tubular furnace (MTI Corporation, OTF-1200X). The activated carbon xerogels

labelled as ACX_{1h} and ACX_{5h}, were obtained by treating the CX in a CO_2 atmosphere (*i.e.* 100 $cm^3 \cdot min^{-1}$ (STP)) at 800°C for 1 h and 5 h, respectively. Finally, the two N-doped carbon xerogels were synthesised via (i) a co-precursor method using urea as a N-containing source and (ii) a post-synthesis activation in NH_3/Air atmosphere of CX, respectively. For the first method (i), R/F, R/C and Resorcinol/Urea (R/U) ratios were fixed at 200, 0.5, and 2, respectively. The solution was prepared, cured and dried following the same method described above. The N-doped carbon xerogel labelled as UCX, was obtained by carbonisation of the N-containing dried xerogel at 800°C for 1 h in a N_2 atmosphere (*i.e.* 100 $cm^3 \cdot min^{-1}$ (STP)) using a tubular furnace (MTI Corporation, OTF-1200X) [119]. For the second method (ii), the N-doped carbon xerogel labelled as NCX, was obtained by activating CX in an NH_3 and air atmosphere (*i.e.* 100 $cm^3 \cdot min^{-1}$ of NH_3:Air = 1:3 (STP)) at 350°C for 3 h.

2.2 Characterisation of the catalyst supports

2.2.1 Nitrogen adsorption and desorption isotherms at -196°C

Description of the technique

Adsorption occurs whenever a solid surface is exposed to a fluid. Particularly, gas adsorption has become a wide-used procedure to determine the surface area and the pore size distribution of porous materials. The pores are classified depending on their diameter width in micropores (*i.e.* <2 nm), mesopores (*i.e.* 2-50 nm) and macropores (*i.e.* >50 nm) [120–122].

Experimental adsorption isotherms recorded so far could have different forms, depending on the interaction between gas molecules and the interface. They are conveniently grouped into six major classes, which are shown in Figure 2.3A, according to the IUPAC classification [120,121]. Type I isotherms, called also rectangular or irreversible isotherms, are typical of the adsorbent-adsorbate interactions occurring in microporous materials; their main feature is the long plateau, indicating a negligible multilayer adsorption on the surface. Type II isotherms occur with non-porous or macroporous adsorbents, with multilayer adsorption; as a matter of fact, point B indicates that the monolayer

coverage is complete, and the multilayer coverage has started. Type III isotherms are also obtained from the interaction between gas molecules and non-porous or macroporous adsorbent, but they are indicative of weak adsorbent-adsorbate interactions. Both type IV and V isotherms exhibit a hysteresis loop, that is indicative of the capillary condensation, whose lower and upper branches represent the adsorption and the desorption steps, respectively. Although Type IV isotherms are related to Type II as they show multilayer adsorption, they are typical of mesoporous materials. Instead, Type V isotherms are related to Type III, as they are representative of weak adsorbent-adsorbate interactions. Finally, Type VI isotherms, called also stepped isotherms, are associated with layer-by-layer adsorption on a uniform surface, therefore on non-porous materials.

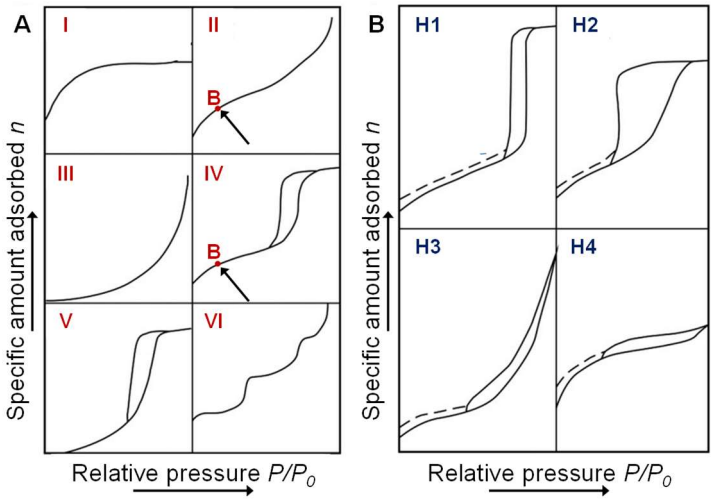

Figure 2.3. Classification of the (A) adsorption isotherms proposed and (B) hysteresis loops by IUPAC in 1985.

As stated above, both Type IV and V isotherms show a hysteresis loop, whose shape depends on the geometry of the pores of the studied adsorbents. According to the IUPAC classification, four principal types of hysteresis loops are widely recognised [121], as shown in the Figure 2.3B. Type I hysteresis loops are associated with materials made by packed, uniform spheres, and therefore are indicative of narrow pore size distributions. Instead, Type II loops clearly show a wider pore size distribution. Finally, both Type III and IV loops are associated with slit-shaped pores, with the difference that in Type IV loops these slits are narrower [121].

Brunauer-Emmett-Teller (BET) and Barrett-Joyner-Halenda (BJH) are analysis theories widely used for determining the surface area and the porous structure of the sample material [122]. The BET mechanism is an extension of that proposed by Langmuir, which is a theory for monolayer molecular adsorption. Specifically, the BET method assumes that there is no limit in the formation of multilayers and that the Langmuir theory can be used for each layer. Hence, BET analysis examines the external area and pore area of the materials to determine the total specific surface area by N_2 multilayer adsorption isotherms.

Instead, BJH analysis is widely used to determinate the pore size distribution and the pore volume of mesoporous materials, and it is generally applied to the nitrogen desorption branch of the nitrogen isotherms at -196°C. In particular, this method relates the amount of adsorbate (N_2) removed from the pores of the material, at decreasing values of the relative vapour pressure (P/P_0), to the size of pores.

Description of the experimental procedure

The surface area and pore volume of each carbon xerogel synthesised in this work were determined by studying nitrogen adsorption/desorption isotherms at -196°C using an iQ autosorb by Quantachrome. In order to remove moisture from the mesopores of the carbon xerogels, the samples were degassed at 150 °C for 150 min under nitrogen atmosphere prior to the analysis. 40 adsorption points and 40 desorption points were taken for each measurement. The BET and BJH methods were used to calculate the specific surface area and the pore size distribution of the samples, respectively.

2.2.2 Temperature Programmed Desorption

Description of the technique

In the case of carbon materials, Temperature Programmed Desorption (TPD) analysis is used to evaluate the amount and types of oxygen-containing surface groups formed on carbon surfaces. The key principle is to heat the sample at a linear heating rate under an inert atmosphere and record the

spectra of the released gases using a quadrupole mass spectrometer under ultrahigh vacuum conditions. During a TPD run, these oxygen surface groups are thermally decomposed to release CO_2 and carbon monoxide (CO) at different temperatures, depending on the thermal stability of the groups. Then, to assess the surface chemistry of the carbon materials, recorded CO_2 and CO TPD-spectra are deconvoluted separately into distinct peaks, which can be attributed to certain oxygen groups [123].

Description of the experimental procedure

To perform TPD experiments, the sample was loaded into a U-shape quartz glass cell, connected to the analyser (iQ autosorb, Quantachrome), ensuring that there were no leaks, in order to guarantee under vacuum conditions. The analyser was connected in-line to a mass spectrometer (HAL-201, HIDEN ANALYTICAL). The experiment was performed from room temperature to 700°C, under a 50 $cm^3 \cdot min^{-1}$ (STP) flow of pure helium.

2.2.3 Thermal Gravimetric Analysis in nitrogen and air atmosphere

Description of the technique

Thermal Gravimetric Analysis under nitrogen flow (N_2-TGA) can be used, in combination with the TPD analysis, to estimate the amount of various oxygen surface groups present on the surface of the carbon xerogels. The key principle is to heat gradually the sample under a N_2 atmosphere and record the sample's mass loss as a function of the temperature. The mass loss, in specific temperature ranges, corresponds to the amount in weight of the several oxygen surface groups identified via TPD analysis.

Likewise, Thermal Gravimetric Analysis under airflow (Air-TGA) can be used to assess the thermal stability of a carbon material. The sample is step heated in an air atmosphere and its mass loss is recorded as a function of the temperature. The extent of the sample's mass loss is inversely proportional to its thermal stability. Moreover, the first derivative of an Air-TGA profile is often studied to determine the burning temperature of the sample. Differently from

before, the higher the burning temperature, the higher the thermal stability of the sample.

Description of the experimental procedure

The oxygen surface groups were quantified by N_2-TGA, using a METTLER TOLEDO thermogravimetric analyser (TGA/DSC 3+). Each sample was heated up to 700°C using a 10°C·min^{-1} temperature ramp. A N_2 flowrate of 20 cm^3·min^{-1} (STP) has flowed throughout the experiment. The same experimental apparatus was used to study the thermal stability of the different carbon xerogels, by determining their burning temperatures via thermal gravimetric analysis in an air atmosphere (Air-TGA). For this experiment, the sample was step heated up to 700°C, under a 20 cm^3·min^{-1} (STP) flow of air.

2.2.4 X-Ray Photoelectron Spectroscopy

Description of the technique

X-Ray Photoelectron Spectroscopy (XPS) is a surface analysis technique that measures the energy of the electrons emitted from a sample material upon excitation from an X-ray [124–126], as schematically represented in Figure 2.4.

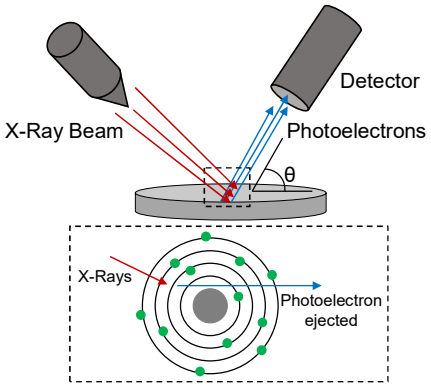

Figure 2.4. Schematic representation of a XPS process.

An X-ray photon is directed at the sample causing the emissions of the so-called photoelectrons, which have a specific kinetic energy measured by the instrument during the analysis, from one of the atom's core shells. Such energy corresponds to binding energy, which is the energy required to eject the electron from the atom's core [124,126]. Based on the values of these binding

energies, the elements present within the sample, their chemical state, as well as the other elements they are bonded to, can be identified.

Description of the experimental procedure

The two N-doped carbon xerogels herein synthesised were analysed by X-ray Photoelectron Spectroscopy (XPS), using a X-ray photoelectron spectrometer (Thermo ESCALAB 250, USA) equipped with an Al-Kα X-ray source (1486.7 eV), in order to obtain information about the nature and the amount of the N-groups on their surface. The N1s envelopes were curve-fitted using Gaussian component profiles using the Origin peak-fitting software. A Shirley baseline was used for sloping backgrounds.

2.2.5 Scanning Electron Microscopy

Description of the technique

Scanning Electron Microscopy (SEM) is one of the most common imaging techniques used to observe the surface morphology of a solid material, by investigating different length ranges, from nanometre to micrometre scale. A fine beam of primary electrons is directed at the sample via an electron gun, scanning across it by the scan coils. Different electronic signals can be emitted from the surface of the sample exposed to the incident beam, including secondary electrons, backscattered electrons, and photons (X-ray emissions). Then, the detector collects the signals of interest, which is in turn processed in order to obtain a 3D-like high magnification image of the sample's surface [124,127]. A schematic representation of a SEM system is shown in Figure 2.5.

To allow the sample to be penetrated by the electron beam, and to prevent an electrons build-up on the sample surface, the sample ought to be electrically conductive. In this respect, prior to the analysis, non-electrically conductive samples are generally coated with a thin layer of gold by sputtering [127,128].

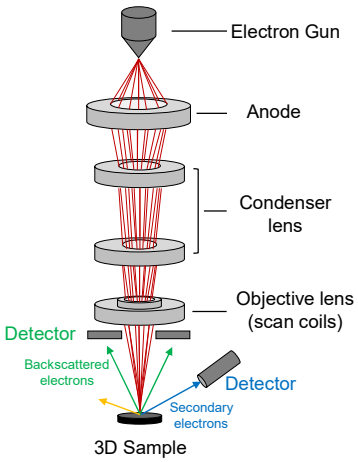

Figure 2.5. Schematic representation of the SEM mode.

Description of the experimental procedure

The surface morphology of the carbon xerogels was studied using a Jeol, Jsm-it100 Scanning Electron Microscope (SEM), operated at 20kV. The samples were uncoated and the working distance ranged between 23 mm and 29 mm.

2.3 Synthesis of the catalysts

2.3.1 Synthesis of ruthenium-based catalysts

Carbon xerogels here synthesised were used as supports of un-promoted and Na-promoted Ru-based catalysts. Un-promoted catalysts were prepared by the incipient wetness impregnation method, starting from a solution of $Ru(NO)(NO3)_3$ to get 1.5 wt.% of Ru. After the impregnation, the catalysts were dried overnight at 110°C. The resulting catalysts were labelled as Ru-CX, Ru-ACX_{1h}, Ru-ACX_{5h}, Ru-UCX, and Ru-NCX according to the impregnated supports.

In order to get Na-promoted catalysts, a successive wetness impregnation was carried out, using a 1M water solution of NaOH to get 5 wt.% of Na. After impregnation, catalysts were dried overnight at 110°C. The resulting catalysts were labelled as Ru/Na-CX, Ru/Na-ACX_{1h}, Ru/Na-ACX_{5h}, Ru/Na-UCX, and Ru/Na-NCX according to the impregnated supports.

2.3.2 Synthesis of cobalt/molybdenum-based catalysts

Co/Mo–based catalysts were synthesised by incipient wetness impregnation of carbon xerogels with an aqueous solution of $(NH_4)_2MoO_4 \cdot 4H_2O$ and $Co(NO_3)_2 \cdot 6H_2O$ in order to obtain 1.5 wt.% of metal loading, and a Co/Mo ratio equal to 7/3. After impregnation, the catalysts were dried first overnight at 120°C in a ventilation oven (SciQuip Oven 55S). The obtained catalysts were labelled as Co/Mo-CX, Co/Mo-UCX and Co/Mo-NCX, according to the impregnated catalyst supports.

2.4 Characterisation of the catalysts

2.4.1 Transmission Electron Microscopy

Description of the technique

Transmission electron microscopy (TEM) is an electron microscopy technique used for imaging samples at very high resolutions, up to atomic scales, probing their internal structure [128,129]. In the specific case of catalysts, TEM can be used to obtain information about the metal particles' size and distribution over the catalyst support. For this scope, the use of a TEM is preferred over the use of a light microscope. Although TEM operates on the same basic principles as a light microscope, it uses electrons instead of light, which have a much smaller wavelength than that of light, resulting in higher resolution images [127–129].

As schematically shown in Figure 2.6, an electron gun at the top of the microscope transmits a high-energy (*i.e.* up to 200 kV) beam of primary through an ultrathin and conductive sample, and the interactions between the electrons and the sample material are generally recorded as an image. A system of condenser lenses controls the beam diameter as it hits the sample. The objective lenses form an intermediate magnified image, which is in turn enlarged by the projective lenses on a fluorescent screen [127,129].

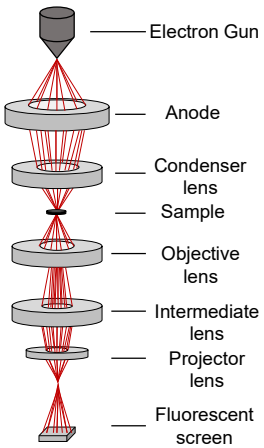

Figure 2.6. Schematic representation of the TEM mode.

Description of the procedure

Metal particle size distribution was estimated by transmission electron microscopy (TEM) using a Jeol TEM-1400 Plus. The catalysts, supported on carbon xerogels, were dispersed by ultrasonic treatment in an ethanol solution, placed on the copper TEM grid coated with a carbon film, and finally, the solvent was slowly evaporated. Since a large number of nanoparticles is needed for a high-quality particle size distribution, about 300 nanoparticles were analysed for each catalyst. Particles shown in the TEM images were analysed using the ImageJ software. The diameter of metal particles, which are assumed spherical, was estimated using the Automated Counting function built-in the software, which has an accuracy of 98%.

Moreover, the metal particles dispersion (D) over the catalysts support was estimated from the TEM metal particle size distributions using Eq.2.1, assuming that the dominant crystal structure of ruthenium is a hexagonal closed pack (hcp) with lattice parameters equal to *a*= *b*= 0.27 nm and *c*= 0.43 nm [130].

$$D\ (\%) = \frac{\sum n_i d_i^2}{\sum n_i d_i^3} \times \frac{6a}{\sqrt{3}} \qquad 2.1$$

Where n_i is the number of particles with diameter d_i.

2.4.2 Scanning Transmission Electron Microscopy and Energy Dispersive X-Ray Analysis

Description of the technique

Scanning Transmission Electron Microscopy (STEM) is a powerful and versatile analysis widely used for mapping the location and identity of atoms in a sample material [127,128].

A fine electron beam is focused on the sample to a small point and it can be scanned over it in a raster pattern by exciting scanning deflection coils. Scattered electrons are detected and their intensity plotted as a function of probe position to form an image. Although the operating principle of a STEM is similar to the one of the SEM, the STEM requires a thinned, electron transparent specimen instead of a bulk sample typically used for the SEM analysis. In this respect, the most commonly used STEM detectors are placed after the sample and detect transmitted electrons [127]. The lens systems used in a STEM are comparable to those in a conventional TEM, since a high-energy beam of electrons is used.

The raster pattern of the beam across the sample makes STEM suitable for High-Angular Annular Dark-Field (HAADF) imaging, and spectroscopic mapping by Energy Dispersive X-Ray Spectroscopy (EDS) [131]. The HAADF mode in STEM allows to obtain atomic-resolution images and it can be used to map the location and species in the sample. Instead, the EDS analysis gives the elemental composition of the sample and even allows one to picture the elemental maps, measuring the electrons emitted from the sample upon excitation from an X-ray. Each element has its characteristic X-ray emission of energies. A detector measuring the signals, which can be successively interpreted, collects the X-rays emitted during the process.

Description of the procedure

To understand the composition and the distribution of Ru and Na particles on the catalyst support surface, as well as their mutual position, the Na-promoted catalysts herein studied have been analysed via Scanning Transmission

Electron Microscopy under high-angle annular dark field mode (HAADF-STEM) and Energy Dispersive X-Ray Spectroscopy (EDS). The experiments were performed with a Titan Themis 200 microscope (FEI) equipped with an X-FEG Schottky field emission gun operated at 200 kV. Samples were prepared by dispersing the catalysts in ethanol; a drop of the suspension was then allowed to evaporate on a holey carbon-coated copper grid.

2.4.3 X-Ray Powder Diffraction

Description of the technique

X-Ray Powder Diffraction (XRD) is a technique used to acquire crystallographic information of a material, by irradiating a material with incident X-rays and then measuring the intensities and scattering angles of the X-rays leaving the material [128,132], as shown in Figure 2.7.

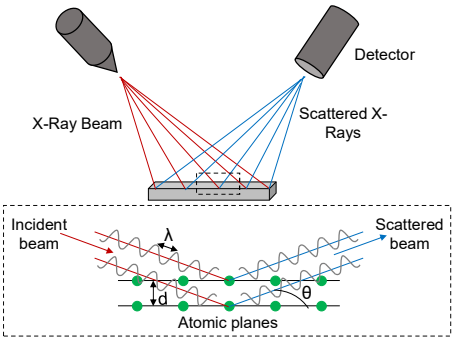

Figure 2.7. Schematic representation of the XRD mode.

The output of an XRD scan is a spectrum with the y-axis being the intensity and the x-axis being 2θ, where θ is the angle of incident X-rays on the sample. The diffraction from a crystal follows Bragg's law:

$$n\,\lambda = 2\,d\,sin\theta \qquad 2.2$$

Where n is an integer called diffraction order, λ the wavelength of the radiation, d is the spacing between crystal planes in the material, and θ is the angle of the incident light (see Figure 2.7).

Various crystal planes and phases can be attributed to each value of θ, then at each peak. Furthermore, the height and width of the peaks can provide further information about the relative amounts of each crystal type [128,132].

In application to catalysts, XRD is particularly useful to determine the average size of metal particles in a catalyst sample using the Scherrer equation:

$$L = \frac{K\,\lambda}{\beta\,cos\theta} \qquad 2.3$$

Where K is a constant, usually assumed to be ~0.9 [133], β is the full-width half-max (FWHM) of the peak of interest, and λ and θ are the same as above. Using this equation, and fitting the peak of the XRD spectrum, we can determine the average particle in the sample.

Furthermore, in application to carbon materials, XRD provides information about the graphitic structural order [133,134]. With this scope, interlayer distance (d_{002}) and mean crystallite size (L_c), indicating the thickness of crystallites along the normal to graphite planes, are calculated from peak 002. The smaller the d_{002} value, the higher the graphitization degree. According to theoretical calculations, d_{002} for the graphite is 0.3354 nm [133].

Description of the procedure

XRD analysis was carried out to determine the crystal phase and crystallinity of each of the Co/Mo-based catalysts here studied. A Bruker D8 Advance Diffractometer was used to record powder XRD patterns using CuKα radiation (λ = 1.5406 Å), with a step size of 0.02°, a 2θ range of 10°- 90° and a time step of 2°min^{-1}. The samples were placed in a silicon substrate zero-background sample holder. The obtained diffraction patterns have been analysed using X'Pert HighScore Plus software and compared to the ICDD database Powder Diffraction Files (PDF-3).

2.4.4 X-Ray Photoelectron Spectroscopy

Description of the procedure

The surface chemical composition of each catalyst was analysed by X-ray Photoelectron Spectroscopy (XPS), using an X-ray photoelectron spectrometer (Thermo ESCALAB 250, USA) equipped with an Al-Kα X-ray source (1486.7 eV). The bond energies were referenced to the adventitious C1s line (284.6 eV). The error in the determination of electron binding energies

and the line widths did not exceed 0.2 eV. The C1s, O1s, N1s, Ru3d and Na1s envelopes were curve-fitted using Gaussian component profiles using the Origin peak-fitting software. A Shirley baseline was used for sloping backgrounds.

2.4.5 Temperature Programmed Reduction

Description of the technique

The temperature-programmed reduction (TPR) is a material characterisation process commonly used in heterogeneous catalysis to characterise metal oxides catalysts under varying thermal conditions. The key principle is to heat the sample at a programmed heating rate, generally linear, in a reducing atmosphere, such as H_2, and to record the H_2 consumption as a function of the temperature using a quadrupole mass spectrometer under ultrahigh vacuum conditions. The resulting TPR profile contains qualitative information on the oxidation state of the reducible species present in the catalyst sample, which allow determining the optimal temperature to reduce the precursor metal oxide into active metal for specific reactions.

Description of the procedure

TPR studies, between 25°C and 700°C, with a temperature ramp of 10°C·min^{-1}, using a 25 cm^3·min^{-1} (STP) flow of 5% vol H_2 balanced in argon (Ar), were carried out in the same apparatus used for TPD experiments.

2.4.6 Inductively Coupled Plasma Mass Spectrometry

Description of the technique

Inductively coupled plasma mass spectrometry (ICP-MS) is an elemental analysis technology capable of detecting low and ultra-low concentrations (*i.e.* in the ppb and ppt range) of most of the periodic table of elements [128,135]. In application to catalysis, this technique is widely used to determine the elemental composition of a catalyst, hence its metal content.

The ICP is an ionisation source that atomises the sample into its constituent elements, which are in turn transformed into ions detectable by the MS. It mostly uses noble gases as plasma gas, typically Ar [135].

The fundamental parts of an ICP-MS are schematically represented in Figure 2.8. This includes: i) an introduction system to carry the sample to the nebuliser, ii) a spray chamber in which the sample is nebulised, iii) a plasma torch to ionise the sample, iv) an interface in which a small amount of the free ions generated by the plasma are transmitted to a quadrupole mass spectrometer, and v) an electron-multiplier detector [135].

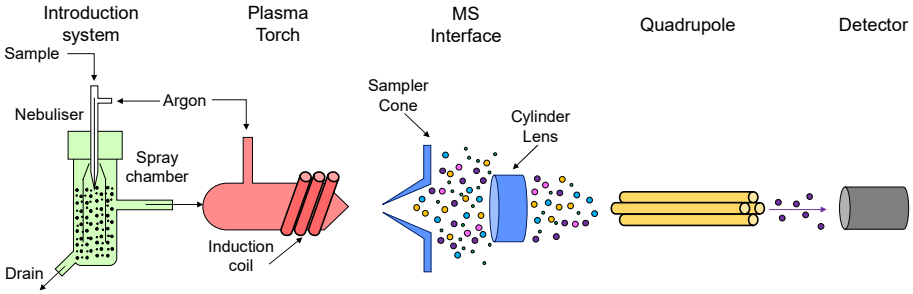

Figure 2.8. Schematic of an ICP-MS system.

Description of the procedure

The metal loading of both un-promoted and Na-promoted catalysts was determined via Inductively Coupled Plasma Mass Spectrometry (ICP-MS). With this scope, samples were firstly leached in hot aqua regia (*i.e.* HCl/HNO_3 mix) for 48 h to dissolve the carbon substrate and analysed using a Thermo Scientific X-Series2 ICP-MS.

2.5 Hollow fibre-based catalytic reactors

2.5.1 Development of the hollow fibre-based reactors

Asymmetric 4-channel α-Al_2O_3 HF substrates were fabricated using the phase inversion technique, followed by sintering at high temperatures [118].

In order to obtain an HF module, 10 HFs were glued together using a high temperature ceramic adhesive (Ceramabond 503, AREMCO). The HFs were first bound into a layer of four fibres and two layers of three fibres and then the layers were bound together. The module was left to air dry for 1 h and then

step cured at 100°C for 1.5 h, 250°C for 1.5 h, 400°C for 1.5 h and 600°C for 1.5 h. The schematic representation of a single HF unit and the HF module is shown below.

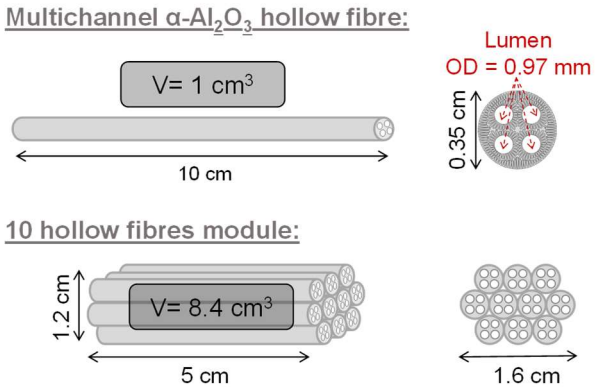

Figure 2.9. Schematic representation of the HF unit and the HF module.

To use the HFs as catalyst support, the carbon xerogels were deposited in their substrate via the sol-gel method, following the same procedure adopted to synthesise the carbon xerogels, *i.e.* i) deposition of the xerogels' precursors solution, ii) gelation, iii) curing and drying, and iv) carbonisation and eventual post-synthesis activation treatment. The amount of carbon deposited in the HFs substrate was calculated by measuring the difference in weight of both the single HF unit and HF module before and after the carbon xerogel deposition. Note that prior to their impregnation with the xerogels' precursors solution, the HFs were wrapped with Teflon tape to avoid xerogels' deposition on their outer surface.

The impregnation of 10 cm long HFs with the Ru-based catalysts solution was carried out by pipetting the same solutions used for the carbon xerogels' impregnation and following the same procedure. Based on the amount of carbon deposited in the HF substrate, the volume of both the $Ru(NO)(NO_3)_3$ solution and 1M water solution of NaOH were calculated. A schematic diagram of the deposition of a Ru-based catalyst on the HF via the sol-gel method and incipient wetness impregnation is shown in Figure 2.10. The same procedure was used to impregnate the HF module with a Co/Mo-based catalyst. Again, based on the amount of carbon deposited in the HF module substrate, the

volume of Co/Mo catalyst solution required to achieve a metal loading of 1.5 wt. % was calculated.

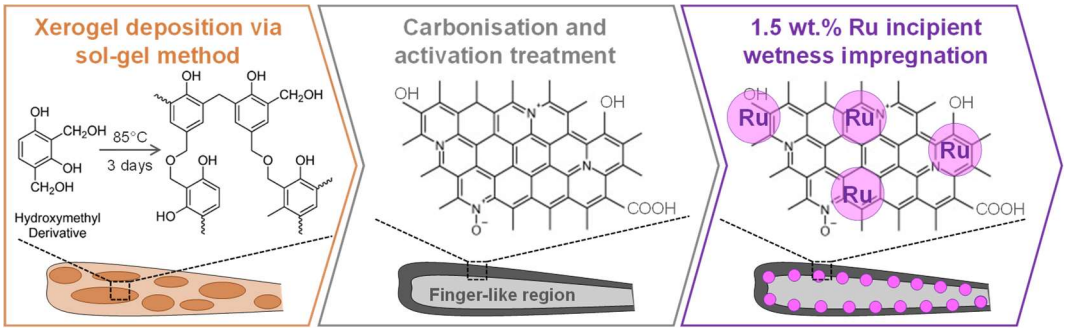

Figure 2.10. Schematic diagram of the deposition of Ru-NCX into the Al_2O_3 HF substrate via the sol-gel method and the incipient wetness impregnation.

The so-prepared catalytic reactors will be named HF reactors (HFRs). By measuring the difference in weight of the HF substrate before and after the catalyst impregnation, the catalyst loading for the Ru-based HFR was calculated to be 30 mg, whereas that of the Co/Mo-based HFR was calculated to be 150 mg.

2.5.2 Development of the hollow fibre Pd-based membrane reactor

A schematic overview of the experimental procedure followed to develop HF Pd-based membrane reactor (MHFR) is shown in Figure 2.11.

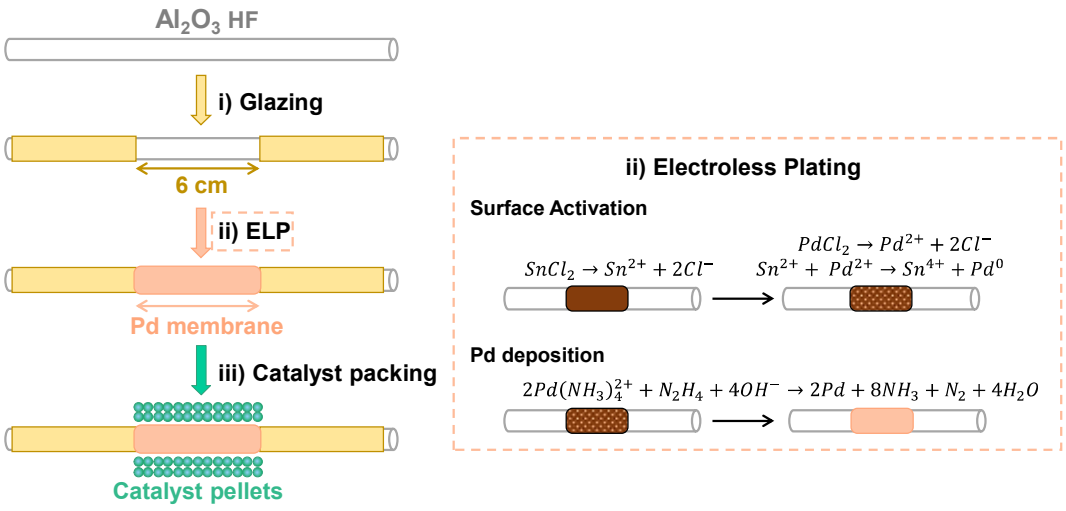

Figure 2.11. Schematic overview of the MHFR development.

Before the deposition of the Pd membrane, the outer surface of a 19 cm long HF, except for the central 6 cm, was coated with a gas-tight glaze in order to block the pores of that area sintered at 900°C for 30 min (see i) in Figure 2.11).

After the glazing, the HF was cleaned by sequential washings with ethanol and water for 30 min and were then dried overnight at 120°C.

The Pd membrane was deposited on the outer surface of the asymmetric 4-channel α-Al_2O_3 HF substrate through electroless plating (ELP) (see ii) in Figure 2.11), as described by Paglieri and Way [136], where the ELP is an autocatalytic technique in which a conductive or a non-conductive surface is coated with a metallic film by the reduction of metal salt complexes (*i.e.* ammine complexes) induced by a reducing agent (*i.e.* hydrazine) [106,108].

The preparation of the Pd membrane on the HF substrate involved two steps, such as surface pre-treatment via sensitisation and activation of the support (*i.e.* HF substrate) and plating of a Pd layer. In the surface activation, Pd seeds are deposited on the HF outer surface, since they act a catalyst in the plating step fastening the formation of the membrane [106]. The HF substrate was activated with Pd seeds via sensitisation in an acidic tin (II) chloride ($SnCl_2$) solution, followed by activation in an acidic palladium (II) chloride ($PdCl_2$) solution. The formation of the Pd seeds on the surface of the HF occurs according to the following reactions (2.4), *i.e.* dissociation of $SnCl_2$ and $PdCl_2$ into Sn^{2+} and Pd^{2+} cations, respectively, and deposition of Pd seeds by a redox reaction between Sn^{2+} and Pd^{2+}:

$$\begin{aligned} SnCl_2 &\rightarrow Sn^{2+} + 2Cl^- \\ PdCl_2 &\rightarrow Pd^{2+} + 2Cl^- \\ Sn^{2+} + Pd^{2+} &\rightarrow Sn^{4+} + Pd^0 \end{aligned} \qquad 2.4$$

As schematically shown in Figure 2.12A, the sensitisation/activation process was carried out by immersing the glazed HF substrates sequentially in five chemical baths: i) acidic $SnCl_2$ solution, ii) deionised water, iii) acidic $PdCl_2$ solution, iv) 0.01 M hydrochloric acid (HCl) solution, and v) deionised water. The sensitisation/activation process was repeated for 6 cycles. The composition of each bath is presented in Table 2.1.

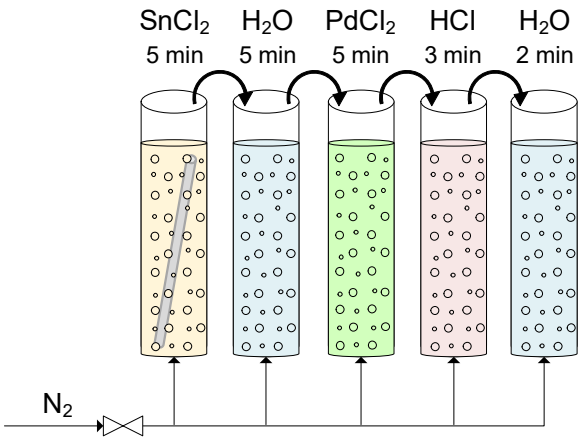

Figure 2.12. Sequential baths for sensitisation/activation process.

Deionised water was used to avoid the contamination of the activation bath (*i.e.* $PdCl_2$) with the sensitisation bath (*i.e.* $SnCl_2$) first, and then to avoid the contamination of the plating bath with both sensitisation and activation baths. Likewise, HCl was used to dissolve away excess tin and tin oxides after performing the sensitizing-activation procedure [136]. All chemical baths were homogenised using compressed N_2. The use of N_2 also ensured the stability of the Sn sensitisers during the sensitisation/activation process, by avoiding their oxidation, which is known to affect their efficiency [136].

Table 2.1. Composition of sensitisation, activation and plating bath solutions.

Step	Compound	Concentration
Sensitisation	$SnCl_2$	1 g·L^{-1}
	HCl (37%)	1 ml·L^{-1}
Activation	$PdCl_2$	0.1 g·L^{-1}
	HCl (37%)	1 ml·L^{-1}
Rinsing	HCl	0.01 M
Electroless Plating	$Pd(NH_3)_4Cl_2$-H_2O	4 g·L^{-1}
	Na_2EDTA-$2H_2O$	40.1 g·L^{-1}
	NH_3-$2H_2O$ (28%)	198 ml·L^{-1}
	N_2H_4 (1M)	5.6 ml·L^{-1}

Successively, the two ends of the glazed HF were closed with Teflon tape to prevent Pd deposition prior to immerging the HF substrate in the ELP solution. The ELP solution was prepared according to the composition presented in

Table 2.1 and left to stabilize overnight before being used [137]. The volume of the ELP solution was fixed at 5.5 mL per cm^2 of substrate surface area and the ELP procedure was performed twice. To obtain a uniform deposition of the membrane during the ELP, the solution was agitated with N_2. Furthermore, the plating temperature was controlled at ~ 60-70°C, in order to deposit metallic Pd layers onto the activated surface, using a hot plate stirrer. Note that the wide temperature range of the ELP solution can be explained by the failure of the heating system in keeping the temperature constant at 60°C. The preposition of the Pd on the surface of the HF takes place according to reaction (2.5):

$$2Pd(NH_3)_4^{2+} + N_2H_4 + 4OH^- \rightarrow 2Pd + 8NH_3 + N_2 + 4H_2O \qquad 2.5$$

Finally, as it can be seen in point iii) of Figure 2.11, a bed of catalyst, synthesised as earlier described in Section 2.1 and Section 2.3, was packed around the Pd membrane.

2.6 Characterisation of the hollow fibre-based catalytic reactors

2.6.1 Scanning Electron Microscopy and Energy Dispersive X-Ray Spectroscopy

Description of the procedure

The morphology of the HF substrate, after the carbon xerogel deposition and the catalyst impregnation, was studied using a Zeiss Crossbeam 550 SEM. The FIB probe voltage and current were 30 kV and 50 pA, respectively, and the working distance was set to 5.5 mm. EDS mapping using an Oxford Instruments X-Max 150 silicon drift detector, with an accelerating voltage of 30kV and a beam current of 50 pA, studied the elemental composition of the samples.

2.6.2 Mercury Intrusion Porosimetry

Description of the technique

Porosimetry is a term associated with the estimation of pore volume, size, and distribution, and density of a material. Mercury (Hg) porosimetry is widely used

in the catalyst for determining the pore size and pore volume of catalyst supports. Since Hg is a non-wetting liquid and will not spontaneously penetrate pores by capillary action, it needs to be forced into the pores applying an external pressure, which is inversely proportional to the pore size [138].

The Washburn Equation relates the applied pressure to pore diameter using physical properties of the non-wetting liquid (*i.e.* Hg):

$$D_P = \frac{-4\,\gamma\,cos\varphi}{P} \qquad 2.6$$

Where D_P is the pore diameter, P is the applied pressure, γ is the surface tension of mercury (*i.e.* ≈ 0.56 N/m), and φ is the contact angle between mercury and the sample (140° is recommended) [139].

Description of the procedure

A detailed assessment of the pore structure and porosity of the HF, before and after catalyst impregnation, was carried out by Hg intrusion porosimetry (PoreMaster, Quantachrome). Hg intrusion data were collected over an absolute pressure range from 5.5x10^3 to 3.5x10^8 Pa and with a set stabilization time of 10 s. Prior to the Hg intrusion analysis, HFs were broken into sections of approximately 5 mm in length.

2.6.3 Scanning Electron Microscopy

The morphology of the Pd membrane after the reaction experiment was studied via SEM, using the same experimental apparatus adopted for characterising the carbon xerogels, *i.e.* a Jeol Jsm-it100 SEM, operated at 15kV. The samples were coated with a thin layer of gold (*i.e.* 15 nm) and the working distance ranged between 16 nm and 23 mm.

2.7 Ammonia decomposition reaction

2.7.1 Experimental apparatus

2.7.1.1 Packed Bed Reactor and Hollow Fibre Reactor

The experimental apparatus used to carry out the NH_3 decomposition reaction, shown in Figure 2.13, consisted on: i) one reactor unit (*i.e.* PBR, HFR for a

single HF for Ru-based catalysts or HFR for a module of HFs for Co/Mo-based catalysts), ii) a reactor furnace (Elite Thermal Systems Limited. Model No: TSV12/32/150), iii) a network of electrical line heaters, iv) a gas delivery system and vi) a mass spectrometer (EcoSys-PTM Mass Spectrometer).

NH_3 condensation within the lines was prevented by a network of electrical line heating tape and thermal insulating fabric, which kept the line temperatures above 150°C. The temperature of each of these lines was monitored using several k-type thermocouples distributed throughout the equipment. A computer was also connected to the mass spectrometer to get real-time readings of the gas composition circulating in the system.

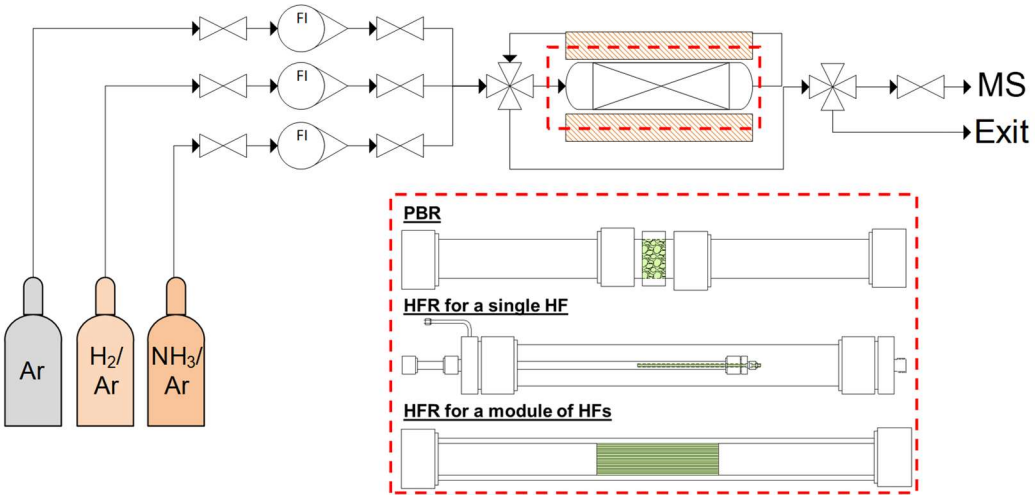

Figure 2.13. Schematic process diagram of the experimental rig for PBR and HFRs units.

Note that the HFR designed in this work for a single HF unit (see Figure 2.13) is the first of his type. In this respect, the use of a graphite ferrule, which guarantees a perfect seal and give a greater accuracy for the mass spectrometry readings, allows multiple uses of the same reactor, contrary to the HFRs employed so far, which have been sealed using epoxy resin and were single-use. Furthermore, the features of the HFR used in this work made it possible to load smaller impregnated fibres while guaranteeing that the samples do not contain traces of epoxy.

2.7.1.2 Hollow Fibre Membrane Reactor

The experimental apparatus used to carry out the NH_3 decomposition reaction, shown in Figure 2.14, consisted on: i) one MHFR reactor unit, ii) a network of

electrical line heaters, iv) a gas delivery system and vi) a mass spectrometer (EcoSys-PTM Mass Spectrometer). The reactor was heated up using an electrical line heater, which was controlled by an analogue power controller (Electrothermal™), and thermal insulating fabric, tightly wrapped around the reactor.

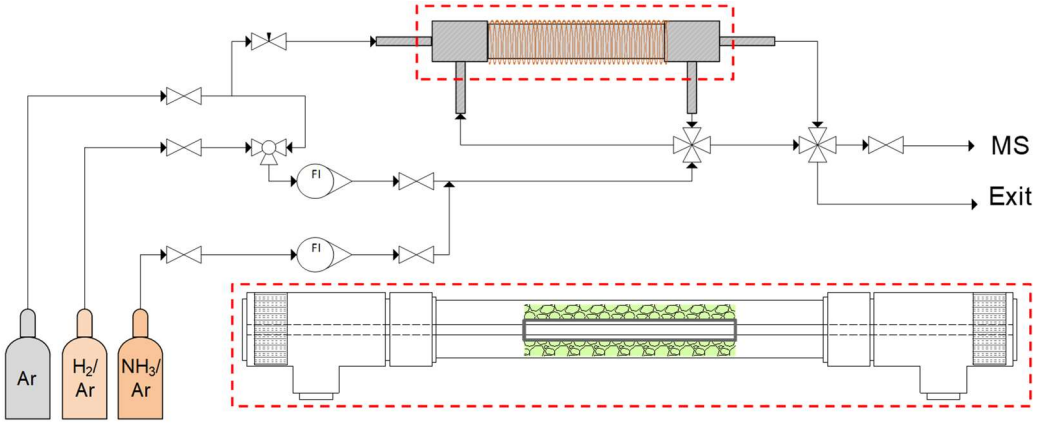

Figure 2.14. Schematic process diagram of the experimental rig for the MHFR reactor unit.

NH_3 condensation within the lines was prevented by a network of electrical line heating tape and thermal insulating fabric, which kept the line temperatures above 150°C. The temperature of each of these lines was monitored using several k-type thermocouples distributed throughout the equipment. The HF was concentrically fixed inside a stainless steel tube using epoxy resin, and the sealings were kept outside the heating zone due to their low thermal stability.

2.7.2 Experimental procedure

2.7.2.1 Packed Bed Reactor and Hollow Fibre Reactor

The catalyst loading for the reaction experiments was i) 300 mg when using the PBR, and ii) 30 mg and 150 mg when using the HFR for a single HF or for a module of HFs, respectively. The whole PBR experiment has been designed in such a way that internal and external diffusion limitations have been minimised. Firstly, to ensure that the internal diffusion limitations present within the PBR do not limit the reaction, the size of catalyst pellets (*i.e.* d_p = 250 μm) we determined assuming the Thiele modulus (ϕ^2), which is a measure of the ratio of a surface reaction rate to a diffusion rate through a pellet, equal 0.4.

Indeed, it is well known that for small ϕ^2, or ϕ^2< 0.4, the pore diffusion resistance is negligible [140,141]. Then, to avoid external mass transfer limitations, the feed volumetric flow rate (*i.e.* 100 $cm^3 \cdot min^{-1}$) was carefully selected in order to minimise the boundary layer thickness (*i.e.* Reynolds number equal to $4.2X10^{-2}$) [140,141].

Before each catalytic test, Ru-based catalysts and Co/Mo-based catalysts were reduced in-situ at 450°C and 600°C, respectively, under a flow of 50 $cm^3 \cdot min^{-1}$ (STP) of 50 vol% H_2 in Ar. The same reaction conditions were used for all reaction experiments. The NH_3 decomposition was performed at atmospheric pressure, between 100°C to 600°C, using a reactant flowrate of 100 $cm^3 \cdot min^{-1}$ and the following reactant mixture: 10 vol% NH_3 balanced in Ar. The gas mixture used in the reaction studies is custom made by BOC Ltd (UK). The composition of the exit gases was monitored by in-line the mass spectrometer, which was calibrated using pure Ar as a zero gas, and the reaction mixture (10% vol. NH_3 in Ar) as a calibration gas. In addition, the ion currency of both the pure Ar and reaction mixture were used as references to calculate the range between 100% and 0% NH_3 conversion, respectively. The NH_3 conversion, x_{NH3} (%), was estimated using the following equation:

$$x_{NH_3} = \frac{C_{NH_{3_{in}}} - C_{NH_{3_{out}}}}{C_{NH_{3_{in}}}} \times 100 \qquad 2.7$$

The turnover frequency (TOF) of each catalyst herein studied was estimated assuming that the metallic phase is responsible for the catalyst activity. The following equation was used to calculate the TOFs:

$$TOF = \frac{\dot{F_{NH_3}}}{n_{Ru}} \times \frac{1}{D} \qquad 2.8$$

Where $\dot{F}_{NH_3}$ is the molar flowrate of the NH_3 converted, n_{Ru} is the Ru loading in moles, which depends on both the metal and catalyst loadings (*i.e.* n_{Ru} = (catalyst loading x Ru loading)/Ru molecular weight), and D is the metal dispersion.

In order to study catalysts' stability, long-term reaction experiments were performed at 450°C for the both the Ru-based and Co/Mo-based catalysts

when using the PBRs (*i.e.* 10 h and 100 h, respectively) and the HFRs (*i.e.* 100 h and 300 h, respectively). It should be noted that longer stability tests were carried out for Co/Mo-based catalysts, as there is no information in the literature on their thermal stability during the NH_3 decomposition reaction, contrary to the Ru-based catalysts that are the most studied for this reaction.

Furthermore, ten thermal shock experiments were performed at atmospheric pressure and at 450°C to assess the effects of frequent start-up and shutdown cycles on the catalytic activity of Co/Mo-NCX and its peeling off resistance. During the thermal shock experiments, the HFR was heated using a ramp rate of 20°C·min^{-1}, reaching 450°C in approximately 20 min. Note that these experiments were only performed for Co/Mo-NCX, which is considered the most suitable catalyst candidate for this technology due to its lower overall cost compared to Ru/Na-NCX.

2.7.2.2 Hollow Fibre Membrane Reactor

The catalyst loading for the MHFR experiment was 2 g. Before the catalytic test, the Ru/Na-based catalyst was reduced in-situ at 450°C under a flow of 50 cm^3·min^{-1} (STP) of 5 vol% H_2 in Ar. Furthermore, Ar was flown through the membrane throughout this process in order to avoid damaging the Pd membrane due to the α-β Pd phase transition (*i.e.* T < 300°C, P < 20 atm, H_2 flow) [106,109,110]. The NH_3 decomposition was performed at atmospheric pressure, between 300°C to 450°C, using the same reactant gas mixture and flowrate of the other reaction experiments. H_2 produced in the NH_3 decomposition reaction was separated by means of the Pd membrane deposited on the outer surface of the HF, using a co-current flow of Ar (*i.e.* 100 cm^3·min^{-1} (STP)) as sweep gas to create a concentration gradient across the Pd membrane. The H_2 recovery index was calculated as the ratio between the permeated H_2 flow and the sum of the permeate and retentate H_2 flows:

$$R_{H_2}\,(\%) = \frac{\dot{V}_{H_{2,P}}}{\dot{V}_{H_{2,P}} + \dot{V}_{H_{2,R}}} \times 100 \qquad 2.8$$

Where $\dot{V}_{H_{2,P}}$ and $\dot{V}_{H_{2,R}}$ is the flowrate of the H_2 in shell and lumen of the reactor, respectively.

Chapter 3 Results and Discussion Part I: Catalysts' supports

This chapter provides a detailed description of the physical, chemical and structural properties of the carbon xerogels. Particularly attention was paid to understanding how the CO_2 activation treatments adopted and the N-doping methods affected carbon xerogels properties. In this respect, as mentioned in the introduction of this thesis, both the activation treatments and the N-doping were performed in order to tune the properties of the carbon xerogels in order to optimise their thermal stability under the reaction conditions, specific surface area, electron conductivity, and basicity, which are known to be favourable for the NH_3 decomposition reaction.

3.1 Description of the carbon xerogels

3.1.1 *Nitrogen adsorption and desorption isotherms at -196°C*

N_2 adsorption and desorption isotherms at -196°C and pore size distributions of carbon xerogels here studied are shown in Figure 3.1A and Figure 3.1B, respectively. According to the IUPAC classification, all supports showed Type IV N_2 isotherms, which are typical for mesoporous materials [120–122]. Moreover, all samples presented a hysteresis loop which is due to capillary condensation, typically observed in pores wider than 4 nm [121]. Hence, ACX_{5h} shows a hysteresis loop Type H4 according to the IUPAC classification, common for micro-mesoporous carbon material with slit-shaped pores. [120–122].

However, the remaining supports show a hysteresis loop Type H2, indicative of a wide pore size distribution [120–122], which is characterised by an almost flat plateau and a steep desorption branch [120]. The extension of the N_2 hysteresis loops shown in Figure 3.1A, in a broad range of relative pressures (*i.e.* P/P_0 between 0.40 and 0.85), indicates the existence of a network of interconnected ink-bottle-shaped or both ends-opened-shaped pores with

different shapes and sizes, ranging from micro- to mesopores, as can be seen in Figure 3.1B [120].

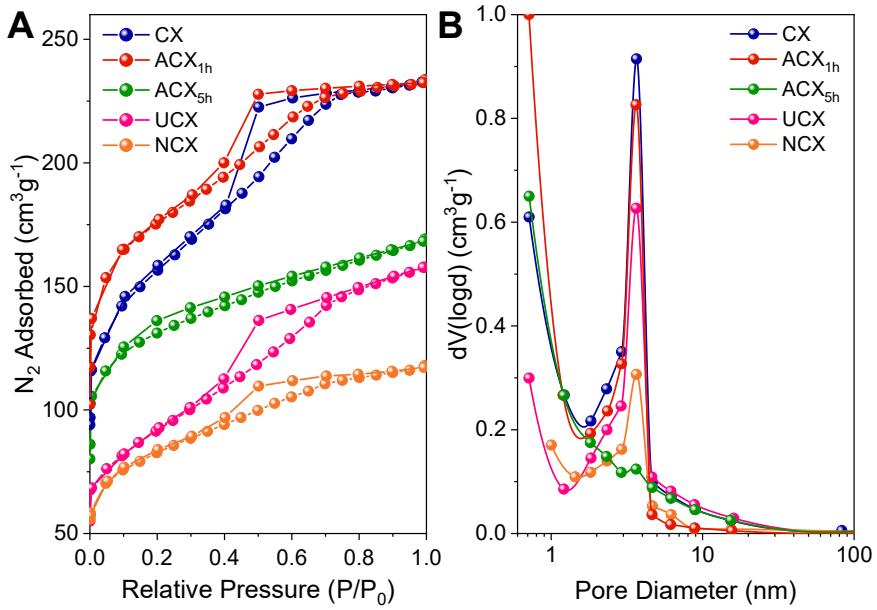

Figure 3.1. (A) N_2 adsorption/desorption isotherms at -196°C and (B) pore size distributions of carbon xerogels here studied.

The duration of the CO_2 activation treatment had distinct effects on the surface area and total pore volume of ACX_{1h} and ACX_{5h}. In this respect, as listed in Table 3.1, ACX_{1h} shows a higher surface area and total pore volume than CX (*i.e.* by 32% and 5%, respectively), whereas ACX_{5h} presents a smaller surface area and total pore volume than CX (*i.e.* by 10% and 30%, respectively).

Table 3.1. Textural and structural properties of carbon xerogels here studied.

Support	S_{BET} ($m^2 \cdot g^{-1}$)	**Pore volume** ($cm^3 \cdot g^{-1}$)		
		Total	*Micropores*	*Mesopores*
CX	1050	0.39	0.20	0.19
ACX_{1h}	1385	0.41	0.23	0.17
ACX_{5h}	960	0.28	0.17	0.11
UCX	550	0.24	0.11	0.13
NCX	325	0.20	0.07	0.13

As can be seen in Figure 3.1A, at low relative pressure (*i.e.* $P/P_0 < 0.1$ bar), ACX_{1h} adsorbed 20% more nitrogen than CX, indicating an increase of the microporosity after 1 h of CO_2 activation treatment. This development of the

microporosity can be explained due to two factors; i) desorption of oxygen surface groups at the entrance of micropores, ii) opening of the micropores due to the reverse Boudouard reaction (*i.e.* $CO_2 + C \rightleftarrows 2\ CO$) [142]. On the other hand, the low volume of N_2 adsorbed by ACX_{5h} confirms the significant decrease in the total pore volume of CX after 5 h of CO_2 activation treatment. This phenomenon could be explained due to the partial crystallisation of the support, which led to a more ordered structure. This result agrees with previous studies, pointing out that carbon xerogels with a more ordered carbonaceous structure present lower surface area and pore volume [143].

It can be observed that the N-doping of carbon xerogels induced a reduction of the N_2 adsorption uptake at very low relative pressure, suggesting a decrease in the total pore volume [120,144]. The fact that the isotherms of both UCX and NCX were simply shifted downwards with respect to CX, and the hysteresis position and shape did not significantly change, indicates that the N-doping reduced the micropores volume of the carbon xerogels but it did not alter their mesopores. Moreover, as reported in Table 3.1, both UCX and NCX exhibited lower specific surface area than CX (*i.e.* by around 50 % and 70 %, respectively). These results can be explained by the addition of heteroatoms to the carbon lattice during the N doping, as well as to the different thermal treatments applied for the synthesis of both UCX and NCX, which are known to affect the structural and textural properties of carbon xerogels [26,48].

Likewise, a comparison between carbon xerogels here studied with those reported in the literature was carried out, as reported in Table 3.2 [82,83,145–150]. It can be noticed that CX shows a higher surface area (*i.e.* 1050 $m^2 \cdot g^{-1}$) than carbon xerogels previously reported in the literature (*i.e.* 600-770 $m^2 \cdot g^{-1}$). This phenomenon could be explained due to the different R/C ratios used to prepare the xerogel precursors solution in this work (*i.e.* R/C = 200) compared to those used in other studies (*i.e.* R/C > 300). These discrepancies are also reflected in the different pH of the xerogel precursors solution, known to depend on the R/C ratio.

Table 3.2. Comparison between carbon xerogels here studied (TW) and those reported in the literature.

Support	R/F	R/C	pH	Carbonisation & Activation	S_{BET} ($m^2 \cdot g^{-1}$)	Ref.
CX	0.50	200	7.11	800°C / 1 h / N_2	950	TW
CX	0.50	1000	-	900°C /3.25 h /N_2	630	[82]
CX650	0.50	-	-	650°C / Ar	663	[150]
CX850	0.50	-	-	850°C / Ar	771	[150]
CX-750	0.50	-	5.80	750°C / N_2	644	[143]
C-xerogel	0.50	-	6.40	800°C / N_2	565-635	[149]
C-xerogel	0.50	-	-	600-1100°C / N_2	600	[145]
CX-Original	0.50	-	6.00	800°C / 2 h / N_2	650	[148]
CX-300	0.50	300	6.80	800°C / N_2	636	[146]
CX-1000	0.50	1000	5.50	800°C / N_2	657	[146]
13CX-UA	1.85	-	6.00	800°C / N_2	687	[147]
28CX-UA	1.85	-	5.50	800°C / N_2	684	[147]
XP350	0.50	350		800°C / 5 h / N_2	655	[83]
ACX_{1h}	0.50	200	7.11	i) 800°C / 1 h / N_2 ii) 800°C / 1 h / CO_2	1384	TW
ACX_{5h}	0.50	200	7.11	i) 800°C / 1 h / N_2 ii) 800°C / 5 h / CO_2	958	TW
AX-1000	0.50	-	5.80	i) 750°C / 1 h / N_2 ii) 1000°C / 2 h / CO_2	1460	[143]
AC-xerogel	1.50	-	-	i) 600-1100°C / 1 h / N_2 ii) 1050°C / 3 h / CO_2	600	[145]
CX-800-4	2.50	1000	-	i) 900°C / 3.25 h / N_2 ii) 800°C / 4 h / CO_2	670	[82]
UCX	0.50	200	6.02	800°C / 5 h / N_2	550	TW
NCX	0.50	200	7.11	i) 800°C / 1 h / N_2 ii) 350°C / 3 h / NH_3	325	TW
URF170	0.50	170	-	800°C / 5 h / N_2	604	[63]
CXU_5.3_700	0.50	-	5.30	700°C / N_2	435	[78]
CXU_6.0_700	0.50	-	6.00	700°C / N_2	432	[78]
CXU_6.9_700	0.50	-	6.90	700°C / N_2	461	[78]
CXU-6.9	0.50	-	6.90	450°C / N_2	406	[84]
XU200	0.50	200	-	800°C / 5 h / N_2	258	[83]

In this respect, as stated by Pekala et al., the R/C ratio can significantly influence the kinetic of the gelation reaction and thus the final properties of the

xerogel [80,151]. In particular, low R/C ratios result in xerogels with small pore sizes and larger surface areas, whereas high R/C ratios lead to xerogels with bigger pores and lower surface areas [151]. Furthermore, Salinas-Torres et al. found that the R/C ratio has a strong influence on the pore texture of the dried xerogels and, therefore on their carbonised counterparts [152]. Instead, UCX surface area (*i.e.* 550 $m^2 \cdot g^{-1}$) is in line with those reported in previous studies (*i.e.* 400-600 $m^2 \cdot g^{-1}$), in which N-doped carbon xerogels were synthesised under the same experimental conditions [63,78,83,84].

3.1.2 Temperature Programmed Desorption

Oxygen surface groups present on carbon xerogels surface were determined by TPD experiments. As it is well known oxygen surface groups decompose into CO_2 and CO at medium and high temperatures [123]. The evolution of CO_2 and CO desorption profiles with the temperature are shown in Figure 3.2A and Figure 3.2B, respectively. As can be seen in Figure 3.2A, CO_2-TPD profiles can be deconvoluted into three components, corresponding to carboxylic acids (*i.e.* peak a: 230 - 300°C), anhydrides (*i.e.* peak b: 400 - 450°C), and lactones (*i.e.* peak c: 530 - 580°C). On the other hand, CO desorption profiles, shown in Figure 3.2B, only exhibited one peak (*i.e.* peak d: 440 - 450°C), which can be associated with the presence of anhydrides on the surface of carbon xerogels [123].

The nature of oxygen surface groups identified in carbon xerogels here studied (*i.e.* carboxylic, anhydride and lactone) agrees with the results of previous works in which the synthesis of carbon xerogels was conducted under similar experimental conditions [78,79,82].

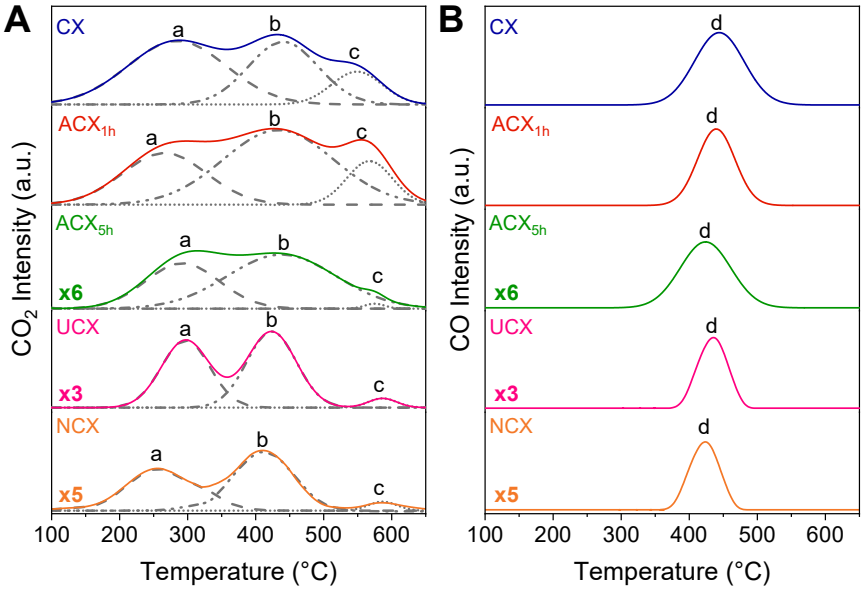

Figure 3.2. (A) CO_2-TPD and (B) CO-TPD profiles of carbon xerogels here studied. CO_2 and CO intensity values scaled to the mass of the sample analysed.

3.1.3 Thermal Gravimetric Analysis in nitrogen atmosphere

The weight percentage of the different functional groups present on the surface of all supports here studied is reported in Table 3.3. Oxygen surface groups represent about 14%, 9%, 3%, 5% and 2% of the total mass of CX, ACX_{1h}, ACX_{5h}, UCX, and NCX, respectively.

Table 3.3. Amount of oxygen surface groups of carbon xerogels here studied.

Support	**Oxygen surface groups** (wt.%)			
	Total	*Carboxylic*	*Anhydrides*	*Lactones*
CX	14.0	3.5	4.3	6.2
ACX_{1h}	9.2	2.1	2.7	4.4
ACX_{5h}	2.9	2.0	0.7	0.2
UCX	4.6	3.2	0.9	0.5
NCX	2.4	1.6	0.7	0.1

The amount of oxygen surface groups presented in CX decreased because of the CO_2 activation treatment. For instance, N_2-TGA experiments showed that ACX_{1h} and ACX_{5h} exhibited 5 wt. % and 11 wt. % less oxygen surface groups than CX, respectively. This behaviour can be ascribed to the exposure of CX to a high temperature during the activation treatment (*i.e.* 800°C). Indeed, thermal treatments at high temperatures (*i.e.* > 700°C) are widely used to

remove functional groups from the carbon surface in order to enhance its physical and chemical properties (*i.e.* basicity and electrical conductivity) [51]. Despite the high temperature activation treatment, desorption of surface groups at low temperature was observed in both ACX_{1h} and ACX_{5h}, which can be explained due to the re-oxidation of the supports after the activation treatment when exposed to the atmosphere.

Likewise, the presence of N heteroatoms in the carbon xerogel caused a decrease in anhydride and lactone surface groups, regardless of the method used. Indeed, only the 0.9 wt. % and 0.5 wt. % of UCX weight were ascribed to anhydride and lactone surface groups, respectively. Likewise, NCX showed only 0.7 wt. % of anhydrides and 0.1 wt. % of lactone groups. For UCX, this behaviour can be explained due to the longer exposure to high temperatures during the carbonisation stage (*i.e.* up to 800°C for 8 h) compared to CX (*i.e.* up to 800°C for 1 h) [153,154]. This behaviour can be further attributed to the formation of various N functionalities during the carbonisation of the N-doped carbon xerogel precursor, which could avoid the formation of certain oxygen surface groups such as lactone surface groups (*i.e* 90% less in UCX than CX) [155,156]. In contrast, the complete absence of lactone groups and the overall decrease of oxygen surface groups in NCX is a consequence of the formation and desorption of amide surface groups during the NH_3/Air activation treatment (*i.e.* R_1-(C=O)-O-R_2 + $NH_3 \rightarrow R_1$-$CONH_2$ + R_2-OH) [74,150,154].

3.1.4 X-Ray Photoelectron Spectroscopy

To prove the efficiency of the N-doping methods used in this work, by confirming the addition of N functionalities to the carbon xerogels' surface, both UCX and NCX were analysed via XPS. The type of N functionalities and their relative amount was then assessed. XPS spectra in the N1s region of UCX and NCX, shown in Figure 3.3A, were deconvoluted into three contributions associated with the presence of N functionalities, including i) pyridine (*i.e.* 399.5–398.5 eV), ii) pyrrole (*i.e.* 400.8–399.8 eV), and iii) graphitic or quaternary nitrogen (*i.e.* 403.0–401.0 eV) [33,79,119,150,157,158].

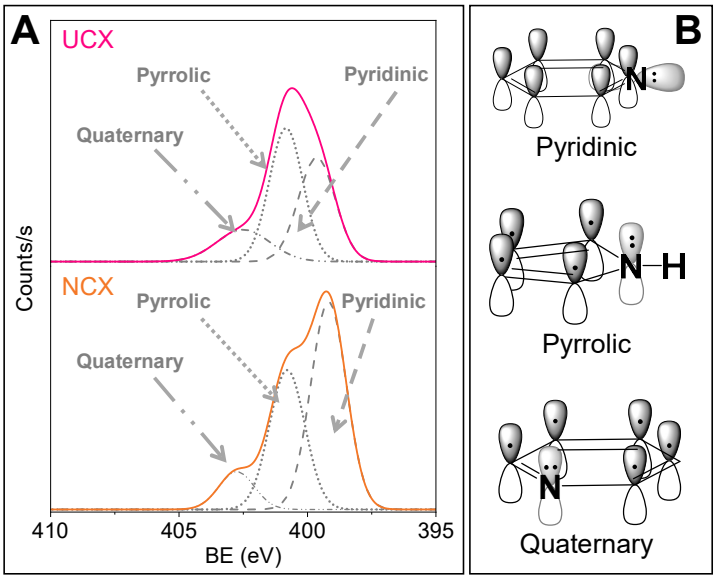

Figure 3.3. (A) XPS spectra in the N1s region of UCX and NCX. (B) Schematic diagram of typical N functionalities.

As schematically represented in Figure 3.3B, pyridinic groups contain sp2-hybridized N atoms located at the edges of graphene sheets, pyrrolic groups have a sp2-hybridized N atom as part of a five-member ring structure, and quaternary N is sp3-hybridized and replace a carbon atom located within a six-member ring structure in the graphene sheet.

As reported in Table 3.4, although UCX and NCX presented the same type of N groups, their total and relative amounts are different. For instance, UCX possessed almost half the amount of groups compared to NCX. Likewise, UCX exhibits higher relative contributions of pyrrolic and quaternary nitrogen (*i.e.* 45% and 23%, respectively), whereas NCX showed more pyridinic nitrogen (*i.e.* 54%).

Table 3.4. Amount of nitrogen functionalities of UCX and NCX determined by XPS.

Support	**Nitrogen groups** (*wt.%*)			
	Tot	Pyridine	Pyrrole	Quaternary
UCX	2.2	0.7	1.0	0.5
NCX	3.9	2.1	1.4	0.4

This result can be justified by the different N-doping methods used to synthesise UCX and NCX. In this respect, Kang et al. found that the relative amount of N functionalities can be controlled by changing the temperature at

which the N doping occurs [150]. Thus, longer exposure to high temperatures during the carbonisation led to a gradual conversion of pyrrolic to pyridinic N, which is consequently converted into quaternary N. Similarly, Abidin et al. reported that the carbonisation temperature significantly affects the formation of the N groups in the carbon xerogel structures [159]. Furthermore, Gorgulho et al. showed that the relative contributions of N groups in a sample are not only affected by the temperature at which N-doped carbon xerogels have been prepared but also by the N-containing precursor used [119].

3.1.5 Thermal Gravimetric Analysis in Air atmosphere

The Air-TGA profiles, and their first derivative curves, of the supports here studied, are shown in Figure 3.4A and Figure 3.4B, respectively. As shown in Figure 3.4A, among all the supports studied, CX shows the greatest drop in mass in air atmosphere, with a final mass loss of 63% at 700°C. On the contrary, UCX exhibits the smallest drop, with approximately 50% of its mass being lost after the treatment at 700°C.

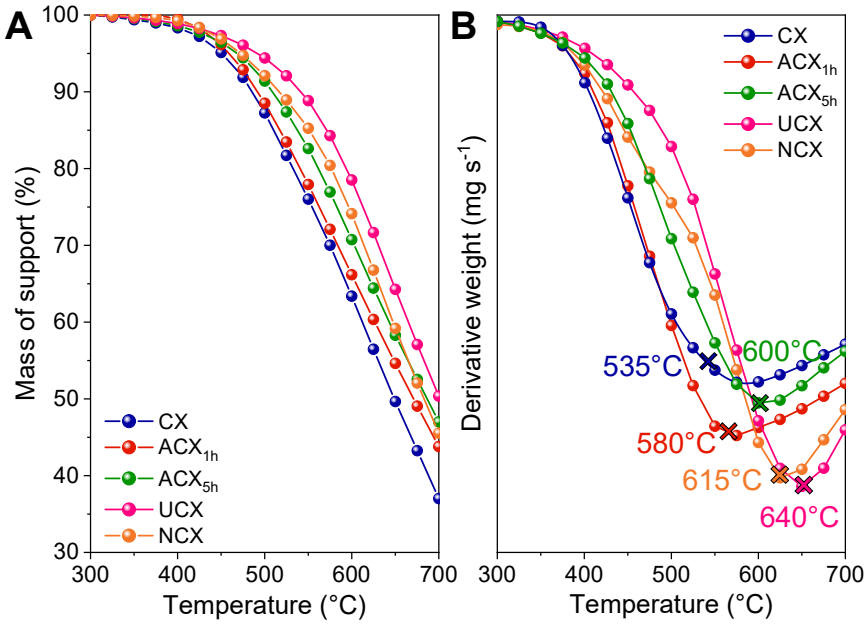

Figure 3.4. (A) Air-TGA profiles and (B) their first derivative curves for carbon xerogels here studied.

It can be noted that after the CO_2 activation treatment, the burning temperature of both ACX_{1h} and ACX_{5h} (*i.e.* 580°C and 600°C, respectively) was higher than that of CX (*i.e.* 535°C). The enhanced thermal stability observed in CO_2

activated carbon xerogels can be explained due to an arrangement of carbon atoms into a more ordered crystal structure. This explanation is in line with the previous work of Zhong et al., which reported that the higher the crystallinity of carbon supports, the higher their thermal stability is [12].

Likewise, both UCX and NCX were associated with higher burning temperatures than CX (*i.e.* 640°C, 615°C, and 535°C, respectively), which suggest that the presence of N atoms on the surface of UCX and NCX enhanced their thermal stability. The positive effect of N doping on the thermal stability of both UCX and NCX can be attributed to the presence of carbon-nitrogen bonds (615 $kJ \cdot mol^{-1}$) which are stronger than carbon-carbon bonds (602 $kJ \cdot mol^{-1}$) [63,78,79]. Similar behaviour was observed by Stohr et al., which reported that N-doped carbon materials exhibit higher oxidation resistance compared to non-doped counterparts [62]. Furthermore, the lower burning temperature observed for NCX compared to UCX can be explained by its larger amount of pyridine groups (see Table 3.4), which have been reported to exhibit lower thermal stability than pyrrole and quaternary N groups [158].

3.1.6 Scanning Electron Microscopy

Scanning Electron Microscopy (SEM) studied the morphology of the different supports. Different top surface SEM pictures from low to high magnification are depicted in Figure 3.5. As reported in the literature, carbon xerogels are composed of interconnected and semi-spherical particles, which form a three-dimensional network [63,146].

As can be seen from the representative images below, the two activation treatments, *i.e.* either in CO_2 or NH_3/Air atmosphere, resulted in carbon xerogels with different textural and structural properties. For instance, after the activation with CO_2, the surface becomes smoother, whereas activation with NH_3 resulted in a more crystalline and shiny surface. Instead, the fact that both ACX_{1h} and ACX_{5h} presented a relatively similar surface morphology to UCX, suggests that both the CO_2 activation treatment and N doping via the co-

precursor method lead to carbon xerogels with similar textural and structural properties.

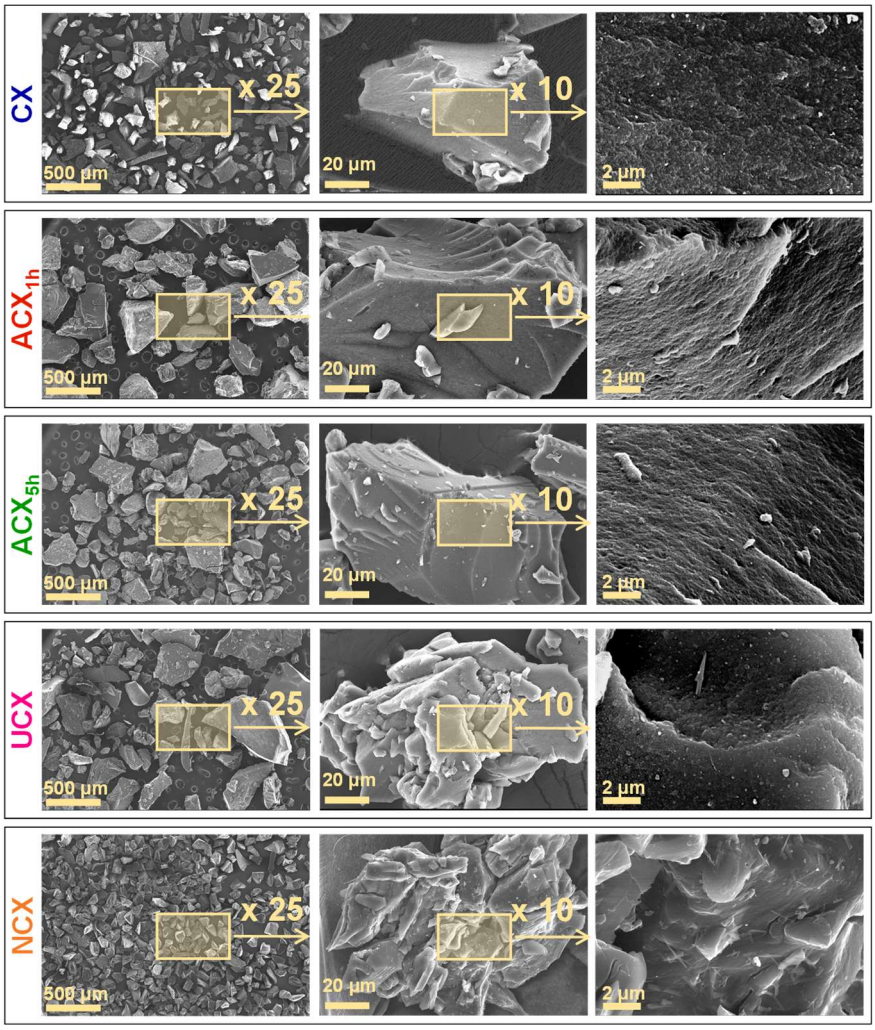

Figure 3.5. SEM images of carbon xerogels at different magnifications.

3.2 Conclusions

The effects of the CO_2 activation of carbon xerogels were investigated for different activation durations, *i.e.* 1 h and 5 h. The specific surface areas and pore volumes of ACX_{1h} and ACX_{5h} were different, depending on the duration of the CO_2 activation treatment. For instance, the 1 h treatment resulted in a higher surface area and pore volume of ACX_{1h} when compared to CX, whereas the 5 h treatment had a detrimental effect on the textural and structural properties of ACX_{5h}. Despite this, as evinced by the Air-TGA and TPD result, the 5 h CO_2 activation treatment offered the advantages of enhanced thermal

stability and basicity of ACX_{5h} when compared to both ACX_{1h} and CX (*i.e.* 5-12% higher burning temperature and 70-80% less oxygen surface groups).

The N-doping of carbon xerogels resulted in the production of carbon xerogels with a lower surface area, less developed microporosity, and enhanced thermal stability and basicity when compared to non-doped counterparts. Changing the N-doping method from the co-precursor method (*i.e.* UCX) to the post-synthesis NH_3/Air activation (*i.e.* NCX) lead to the introduction of different N functionalities on the carbon xerogel surface. According to XPS spectra deconvolution, the pyrrolic N and quaternary N functionalities are predominant in UCX, whereas pyridinic N are predominant in NCX. This, in turn, affected the thermal stability of both UCX and NCX, being the former more stable than the latter due to the fewer pyridine groups on its surface.

Chapter 4 Results and Discussion Part II: Ruthenium-based catalysts

This chapter includes a detailed description of both the un-promoted and Na-promoted Ru-based catalysts, with a particular focus on how the properties of the different carbon xerogels used affected their catalytic activity. In addition, the effect of the promoter on the catalysts' performance during the NH_3 decomposition reaction is analysed in this chapter as well.

4.1 Description of the ruthenium-based catalysts

4.1.1 Scanning Transmission Electron Microscopy and Energy Dispersive X-Ray Analysis

Conventional STEM-HAADF images and corresponding EDS elemental maps of the Na-promoted catalysts herein studied are shown in Figure 4.1. From a visual inspection of the elemental maps, it can be seen an even distribution of both Ru and Na nanoparticles on the catalyst's support surface, indicating the absence of apparent Ru aggregates.

Based on Tennison et al. work, metallic Na and sodium oxide (Na_2O) can be found in three different positions with respect to the Ru; i) absorbed in the bulk of the Ru particles, ii) around the Ru particles forming "hot rings", iii) decorating the surface of Ru particles [92]. However, looking at the STEM/EDS images in Figure 4.1, it is difficult to determine the exact relative position of Na oxide with respect to Ru particles. In this respect, it can be assumed that both the Na and Na_2O can be found in any of the three different positions identified by Tennison et al.

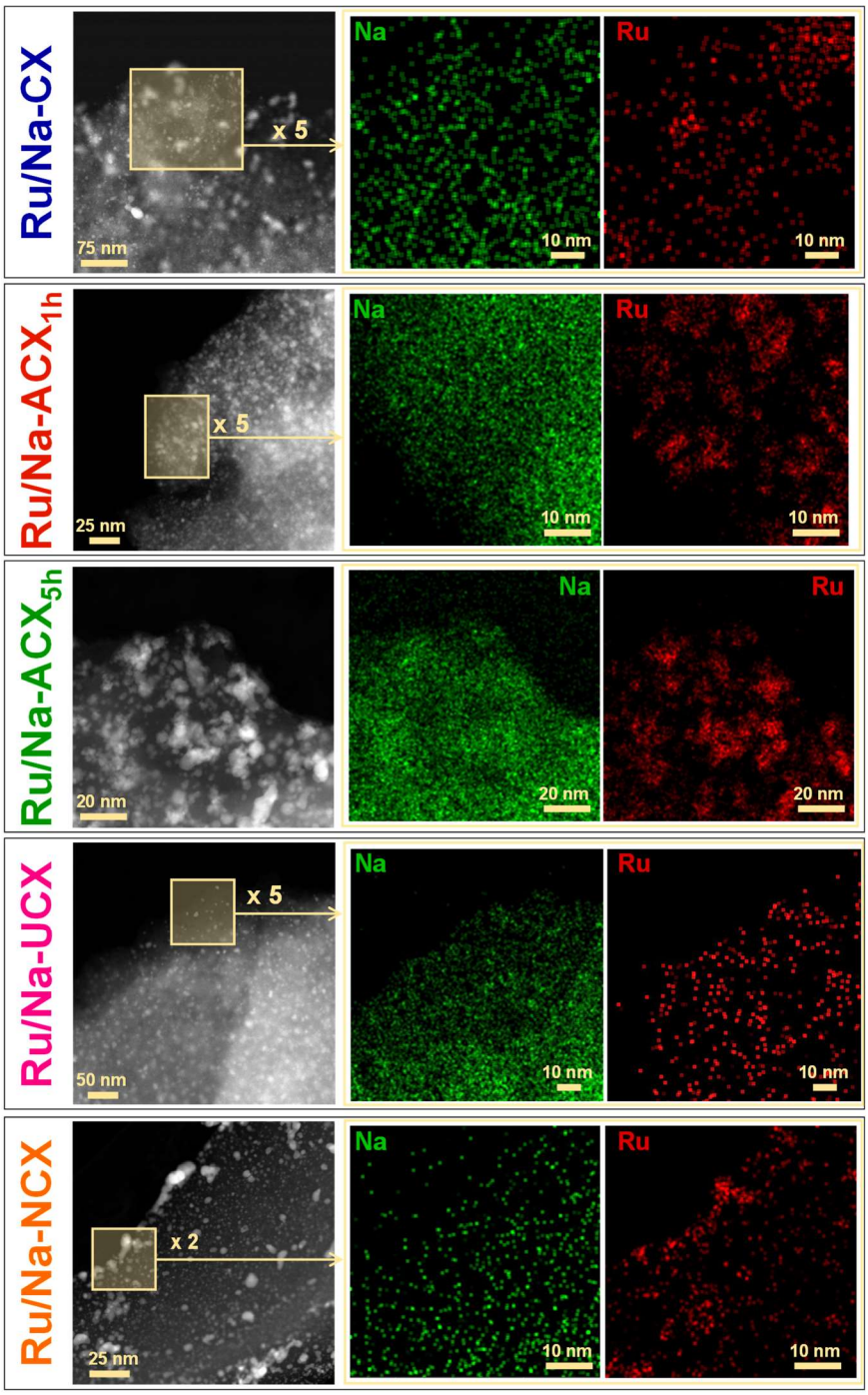

Figure 4.1. Representative STEM-HAADF images and corresponding EDS elemental maps taken from the Na-promoted Ru-based catalysts after the reaction.

4.1.2 Transmission Electron Microscopy

Representative TEM images of un-promoted and Na-promoted Ru-based catalysts here studied, before and after reaction, are shown in Figure 4.2 and Figure 4.3, respectively. In addition, Ru particle size distribution histograms before and after the first reaction run, for un-promoted and Na-promoted catalysts, are also shown in Figure 4.2 and Figure 4.3, respectively.

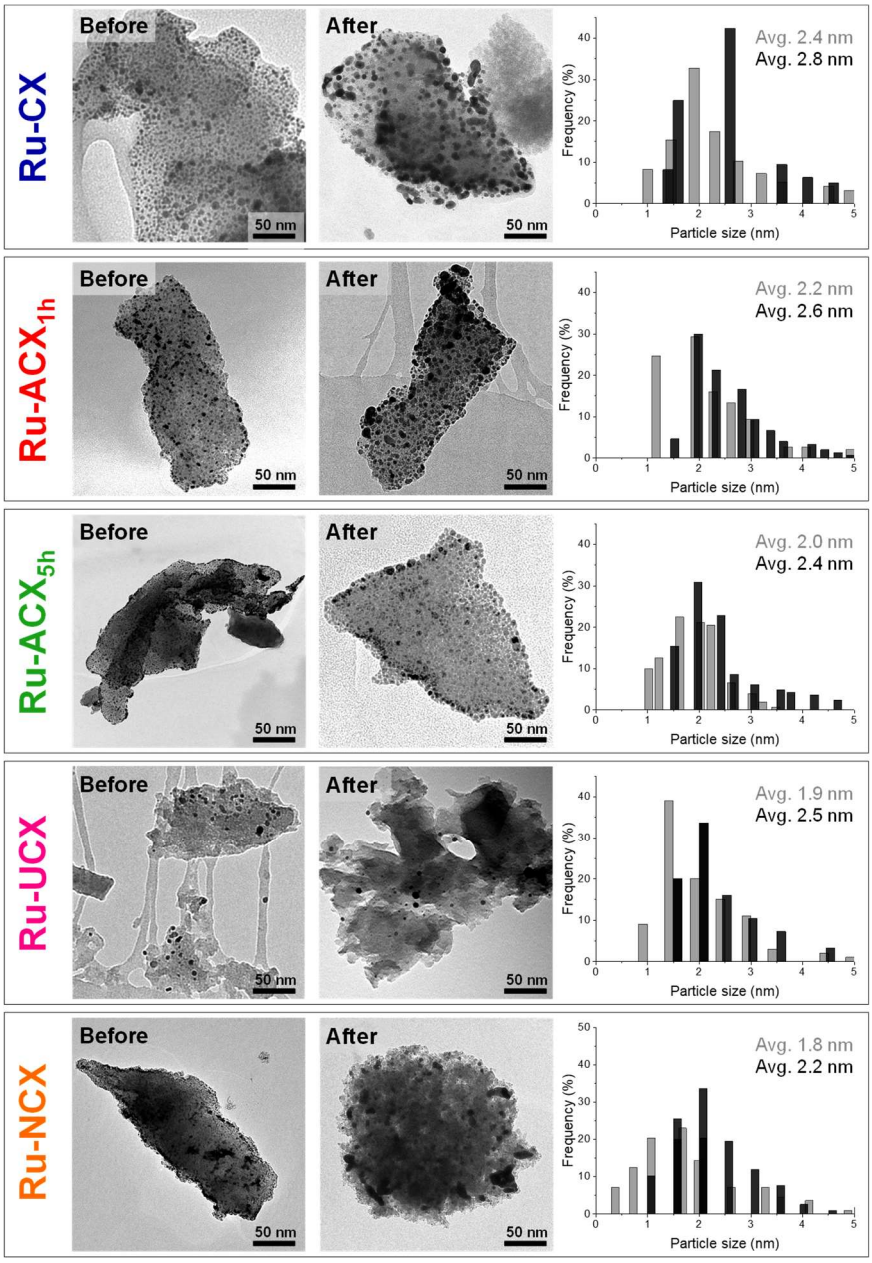

Figure 4.2. TEM images before and after reaction of un-promoted Ru-based catalysts. Right: Particle size distributions before (grey) and after (black) the reaction.

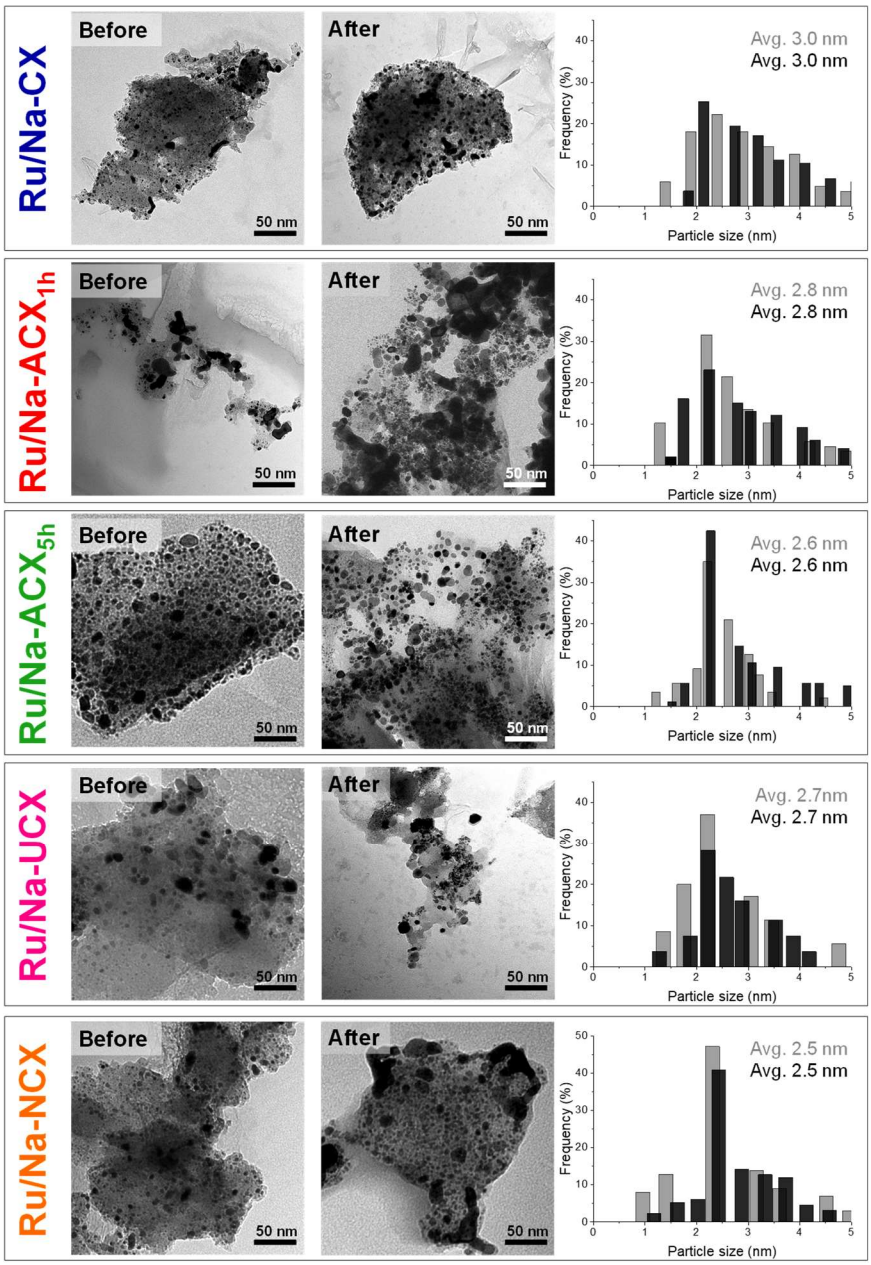

Figure 4.3. TEM images before and after reaction of Na-promoted Ru-based catalysts. Right: Particle size distributions before (grey) and after (black) the reaction.

Likewise, the standard deviation (SD) of Ru particle size distributions has been calculated for all catalysts herein presented. As can be seen from the data reported in Table 4.1, a similar SD trend can be identified for both un-promoted and Na-promoted catalysts before reaction; in this respect, it can be noticed that the catalysts supported on ACX_{5h} and CX always present the narrowest and the widest particle size distribution, respectively. Furthermore, only the two catalysts supported on ACX_{1h} presented a narrower particle size distribution

after the first reaction experiment (*i.e.* SD 25% and 10% lower for Ru- ACX_{1h} and Ru/Na- ACX_{1h}, respectively).

Table 4.1. Ru-based catalysts here studied: Ru average particle size (Dm), SD of Ru particle size distributions, and metal particles dispersion (D(%)) before and after the reaction.

Catalyst	Dm (nm)		SD (nm)		D (%)	
	Before	*After*	*Before*	*After*	*Before*	*After*
Ru-CX	2.4	2.8	0.93	1.06	29.9	26.9
Ru/Na-CX	3.0	3.0	0.89	0.93	27	-
Ru-ACX_{1h}	2.2	2.6	0.82	0.63	33.7	31.3
Ru/Na-ACX_{1h}	2.8	2.8	0.89	0.80	27.6	-
Ru-ACX_{5h}	2.0	2.4	0.56	0.78	35.1	32.1
Ru/Na-ACX_{5h}	2.6	2.6	0.50	0.71	29.4	-
Ru-UCX	1.9	2.5	0.80	1.05	34.9	32.6
Ru/Na-UCX	2.5	2.6	0.69	0.84	29.9	-
Ru-NCX	1.9	2.5	0.80	1.05	36.2	32.9
Ru/Na-NCX	2.5	2.6	0.69	0.84	33.1	-

It is widely accepted that oxygen surface groups can behave as anchoring sites for metal atoms, improving their dispersion throughout the support [34,50,52]. However, as can be seen in Table 4.1, despite Ru-CX presenting the highest amount of oxygen surface groups, it had the largest average particle size and the lowest metal particles dispersion (*i.e.* 2.4 nm and 30%, respectively), compared to the other un-promoted catalysts herein presented. Similar behaviour was observed by Van Dam et al. [50], which concluded that high temperature electron-withdrawing surface groups can weaken the interaction between the metal atoms and the support, facilitating their mobility and agglomeration into larger particles. This agrees with the fact that catalysts with the lowest average particle size, Ru-ACX_{5h}, Ru-UCX, and Ru-NCX also showed the lowest amount of lactone groups.

A similar trend was observed for Na-promoted catalysts; the lower the number of lactone groups, the smaller Ru average particle size. However, notice that the Ru average particle size of Na-promoted catalysts was larger than that of

un-promoted ones (*i.e.* 2.6 - 3.0 nm vs 1.8 - 2.4 nm). Despite the low contrast between Ru and Na, which make it very difficult to distinguish Ru particles from Na ones, this behaviour tentatively suggests that metal particles observed in Figure 4.3 are a mixture of Ru and Na atoms.

Furthermore, as shown in Figure 4.2, the Ru particle size distribution of un-promoted catalysts shifted to the right after the first reaction run. The increase in the average size of Ru particles (*i.e.* from 1.8 - 2.4 nm to 2.2 - 2.8 nm) can be explained by the sintering of Ru particles due to the high reaction temperature (*i.e.* 600°C) [89]. In contrast, as it can be seen in Figure 4.3, the Ru particle size distribution of Na-promoted catalysts did not change after the first run of reaction. This strongly suggests that Na oxide must be located around Ru particles, preventing their sintering and agglomeration. This hypothesis is based on Tennison et al. work aforementioned [92] and STEM/EDS analysis discussed before.

4.1.3 Temperature Programmed Reduction

TPR profiles of un-promoted and Na-promoted catalysts are shown in Figure 4.4A and Figure 4.4B, respectively. The interpretation of these profiles has been done using the open literature [34,68,87,90]. As can be seen in Figure 4.4A, three H_2 reduction peaks were observed for the un-promoted catalysts here studied. The first peak observed at low temperature (*i.e.* peak a: 210 - 245°C) corresponds to the reduction of the Ru oxide particles. The fact that reduction temperature here reported is higher compared with those reported in the literature (*i.e.* 130 - 180°C) [42,49,63], suggests a stronger metal-support interaction in the catalysts studied in this work. Similar behaviour was reported by Yin et al., who found that the interaction between the metal and the support can significantly influence the reduction temperature [3]. Moreover, as expected, the reduction temperature of Ru oxide particles increased with their average particle size, indicating that bigger metal particles are more difficult to be reduced.

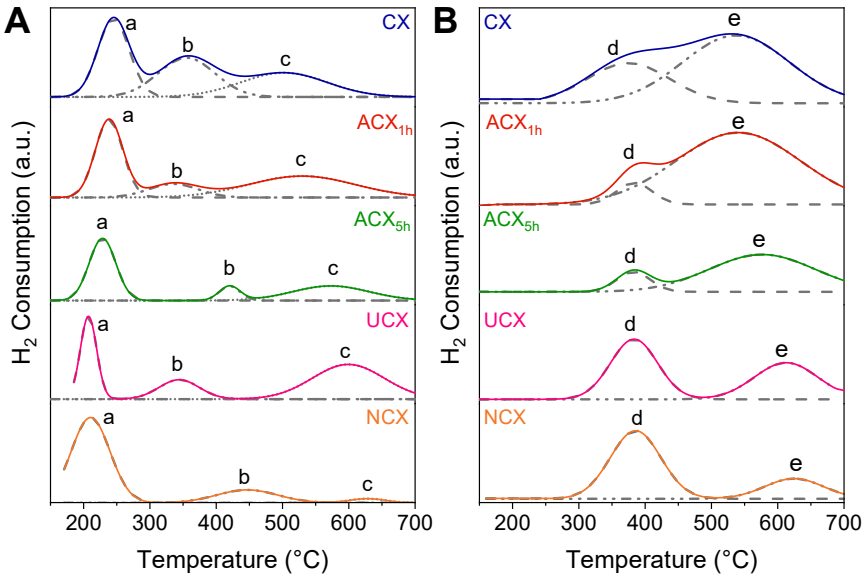

Figure 4.4. Temperature Programmed Reduction profiles of (A) un-promoted and (B) Na-promoted Ru-based catalysts.

The second reduction peak observed at intermediate temperature (*i.e.* peak b: 335 - 450°C), can be explained due to the H_2 from Ru atoms onto the carbon surface. According to Psofogiannakis et al., the H_2 spillover is facilitated when the carbon substrate is decorated with oxygen surface groups [64]. Moreover, Guerrero et al. found out that an increased surface density of carboxylic and lactones groups leads to a significant enhancement of the H_2 spillover [65]. This is consistent with the fact that among all the catalysts Ru-CX, which had the highest amount of carboxylic and lactones groups among all catalysts studied, displayed the highest intensity H_2 consumption peak attributed to the H_2 spillover. Notice that under the NH_3 decomposition reaction conditions the H_2 spillover can occur, resulting in an H_2 rich surface around the ruthenium particles that can affect the catalytic performance.

The third reduction peak observed at high temperature (*i.e.* peak c: 500 - 610°C) corresponds to the partial gasification of the carbon support to produce methane. The temperature range at which this peak is observed is higher than the values reported in the literature [5,6]. In this respect, it has been reported that the extent of the gasification process is determined by the nature of the carbon support. According to Forni et al. [66] and Kowalczyk et al. [67], the gasification process is less pronounced on more crystalline carbon support

structures. This could explain the fact that both CO_2 activation treatment and N doping significantly improved the gasification resistance of Ru-ACX_{1h}, Ru-ACX_{5h}, Ru-UCX, and Ru-NCX.

Unlike un-promoted catalysts, only H_2 consumption peaks corresponding to the reduction of the Ru precursors (*i.e.* peak d: 375 - 390°C) and the partial gasification of the support (*i.e.* peak e: 540 - 630°C) were observed in the TPR profiles of Na-promoted catalysts. This suggests, in accordance with the STEM/EDS and TEM results discussed before, that Na_2O act as a barrier around Ru particles, which avoids the diffusion of H_2 atoms from the metal to the support [68]. Hence, the H_2 consumption peak at the intermediate temperature corresponding to H_2 spillover was not observed in any of Na-promoted catalysts here studied. Moreover, the addition of Na increased in the reduction of the Ru oxide particles and the partial gasification of the support temperatures. This behaviour can be explained due to the electronic promoter effect of Na, which enhances the interaction between Ru particles and the carbon support [13,42]. Likewise, it is important to highlight that the addition of Na improved the thermal stability of Na-promoted catalysts, which allows their use in a wider temperature range.

A schematic diagram reporting the evolution of both the un-promoted and a-promoted catalysts surface during the H_2 TPR experiments is shown in Figure 4.5.

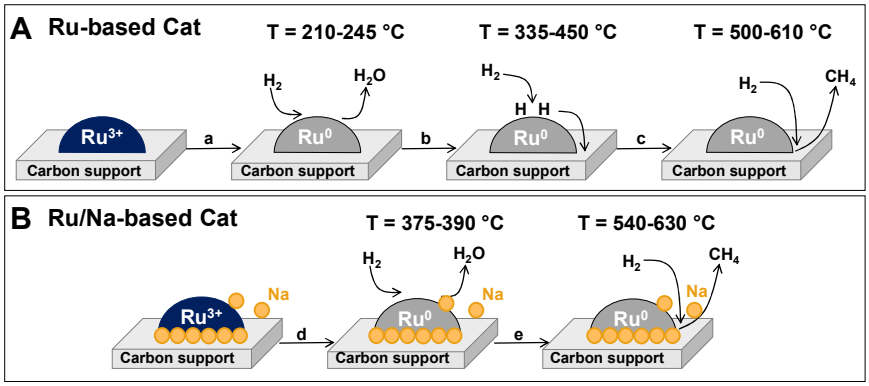

Figure 4.5. Schematic representation of the surface evolution of (A) un-promoted and (B) Na-promoted Ru-based catalysts during TPR experiments.

4.1.4 X-Ray Photoelectron Spectroscopy

XPS spectra of C1s, O1s and N1s regions, for un-promoted and Na-promoted Ru-based catalysts, before their activation, are reported in Figure 4.6A and Figure 4.6B, respectively. The chemical composition of the surface of carbon xerogels here studied is in agreement with the results of previous works [33,63,150,160–163]. As expected, the treatments used to modify the properties of carbon xerogels affected the nature of the chemical components on their surface.

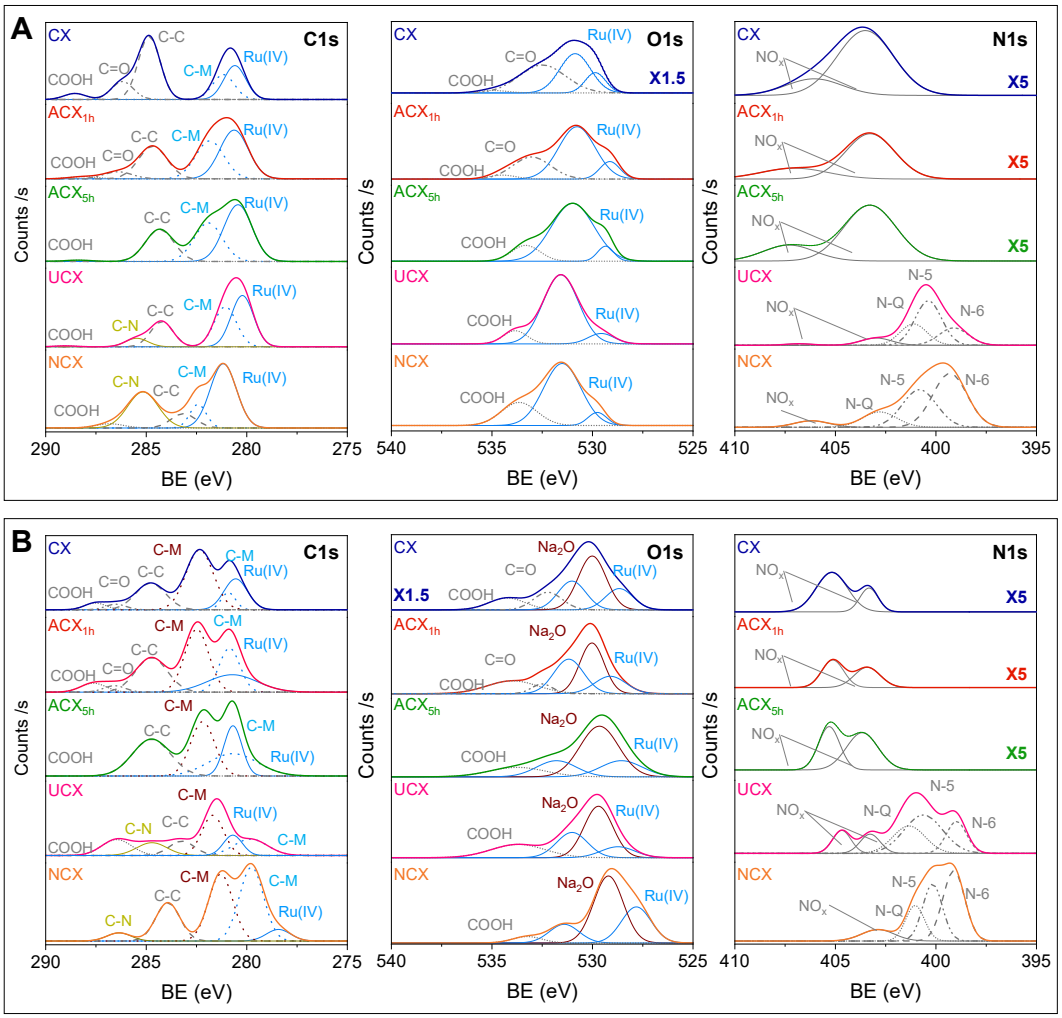

Figure 4.6. XPS spectra of C1s, O1s and N1s regions for the (A) un-promoted and (B) Na-promoted Ru-based catalysts here studied.

About the C1s region, four contributions were identified in the XPS spectra of all catalysts: dehydrogenated carbon species bound to a metal ion (*i.e.* around 281 eV), amorphous carbon (*i.e.* 284.6–284.9 eV), carbon in lactone groups (*i.e.* 286.2–286.7 eV), and carbon in carboxylic groups (*i.e.* 288.6–288.8 eV).

An additional contribution (*i.e.* around 283eV) was identified in the XPS spectra of the C1s region of all Na-promoted catalysts, which can be attributed to the formation of C-Na bonds [33,63,150,163]. Moreover, as a consequence of the N doping, both un-promoted and Na-promoted catalysts supported on UCX and NCX exhibited a further contribution in the C1s region, due to the C-N bond [63,150,162].

It can be seen that Ru-ACX_{5h}, Ru-UCX and Ru-NCX presented the two lowest contributions of amorphous carbon (*i.e.* 19%, 18%, and 19%, respectively), which is indicative of the higher order of their carbonaceous structure compared to the other catalyst supports studied in this work. This is in agreement with the results of the N_2 adsorption (BET) and Air-TGA experiments, which provided evidence of the lower surfaces areas and higher burning temperatures, thus higher crystallinity, of $ACX_{5h,}$ UCX and NCX, compared to CX and ACX_{1h}. Furthermore, as shown in the deconvolutions of the XPS spectra of C1s and O1s regions, Ru-ACX_{5h}, Ru-UCX and Ru-NCX did not present any contribution that could be ascribed to the presence of lactone groups on their surface. These results are in congruence with the TPD profiles shown in Figure 3.2, and the N_2-TGA data reported in Table 3.3, which suggested a scarce presence of lactone groups on their surfaces.

Likewise, monitoring the Ru3d XPS region, which overlaps with the C1s one, an additional peak, ascribed to the presence of the Ru oxide (*i.e.* Ru(IV)) on the catalysts' surface (*i.e.* about 280.7 eV) [160], is included in the deconvolution of the C1s XPS spectra of all catalysts herein studied.

As shown in Figure 4.6A and Figure 4.6B, the deconvoluted O1s region XPS spectra can be related to the following contributions [33,162]: Ru oxide (*i.e.* approx. 529 and 531 eV), oxygen in lactone groups (*i.e.* 532.7–533.0 eV) and oxygen in carboxylic groups (*i.e.* 533.8–534.4 eV). Moreover, an additional peak is included in the deconvolution of the O1s region of all Na-promoted Ru-based catalysts (see Figure 4.6B), which suggests the presence of Na oxide on the catalyst surface (*i.e.* about 530 eV) [161].

Similarly, for all N1s region XPS spectra, N components at high binding energy (*i.e.* around 402.4 and 406 eV) were identified, which can be attributed to NOx groups generated by the thermal decomposition of the Ru precursor $RuNO(NO_3)_3$ used in the synthesis of the catalyst [164]. As expected, the N1s region XPS spectra of all catalysts supported on N-doped carbon xerogels presented three additional N contributions, accounting for pyridinic nitrogen (*i.e.* 399.5–398.5 eV), pyrrolic nitrogen (*i.e.* 400.8–399.8 eV), and quaternary nitrogen (*i.e.* 403.0–401.0 eV) [33,63,150,160].

Finally, the deconvolutions of the XPS spectra of Na-promoted catalysts reported in Figure 4.6B, of the C1s, O1s and N1s regions, exhibited the same trend as their un-promoted counterparts. However, in the C1s and O1s regions, all Na-promoted catalysts showed an additional contribution corresponding to the presence of carbon-metal bonds and Na_2O [161], respectively, in agreement with the results of the TEM, STEM/EDS and TPR experiments wherein the presence of Na particles on the catalyst surface was hypothesised.

4.2 Performance of ruthenium-based catalysts during the ammonia decomposition reaction

4.2.1 Effect of the support

The performance of un-promoted catalysts during the NH_3 decomposition reaction is shown in Figure 4.7A. Two reaction runs were carried out not only to assess the reproducibility of the performance of the catalysts during the NH_3 decomposition reaction, but also to demonstrate the formation of Ru B5 sites after the first reaction run and study their effect on the catalysts performance during the second reaction run.

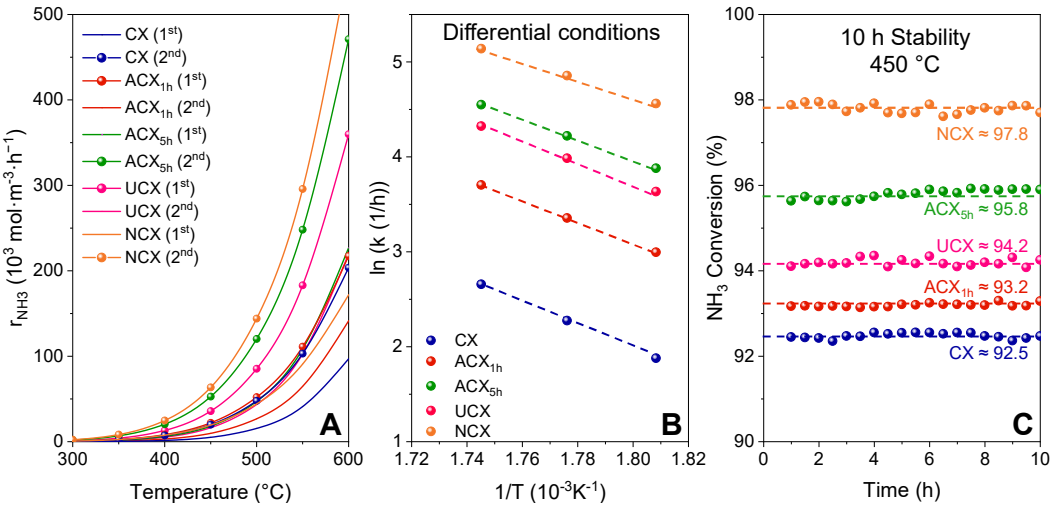

Figure 4.7. (A) NH_3 decomposition reaction rates of un-promoted Ru-based catalysts using a PBR, (B) Arrhenius' plot at differential conditions, (C) Long-term stability study of the PBR at 450°C.

The H_2 spillover effect observed on un-promoted Ru-based catalysts during TPR experiments could explain, in part, their higher catalytic activity compared with similar catalysts reported in the literature [33,34,48,90], as pointed out in Table 4.2. It has been reported that the H_2 spillover can enhance the catalytic activity during the NH_3 decomposition reaction since it affects the number of active sites available for the adsorption of NH_3 oncoming molecules. In particular, a large H_2 spillover effect encourages the migration of H_2 species over the surface, increasing the number of active sites available for the reaction [54,165].

It was observed that the CO_2 activation treatment had a positive effect on the performance of both Ru-ACX_{1h} and Ru-ACX_{5h}, which showed higher reaction rates than Ru-CX during the NH_3 decomposition reaction. This behaviour can be explained due to the higher crystallinity of ACX_{1h} and ACX_{5h} compared to CX. The higher activity of Ru-ACX_{5h} compared to both ACX_{1h} and CX can be justified by the lower amount of oxygen surface presented by ACX_{5h} compared to ACX_{1h} and CX. It has been stated by Aika et al. [52] and Zhong et al. [51] that oxygen surface groups withdraw electrons from Ru atoms, lowering the catalytic activity during the NH_3 decomposition reaction. Similar behaviour has been reported by Yin et al., which showed that the catalytic performance of Ru catalyst is support-dependent, observing that supports with strong basicity,

thus with less acidic oxygen functional groups, are beneficial for the NH_3 decomposition reaction [16].

Table 4.2. Comparison between the performances of the Ru-based catalysts studied in this work (TW) and those of the literature during the NH_3 decomposition reaction.

Catalyst	Ru (wt. %)	GHSV ($ml_{NH3} \cdot g_{cat}^{-1} \cdot h^{-1}$)	TOF ($mol_{NH3} \cdot mol_{Ru}^{-1} \cdot h^{-1}$)	Ref.
Ru-CX	1.5	2000	65[a]	TW
Ru-ACX$_{1h}$	1.5	2000	103[a]	TW
Ru-ACX$_{5h}$	1.5	2000	190[a]	TW
Ru-UCX	1.5	2000	163[a]	TW
Ru-NCX	1.5	2000	107[a]	TW
Ru/Na-CX	1.5	2000	169[a]	TW
Ru/Na-ACX$_{1h}$	1.5	2000	185[a]	TW
Ru/Na-ACX$_{5h}$	1.5	2000	326[a]	TW
Ru/Na-UCX	1.5	2000	236[a]	TW
Ru/Na-NCX	1.5	2000	470[a]	TW
Ru/AC	5.0	6000	19[b]	[48]
Ru/CNT	5.0	6000	45[b]	[48]
Ru/AC0	2.0	2000	75[b]	[34]
Ru/AC1	2.0	2000	75[b]	[34]
RuCNTs-0	2.0	2000	13[a]	[33]
RuCNTs-N	2.0	2000	17[a]	[33]
RuCNTs-1	2.0	2000	25[a]	[33]
RuCNTs-2	2.0	2000	128[a]	[33]
Ru/CNT	7.0	5200	11[c]	[90]
Ru/GCNT	7.0	5200	77[c]	[90]

[a] 1 atm, 350°C; [b] 1 atm, 400°C; [c] 1 atm, 327°C

Likewise, the N doping led to higher reaction rates of both Ru-UCX and Ru-NCX when compared with Ru-CX. The hypothesis formulated to justify this result is that the promoting effect of N atoms overcame the electron-withdrawing effect of the oxygen surface groups (*i.e.* carboxyl, anhydride, lactone), leading to a more basic catalyst support, thus to an improved catalytic activity. In this regard, it has been reported that N atoms in the carbon lattice enhance the local basicity and electron density of the support, which improve

the catalytic activity during the NH_3 decomposition reaction [33,54,64]. Figure 4.8 shows a schematic diagram of the electrons transfer mechanism in the presence of the basic and acidic surface functionalities.

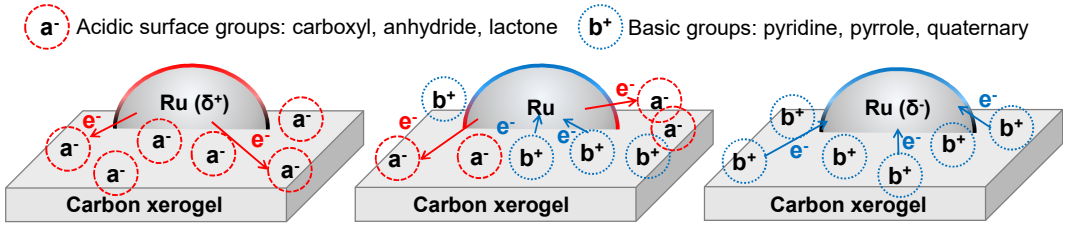

Figure 4.8. Schematic diagram of the electrons transfer mechanism in presence of both basic and acidic surface functionalities decorating the carbon xerogels surface.

In addition, it is well known that high electron transfer from electropositive elements to the active metal surface is needed to promote the NH_3 decomposition reaction rate-limiting step, *i.e.* the recombinative N_2 desorption [9]. Therefore, it was expected that the higher charge density of N-doped carbon xerogels compared to their non-doped counterparts would enhance the catalytic activity of metal particles performing in the NH_3 decomposition reaction.

As shown in Figure 4.7A, all un-promoted catalysts exhibited higher reaction rates during the second reaction run. This behaviour could be tentatively explained due to the formation of ruthenium B5 sites after the exposure of the catalysts at high temperature (*i.e.* 600°C). It is well established that the NH_3 decomposition reaction is structure sensitive, presenting a reaction rate dependent on the geometry of the metal particles [31–33]. Ru B5 sites consist of an ensemble of five edge atoms which encourage the NH_3 decomposition reaction by speeding up the N_2 desorption [31,32]. According to Van Hardeveld and Van Montfoort, the amount of B5 sites is maximised when the Ru metal particle size is between 2.5 and 5 nm [31]. This is in line with TEM results, which showed that the Ru particle after the first reaction run is higher than 2.5 nm in all the catalysts.

It is worth to mention that the performance of the catalysts during the NH_3 decomposition reaction could increase with the number of reaction runs, as a consequence of the increase in the number of B5 sites formed under the

reaction conditions. However, in this work, only two reaction experiments were carried out, which were sufficient to demonstrate the formation of B5 sites and their effect on the performance of the various catalysts presented here.

The reaction rate constant (k) for the NH_3 decomposition reaction of the un-promoted catalysts was calculated under differential conditions (*i.e.* gradient-less NH_3 concentration along the reactor), and the regressed parameters shown in the Arrhenius's plot in Figure 4.7B were used to determine the reaction rate constant at the operating conditions and the apparent activation energy (see Table 4.3). It is important to highlight that the relative increase in reaction rates after the first reaction run is not the same for the different catalysts. This result can be tentatively explained by the relative decrease in the metal dispersion for the different catalysts (see Table 4.1). In this respect, it is hypothesised that the greater the reduction in metal dispersion, the higher the formation of B5 sites, thus the relative increase in the reaction rate.

Table 4.3. Un-promoted Ru-based catalysts here studied: r_{NH3} at 450°C, E_a, and T_{10} before and after the first reaction run, and metal loading after the long-term stability test.

Catalyst	$r_{NH3,450°C}$ ($mol \cdot m^{-3} \cdot h^{-1}$)		E_a ($kJ \cdot mol^{-1}$)		T_{10} (°C)		Metal (wt.%)
	1st	*2nd*	*1st*	*2nd*	*1st*	*2nd*	*Ru*
Ru-CX	$5.2X10^3$	$2.0X10^4$	102.6	81.2	380	355	1.35
Ru-ACX$_{1h}$	$9.8X10^3$	$2.2X10^4$	93.3	80.0	360	345	1.37
Ru-ACX$_{5h}$	$1.8X10^4$	$5.3X10^4$	88.2	76.6	360	325	1.38
Ru-UCX	$1.6X10^4$	$3.7X10^4$	90.9	80.7	350	325	1.32
Ru-NCX	$2.0X10^4$	$6.4X10^4$	76.1	75.5	345	320	1.32

Finally, results in Figure 4.7C and Table 4.3 show that all catalysts here studied showed constant NH_3 conversions during the 100 h reaction experiment, proving their stability throughout the whole reaction experiment under the operating conditions adopted (*i.e.* 450°C, 1 atm). Furthermore, after the stability test, all catalysts here studied showed approximately 1.5 wt.% of Ru with a difference in metal loading within the measurement error (*i.e.* ± 3%), showing a high catalyst-preservability.

Key parameters characterising all catalysts here studied, such as i) reaction rate (*i.e.* r_{NH3}), ii) activation energy (*i.e.* Ea), iii) 10% conversion temperature (*i.e.* T_{10}), and iv) metal loading, are listed in Table 4.3.

4.2.2 Effect of the promoter

The performance of Na-promoted catalysts during the NH_3 decomposition reaction is shown in Figure 4.9A. It can be seen that the addition of Na had a positive effect on the performance of all the catalysts here studied, as also reflected in their reaction rate and activation energy, as listed in Table 4.4. Furthermore, in contrast with the behaviour of the un-promoted catalysts, the catalytic activity of Na-promoted catalysts did not improve after the first reaction run.

Table 4.4. Na-promoted Ru-based catalysts here studied: r_{NH3} at 450°C, E_a, and T_{10} before and after the first reaction run, and metal loading after the long-term stability test.

Catalyst	$r_{NH3,450°C}$ ($mol \cdot m^{-3} \cdot h^{-1}$)	E_a ($kJ \cdot mol^{-1}$)	T_{10} (°C)	**Metal** (wt.%)	
				Ru	*Na*
Ru/Na-CX	$5.0X10^4$	82.3	340	1.32	5.31
Ru/Na-ACX$_{1h}$	$5.3X10^4$	81.9	330	1.36	5.35
Ru/Na-ACX$_{5h}$	$7.8X10^4$	76.1	300	1.42	5.38
Ru/Na-UCX	$5.9X10^4$	82.0	305	1.34	5.33
Ru/Na-NCX	$8.7X10^4$	71.8	305	1.33	5.36

The enhanced catalytic activity of Na-promoted catalysts can be attributed to the electron donor effect of Na on Ru particles. In particular, it was found by Rarog et al., that Na modified the electrostatic potential around B5 sites, making them more active for the N_2 dissociation [88]. Moreover, the fact that the catalytic activity of Na-promoted catalysts did not change during the second reaction run suggests that Na_2O particles acted as a structural promoter, which avoided sintering and agglomeration of Ru particles, as also shown by TEM and STEM results previously discussed.

Like before, the reaction rate constant (k) for the NH_3 decomposition reaction at the operating conditions and the apparent activation energy were calculated

for each Na-promoted catalysts, using the data taken from the Arrhenius' plot in Figure 4.9B. Similarly to their un-promoted counterparts, all Na-promoted catalysts showed constant NH_3 conversions during the long-term stability test (see Figure 4.9C) and approximately 1.5 wt.% of Ru and 5.0 wt.% of Na with a difference in metal loading within the measurement error (*i.e.* ± 3%). These results indicate that the Na-promoted catalysts have high thermal stability under the operating conditions adopted (*i.e.* 450°C, 1 atm) and high catalyst-preservability.

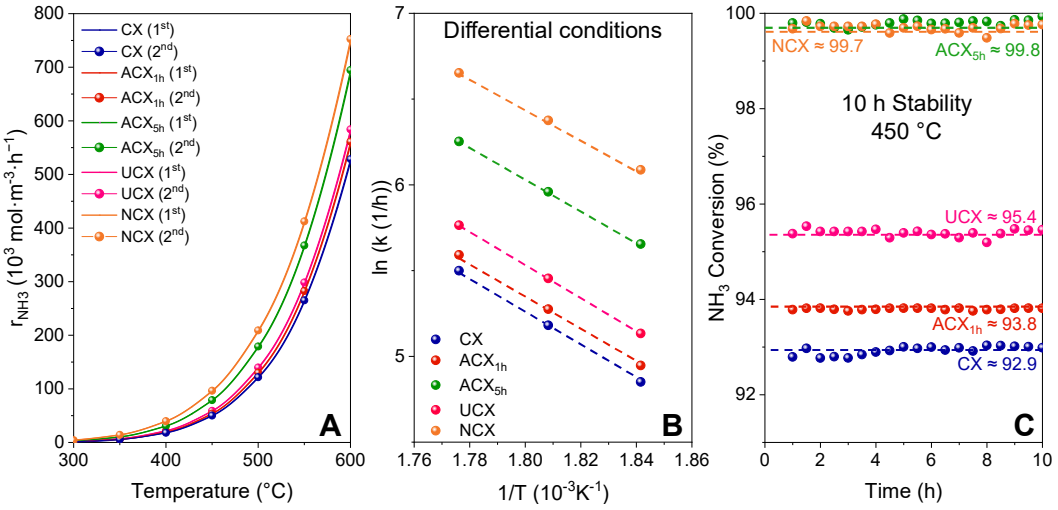

Figure 4.9. (A) NH_3 decomposition reaction rates of Na-promoted Ru-based catalysts using a PBR, (B) Arrhenius' plot at differential conditions, (C) Long-term stability study of the PBR at 450°C.

4.3 Conclusions

This study has proved that carbon xerogels are efficient catalyst supports for the NH_3 decomposition reaction and that the performance of Ru-based catalysts is affected by several factors, including textural and structural properties of the catalyst support, Ru particle size distribution and use of Na as catalyst promoter.

For instance, it has been found that despite the highest H_2 spillover contribution, Ru-CX exhibited the worst catalytic performance when compared to the other catalysts herein studied. This result can be justified due, in part, to the enhanced crystallinity of the CO_2 activated and N-doped carbon xerogels when compared to CX. Nevertheless, the improved catalytic performance of

both Ru-ACX_{5h}, Ru-UCX and Ru-NCX can be justified by the higher basicity and electron donor effect of ACX_{5h}, UCX and NCX compared to the other supports.

Likewise, higher NH_3 conversion levels were observed in catalysts with a Ru average particle size higher than 2.5 nm, confirming that the NH_3 decomposition reaction is sensitive to the structure, and suggesting the presence of B5 sites in the aforementioned catalysts.

Finally, the addition of Na had a remarkably positive effect on the performance of all catalysts studied during the NH_3 decomposition reaction. In this respect, metallic Na acted as an electronic promoter due to its electron donor effect on the Ru particles, whereas Na_2O acted as a structural promoter, preventing the sintering of Ru particles during the reaction.

Chapter 5 Results and Discussion Part III: Cobalt/molybdenum-based catalysts

This chapter includes a detailed description of the Co/Mo-based catalysts synthesised in this work, paying particular attention to the effect of the properties of the different carbon xerogels on the catalysts' performance during the NH_3 decomposition reaction.

5.1 Description of the cobalt/molybdenum-based catalysts

5.1.1 Transmission Electron Microscopy

TEM images of Co/Mo-based catalysts before and after the reaction experiments are shown in Figure 5.1. Note that the catalysts studied before the reaction were reduced before the TEM analysis. For all the catalysts, there was an even distribution of metal nanoparticles decorating the support surface. As shown by the histograms in Figure 5.1, the average metal particle size decreased by 15% and 20-35% after the CO_2 activation treatment and the N-doping, respectively. Likewise, it can be noted that the average metal particle size did not change upon the reaction experiment, suggesting that all catalysts are stable under reaction conditions.

As already discussed in Section 4.1.2, it is well known that both oxygen surface groups and N groups can act as anchoring sites for metal atoms, improving their dispersion throughout the support's surface [34,50,52,166,167]. Similarly to what has been evidenced by the TEM analysis of Ru-based catalysts, Co/Mo-CX exhibited a larger average particle size (*i.e.* 3.3 nm) compared to Co/Mo-ACX_{5h}, Co/Mo-UCX, and Co/Mo-NCX (*i.e.* 2.8 nm, 2.7 nm, and 2.2 nm respectively), even though CX presents the highest amount of oxygen surface groups.

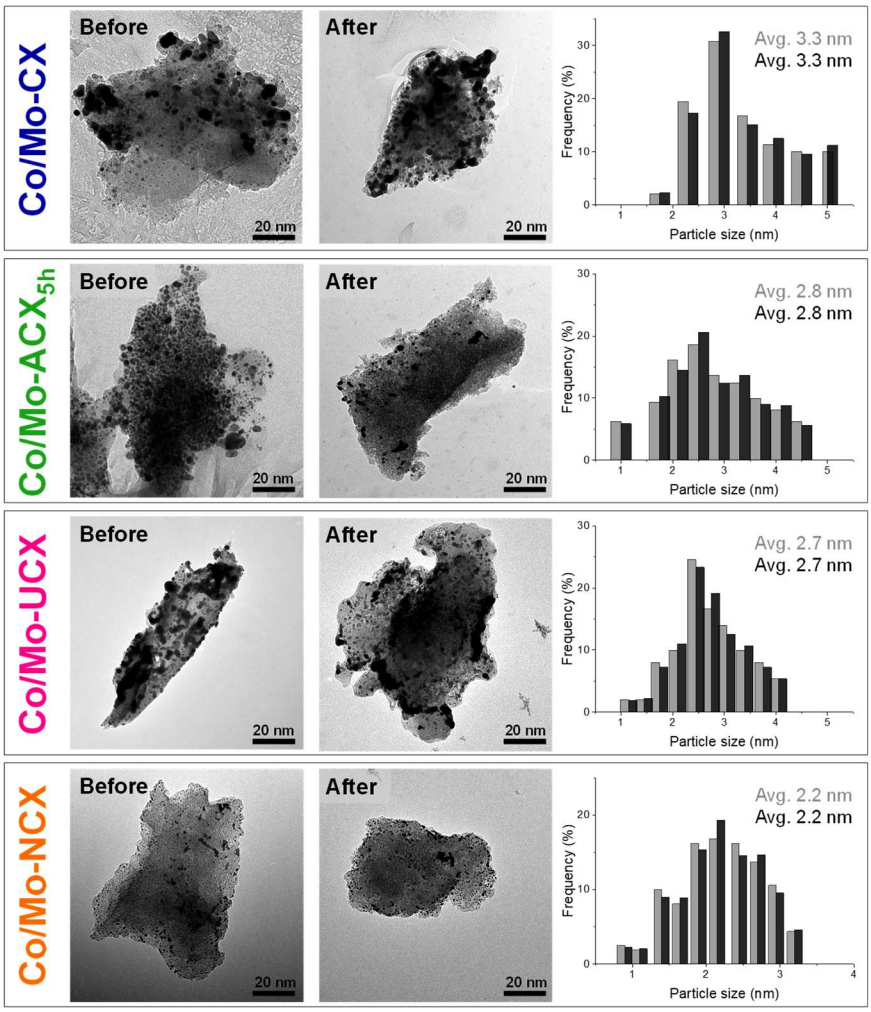

Figure 5.1. TEM images before reaction and particle size distributions of Co/Mo-based catalysts before and after the reaction.

For Co/Mo-UCX and Co/Mo-NCX, this result can be explained by a combination of two factors. On one hand, the large amount of acidic high temperature electron-withdrawing oxygen surface groups on CX weakens the interaction between the metal atoms and the support, thereby facilitating their mobility and agglomeration into larger particles [50]. This supports the fact that catalysts with the lowest average particle size, *i.e.* Co/Mo-UCX and Co/Mo-NCX, also showed the lowest amount of lactone groups. On the other hand, the presence of basic N functionalities in both UCX and NCX encourages the anchorage and dispersion of the metal active phase on the support surface due to the higher electronegativity of the support [158,166]. It is worth noticing that NCX showed a 10% lower average particle size than UCX, even though both catalyst supports were N-doped. This result, according to the XPS results

shown in Figure 3.3, can be justified by the different N speciation of NCX and UCX, which could affect the metal-support interaction [158,168,169].

Likewise, for Co/Mo-ACX_{5h}, the smaller average particle size compared to Co/Mo-CX (*i.e.* 2.8 nm and 3.3 nm, respectively), is indicative of stronger interactions of metal particles and support, thereby of an enhanced metal particles dispersion, as confirmed by the lower amount of lactone groups shown by ACX_{5h} compared to CX (*i.e.* by 96 %).

Finally, it was found that, after the reaction, the metal particle size distributions did not change significantly, and the average particle size remained the same for all the catalysts. These results suggested that no side reactions considerably affecting the amount of both the nitrogen functionalities and the oxygen groups (*i.e.* hydrogenation), thereby the metal particle size, occurred during our reaction experiments.

5.1.2 X-Ray Powder Diffraction

The open literature and the ICDD database Powder Diffraction Files (PDF-3) have been considered in the interpretation of the XRD diffractograms of reduced Co/Mo-based catalysts supported on carbon xerogels, which are shown in Figure 5.2 [46,133,134,144].

The main sharp diffraction peak centred at around 26° corresponds to the (002) basal plane diffraction along the graphitic structure [133,134,144]. Its sharpness and high intensity suggest that all carbon xerogels show a high crystallisation degree. In this respect, both the apparent crystallite size along the c-axis (L_c) and interlayer spacing along the c-axis (d_{002}) have been calculated by applying the Scherrer's equation to the (002) peak.

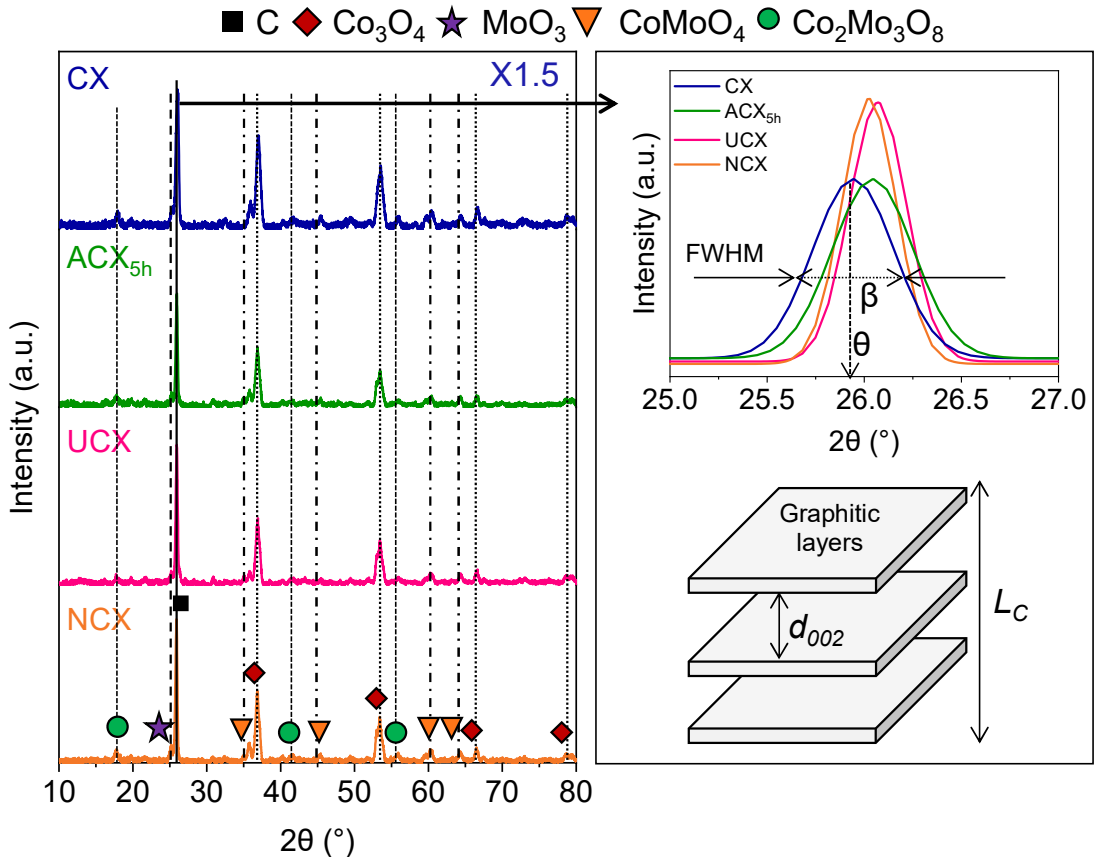

Figure 5.2. XRD diffractograms of Co/Mo-based catalysts.

As revealed by the data in Table 5.1, after N doping, this diffraction peak shifted to slightly higher angles and its intensity increased, evidencing a shrinkage in the carbon-to-carbon layer distance of both UCX and NCX. This behaviour suggests that the incorporation of N into the carbon xerogels lattice did not induce a significant increase in the structural order, as evidenced by the minimal changes in the crystallite size of CX after N doping (*i.e.* 11% bigger for UCX and 10% bigger for NCX). These results agree with the previous work of Kicínski et al., which studied the effect of the xerogel starting solutions and their carbonisation temperature on the crystallite size and the amount of stacked graphitic layers [133,144]. Similarly, Peikolainen et al. reported that the textural and structural properties of carbon xerogels directly affect the degree of order in their carbonaceous structure [134].

Table 5.1. Structural properties of CX, ACX_{5h}, UCX and NCX determined by XRD analysis.

Support	2θ (°)	L_C (Å)	d_{002} (Å)
CX	25.9	4.3	3.44
ACX_{5h}	26.0	4.3	3.42
UCX	26.1	4.7	3.41
NCX	26.0	4.8	3.42

The other major diffraction peaks identified using the ICDD database Powder Diffraction Files (PDF-3) evidenced that the active phase of the three Co/Mo-based catalysts is predominantly composed of a mixture of Co_3O_4, $CoMoO_4$ and $Co_2Mo_3O_8$. Despite the high reduction temperature (*i.e.* 600°C), no legible diffraction peaks associated with Co and Mo were observed, suggesting the re-oxidation of the catalysts when exposed to the atmosphere prior to the XRD analysis. Nevertheless, the absence of Co, Mo and CoO nanoparticles diffraction peaks, and the significantly lower intensities of Co_3O_4, $CoMoO_4$, $Co_2Mo_3O_8$ and MoO_3 diffraction peaks compared to the distinct diffraction peak associated with the carbon support, can be also attributed to a high metal particles dispersion, which is in agreement with the TEM results.

5.1.3 Temperature Programmed Reduction

The TPR profiles of Co/Mo-based bimetallic catalysts are shown in Figure 5.3. The open literature in combination with the Co-Mo-O_2 phase diagram provided in Figure 5.3A were used as references to interpret the TPR profiles of the catalysts studied in this work [37,46,170–173].

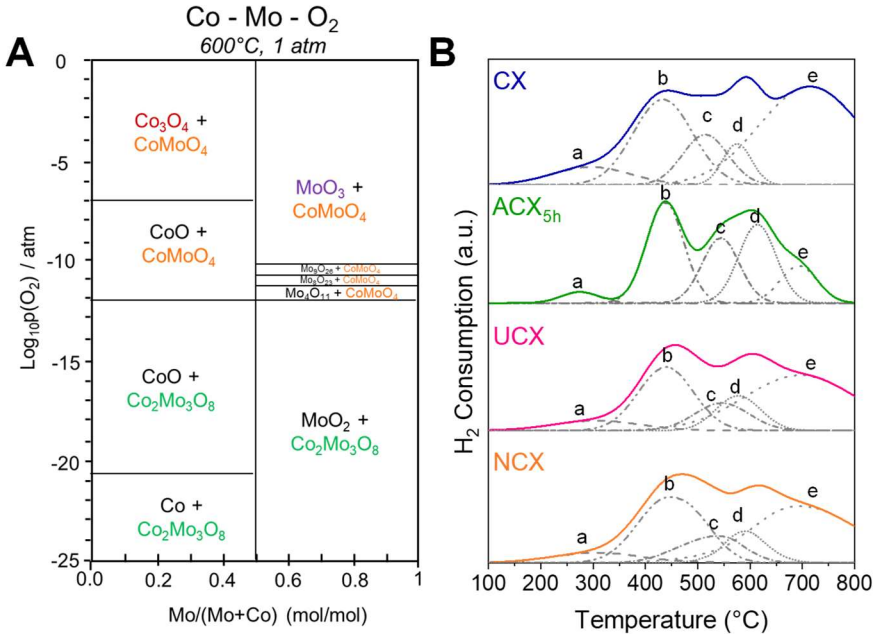

Figure 5.3. (A) Phase diagram of the Co-Mo-O2 (generated using FactSage thermochemical software) and (B) Temperature Programmed Reduction profiles of Co/Mo-based catalysts.

Overall, as shown in the schematic diagram in Figure 5.4, the TPR profiles showed five H_2 consumption peaks: a) reduction of Co_3O_4 to CoO (*i.e.* 280-300°C), b) reduction of CoO to Co (*i.e.* 430-450°C), c) reduction of $CoMoO_4$ to $Co_2Mo_3O_8$ (*i.e.* 520-540°C), d) partial gasification of the carbon support (*i.e.* 580-600°C), and e) reduction MoO_3 to MoO_2 (*i.e.* from 700°C onwards). The decrease in the intensity of peak d, corresponding to the partial gasification of the carbon support, after both the support's activation treatments and the N-doping, can be attributed to the higher thermal stability of ACX_{5h}, UCX and NCX compared to CX, as evidenced by Air-TGA analysis discussed in Section 3.1.5.

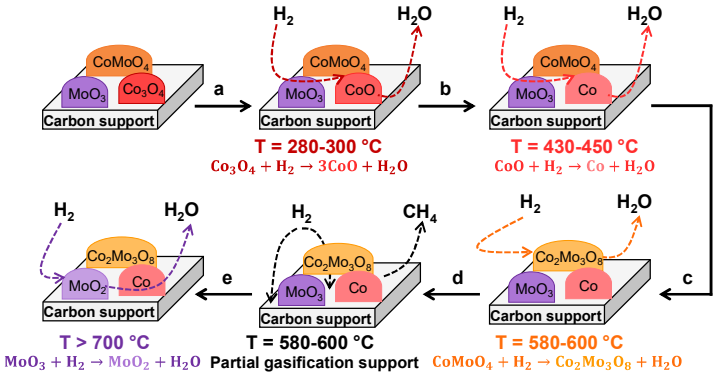

Figure 5.4. Schematic representation of the surface evolution of Co/Mo-based catalysts during the TPR experiments.

5.2 Performance of the cobalt/molybdenum-based catalysts during the ammonia decomposition reaction

The performance during the NH_3 decomposition reaction of the four Co/Mo-based catalysts studied in this work is shown in Figure 5.5A. It was observed that both Co/Mo-UCX and Co/Mo-NCX exhibited a higher catalytic activity than Co/Mo-CX during the reaction. This behaviour can be explained by a combination of two factors, including the lower amount of oxygen surface groups exhibited by both UCX and NCX, as well as the presence of N groups incorporated in their carbon lattice. In this respect, it has been widely acknowledged that acidic oxygen surface groups (*i.e.* carboxyl, anhydride, lactone) can withdraw electrons from metal atoms, negatively affecting the catalytic activity during the NH_3 decomposition reaction [51,52]. In contrast, the presence of N groups benefits the NH_3 decomposition reaction by enhancing the local basicity and electron density of the carbon support [33,79,158].

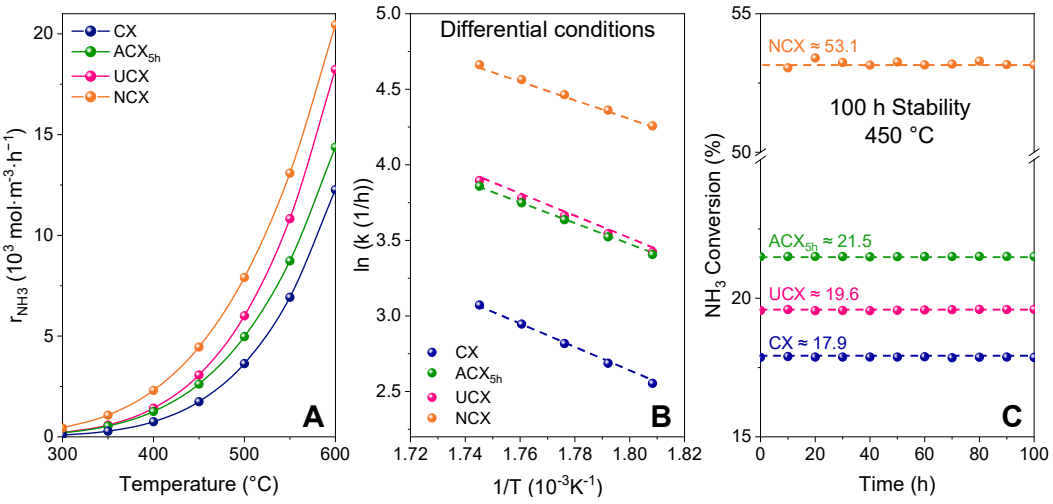

Figure 5.5. (A) NH_3 decomposition reaction rates of Co/Mo-based catalysts using a PBR, (B) Arrhenius' plot at differential conditions, (C) Long-term stability study of the PBR at 450°C.

In addition, it is well known that high electron transfer from electropositive elements to the active metal surface is needed to promote the NH_3 decomposition reaction rate-limiting step, *i.e.* the recombinative nitrogen desorption [35]. Therefore, it was expected that the higher charge density of N-doped carbon xerogels compared to their non-doped counterparts would

enhance the catalytic activity of metal particles performing in the NH_3 decomposition reaction.

The reaction rate constant (k) for the NH_3 decomposition reaction of the four Co/Mo-based catalysts was calculated under differential conditions (*i.e.* gradient-less NH_3 concentration along the reactor), and the regressed parameters shown in the Arrhenius' plot in Figure 5.5B were used to determine the reaction rate constant at the operating conditions and the apparent activation energy. As expected, it was found that Co/Mo-ACX_{5h}, Co/Mo-UCX, and Co/Mo-NCX exhibited higher reaction rate constants and lower apparent activation energy than Co/Mo-CX.

Finally, results in Figure 5.5C show that all catalysts here studied exhibited constant NH_3 conversions during the 100 h reaction experiment, proving their stability throughout the whole NH_3 decomposition reaction under the operating conditions adopted (*i.e.* 450°C, 1 atm). Key parameters characterising all Co/Mo-based catalysts here studied, such as i) metal particle size, ii) reaction rate, iii) activation energy, and iv) 10% conversion temperature, are listed in Table 5.2.

Table 5.2. Co/Mo-based catalysts here studied: metal average particle size (Dm), k at 450°C, Ea, and T_{10}.

Catalyst	Dm (nm)	$k_{450\,°C}$ ($h^{-1}\cdot g_{cat}^{-1}$)	E_a ($kJ\cdot mol^{-1}$)	T_{10} (°C)
Co/Mo-CX	3.3	$1.4X10^3$	68.2	430
Co/Mo-ACX_{5h}	2.8	$2.1X10^3$	59.6	430
Co/Mo-UCX	2.7	$2.5X10^3$	62.3	430
Co/Mo-NCX	2.2	$3.6X10^3$	53.3	365

It is noteworthy that, although both UCX and NCX are N-doped carbon xerogels, Co/Mo-NCX performed better in the NH_3 decomposition reaction. This behaviour, according to the XPS and TEM results previously discussed, can be ascribed, in part, to the higher N content of NCX compared to that of UCX. Moreover, this work evidenced an inverse relationship between the performance of the Co/Mo-based catalysts during the NH_3 decomposition

reaction and their average metal particle size since Co/Mo-NCX, which had the smallest metal average particle size, exhibited the highest catalytic activity. According to the TEM images in Section 3.1.5, this result can be explained due to the different degrees of dispersion of the metal particles over the carbon support. Contrary to the Ru-based catalysts, whose activity is maximised when the Ru metal particle size is between 2.5 nm and 5 nm [52], the optimal metal particle size for a Co/Mo-based catalyst is found to be around 2.2 nm.

5.3 Conclusions

This study has shown that the basicity and electrical conductivity of the support positively affect the catalytic activity of the Co/Mo-based catalysts during the NH_3 decomposition reaction. In this respect, Co/Mo-NCX was identified as the most suitable catalyst candidate for the NH_3 decomposition reaction, due to the improved basicity and electrical conductivity of NCX compared to CX, the lowest presence of oxygen groups on NCX surface, and promoting effects of the N atoms. Likewise, the metal particles size played an important role in influencing the catalysts' performance, being 2.2 nm the optimal particle size for Co/Mo-based catalysts for the NH_3 decomposition reaction.

Chapter 6 Results and Discussion Part IV: Design of hollow fibre reactors for on-board hydrogen production

This chapter provides a detailed description of the morphology of the asymmetric 4-channel α-Al_2O_3 hollow fibre (HF) used in this work to develop the hollow fibre reactors (HFRs). The analysis of the catalysts dispersion onto the HFs is reported in this chapter as well.

In addition, this chapter covers the effects of using a HFR on the catalysts' performance during the NH_3 decomposition reaction, and it includes a feasibility study that compares the traditional PBRs and the HFRs for on-board H_2 production via NH_3 decomposition.

6.1 Characterisation of the hollow fibre catalytic units

Based on the results collected during the NH_3 reaction experiments using the PBR (*i.e.* Chapter 4 and Chapter 5), among all Ru-based and Co/Mo-based catalysts here studied, Ru/Na-NCX and Co/Mo-NCX were identified as the most suitable catalyst candidates for deposition in the HF substrate. Before performing the reaction experiments, the HF substrates were characterised at different stages of the catalyst deposition procedure, *i.e.* after the carbon xerogel (*i.e.* NCX) and the metal catalyst deposition into the HF substrate.

Figure 6.1A provides representative SEM images of the HF unit before the carbon xerogel deposition, which show that the 4-channel asymmetric HF exhibits an asymmetric pore structure, as particularly noticeable in Figure 6.1A (ii-iii), called "sandwich" structure. The "sandwich" structure consists of a sponge-like porous region (teal, approximately 20% of the cross-section area) separating two finger-like regions (white, remaining 80% of the cross-section area). The sponge-like region in between finger-like regions consists of a porous α-Al_2O_3 layer, whereas the finger-like region is comprised of hundreds

of conical micro-channels (*i.e.* length 80-100 μm) perpendicularly distributed around the four lumens and the outer surface of the fibre.

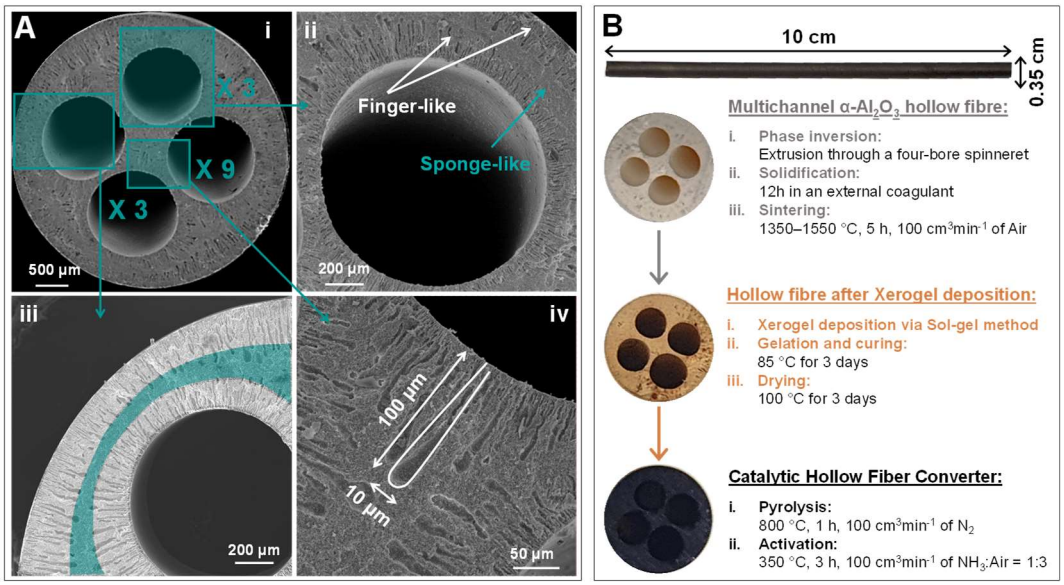

Figure 6.1. (A) SEM images of the HF substrate before NCX deposition, and (B) Cross-section of the HF at different stages of the NCX deposition process.

Furthermore, representative images of the HF unit, at different stages of the NCX deposition process are shown in Figure 6.1B. As can be seen, the HF showed homogeneous colouration after the sol-gel impregnation with the precursor xerogel solution, as well as after carbonisation and NH_3/Air activation treatments, proving the efficiency of this impregnation method.

SEM and EDS images presented in Figure 6.2A show the morphology and the elemental analysis of the HFRs, upon impregnation with Ru/Na-NCX and Co/Mo-NCX. In particular, the EDS surface mapping images show that the morphology of the HF substrate and the use of a precursor liquid solution results in the catalyst being uniformly dispersed over the support's surface. This is in contrast with the catalyst dispersion when traditional monoliths are employed as catalyst supports, being the accumulation of catalyst in the corners of the substrate the major limitations faced by traditional monoliths substrate [95].

Based on these results, and being the Ru/Na-NCX catalyst loading of 30 mg in a single HF 10 cm long and the Co/Mo-NCX catalyst loading of 150 mg in

the HF module, it can be assumed that the amount of catalyst per cm of hollow fibre (W_{HF}) is 3 mg.

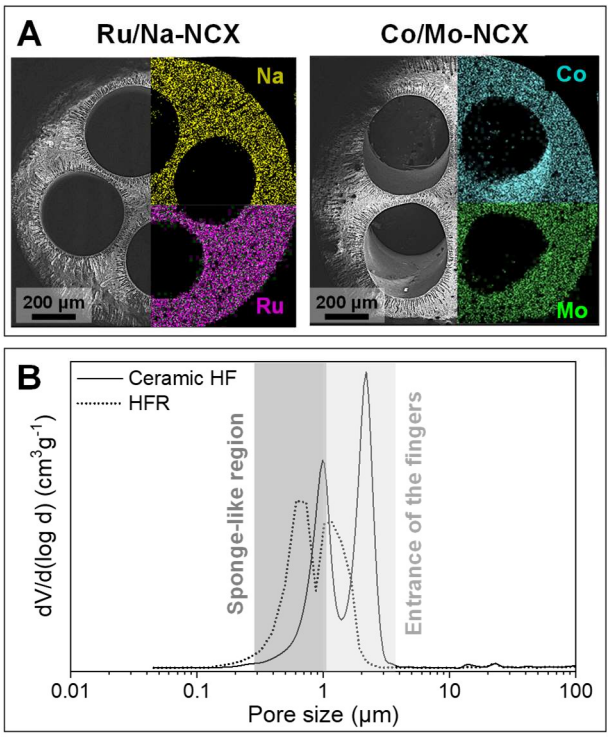

Figure 6.2. (A) Ru/Na-NCX and Co/Mo-NCX SEM images of the hollow fibre substrate and EDS surface mapping after the catalyst impregnation, (B) Hg porosimetry of the hollow fibre before and after the catalyst deposition.

In addition to the SEM/EDS analysis, the Hg pore size distributions of the α-Al_2O_3 HF provide further details of the asymmetric pore structure of the HF, before and after the catalyst deposition. As can be seen in Figure 6.2B, before the catalyst deposition, two different pore size distributions can be identified, corresponding to the sponge-like region (*i.e.* D_P = 1.0 µm) and the entrance of the fingers (*i.e.* D_P = 2.2 µm), respectively [118]. After the deposition, the pore size distribution in the sponge-like region and finger-like region decreased from 1.0 to 0.6 µm and from 2.2 to 1.2 µm, respectively. The reduction in the pore sizes of both regions can be explained due to the formation of a layer of catalyst around the pores and on the wall of the fingers of the HF substrate [70,71,115]. Given both the EDS and the Hg porosimetry results, it is expected that the thin catalyst layer has a thickness ranging between 0.4 and 1 µm.

6.2 Performance studies during the ammonia decomposition reaction using hollow fibre catalytic reactors

Based on the results collected during the reaction experiments using the PBR, Ru/Na-NCX and Co/Mo-NCX showed the best performance in the NH_3 decomposition reaction (see Chapter 4 and Chapter 5). In order to study the effect of using the HF as catalyst support on the catalysts' performance, the catalytic activity of both Ru/Na-NCX and Co/Mo-NCX during the NH_3 decomposition reaction was assessed using HFRs, and then compared to the one achieved using traditional PBRs. The beneficial effect of using the HFR on the catalytic activity of both catalysts can be seen in Figure 6.3A, which shows for instance that, at 450°C, the normalised NH_3 reaction rate in the HFR is 10 times higher than that in the PBR for Ru/Na-NCX, and 3.6 times higher for Co/Mo-NCX.

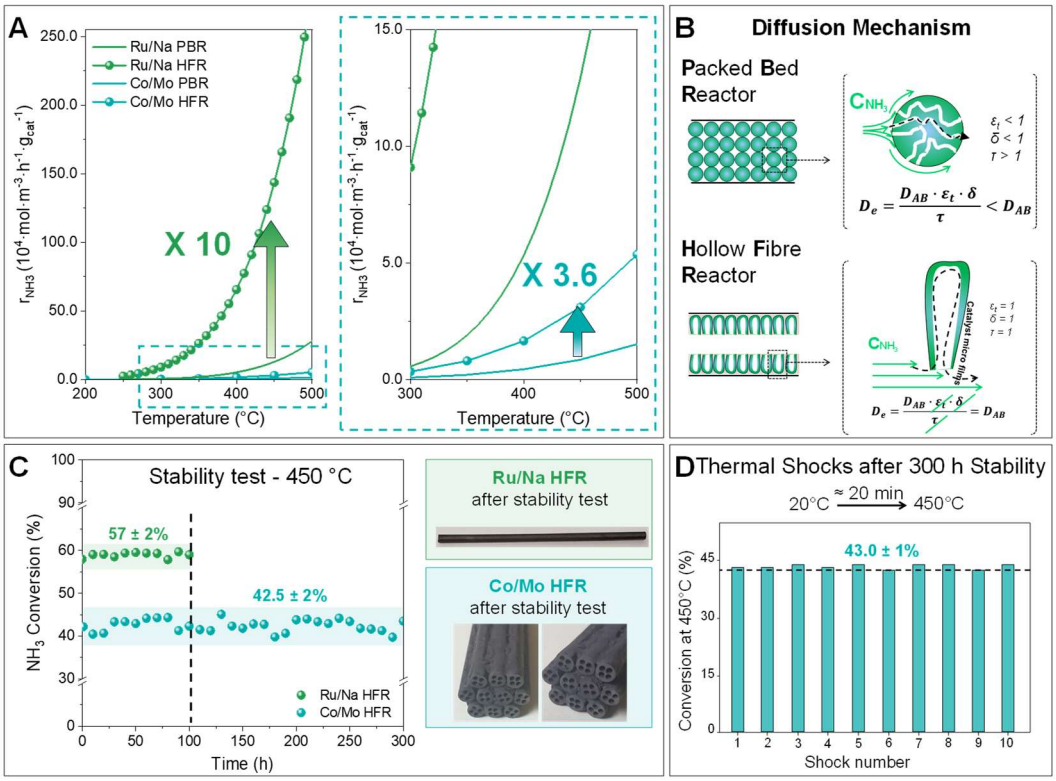

Figure 6.3. (A) NH_3 decomposition reaction rates in the PBR and HFR, (B) NH_3 diffusion mechanism in both the PBR and HFR, (C) Long-term stability study of Ru/Na-NCX and Co/Mo-NCX at 450°C, and (D) Co/Mo-NCX thermal shocks at 450°C after the stability study.

These results can be ascribed to the unique geometry of the HF substrate [9–11]. For instance, as can be seen from the diffusion mechanism of the reactant gases in a PBR and an HFR sketched and presented in Figure 6.3B, the granular structure of the catalyst in the PBR gives rise to unavoidable gas flow obstacles quantified as porosity, constriction factor and tortuosity. These obstacles slow down the internal diffusion of the reactants, giving an effective diffusion coefficient less than the bulk diffusion coefficient, and resulting in slower reaction kinetics (see Table 6.1) [140,141]. In contrast, using an HF as catalyst support bypasses diffusion limitations and overcomes problematic flow patterns such as fluid channelling, fluid recirculation and stagnant regions which are regularly observed in packed bed units [140,141], resulting in reaction kinetics that is as close to ideal kinetics as can be achieved [70,96]. This is because here the NH_3 diffuses into the micro-channels of the finger-like region of the HF, which are assumed to possess a porosity, tortuosity and constriction factor equal to one, giving an effective diffusion coefficient approximately equal to the bulk diffusion coefficient.

Table 6.1. Rate of reaction and reaction rate constant ($\boldsymbol{k}$) for the NH_3 decomposition reaction in the PBR and HFR at differential conditions (*) and at 450 °C.

	Ru/Na-NCX		***Co/Mo-NCX***	
$\boldsymbol{T}$ (°C)	$\boldsymbol{k_{PBR}}$ ($h^{-1}\cdot g_{cat}^{-1}$)	$\boldsymbol{k_{HFR}}$ ($h^{-1}\cdot g_{cat}^{-1}$)	$\boldsymbol{k_{PBR}}$ ($h^{-1}\cdot g_{cat}^{-1}$)	$\boldsymbol{k_{HFR}}$ ($h^{-1}\cdot g_{cat}^{-1}$)
280*	$8.0\text{x}10^2$	$1.4\text{x}10^4$	$2.4\text{x}10^2$	$5.6\text{x}10^2$
290*	$1.1\text{x}10^3$	$1.7\text{x}10^4$	$2.9\text{x}10^2$	$6.8\text{x}10^2$
300*	$1.4\text{x}10^3$	$2.2\text{x}10^4$	$3.5\text{x}10^2$	$8.2\text{x}10^2$
450	$3.1\text{X}10^4$	$3.5\text{x}10^5$	$2.1\text{X}10^3$	$7.6\text{X}10^3$

To assess the stability of both catalysts during the reaction experiments, a 100 h and 300 h reaction runs were carried out in an HFR using Ru/Na-NCX and Co/Mo-NCX, respectively. In this regard, as can be seen in Figure 6.3C, steady NH_3 conversions were achieved at 450°C in the HFR during the stability test using either Ru/Na-NCX or Co/Mo-NCX. In addition, for both catalysts, the HF presented a homogeneous colouration after the stability test, suggesting that this catalytic system is stable under operating conditions.

Furthermore, since developing a viable and competitive technology for on-board H_2 production is the main objective of this work, the effects of frequent start-up and shutdown cycles on the catalytic activity of Co/Mo-NCX and its peeling off resistance were studied in order to best mimic the operating conditions of a catalytic converter in a car. With this scope, 10 thermal shocks at 450°C were carried out. Similarly to the results obtained after the stability test, steady NH_3 conversion values were observed after each thermal shock (see Figure 6.3D), suggesting not only that this catalytic system is stable under operating conditions, but also that it has a high catalyst adherence, which prevents the catalyst from peeling off from the HF substrate. Finally, to corroborate these results, the Co/Mo-based HFR was weighed before the stability test and after the thermal shock tests, leading to a difference in weight within the measurement error (*i.e.* ± 0.01%).

Note that, the thermal shock experiments were performed only for Co/Mo-NCX as it was considered the most suitable candidate for this technology. In this respect, despite the lower performance of Co/Mo-NCX compared to Ru/Na-NCX under the same operating conditions, the significantly lower price of the Co/Mo system than Ru/Na system (*i.e.* 17.36 $\$\cdot g^{-1}$ for the Ru, 0.07 $\$\cdot g^{-1}$ for the Co and 0.04 $\$\cdot g^{-1}$ for the Mo [6]) allows working at higher catalysts loading to increase the catalyst performance during the NH_3 decomposition reaction without detriment to the overall costs of this technology. This makes Co/Mo-NCX a more attractive than Ru/Na-NCX solution for developing an on-board H_2 production systems.

6.3 Design of the hollow fibre catalytic reactors for on-board hydrogen production

The design feasibility study of both a PBR and HFR for on-board H_2 production via NH_3 decomposition presented in this work was carried out following the assumptions and constraints reported in Table 6.2, and using the parameters listed in the same table. In order to design both the PBR and HFR, several steps were followed.

Firstly, the reaction rate constant (k) during the NH_3 decomposition reaction for Ru/Na-NCX and Co/Mo-NCX in both reactors was calculated at the operating conditions (*i.e.* 450°C, 1 atm). Then, targeting a power demand of 100kW (*i.e.* 72 $m^3 \cdot h^{-1}$ (STP) of H_2 supply [174]), the flow rate of NH_3 required ($\dot{V_{NH_3}}$) to meet the target was calculated to be 48.2 $m^3 \cdot h^{-1}$ (STP).

Table 6.2. Assumptions, constraints and parameters for the design of both the PBR and HFR for on-board H_2 production.

Assumptions	**i.**	Isothermal catalytic process.
	ii.	The NH_3 decomposition reaction is irreversible and follows first order kinetics under operating conditions [28].
	iii.	Flow rate and fluid properties are uniform over any cross-section normal to the fluid motion.
	iv.	Negligible axial mixing due to either diffusion or convection
	v.	HF hexagonally packed into the module
Constraints	**i.**	Operating conditions: T = 450°C, P = 1 atm.
	ii.	NH_3 conversion at the equilibrium x_{NH_3} = 99.5% under operating conditions.
	iii.	On-board space constrains: L_{max} = 0.9 m, d_{max} = 0.3 m [5], and V_{max}= 63 L.
Parameters	**i.**	Density of the bed ρ_b= 300 $kg \cdot m^{-3}$.
	ii.	Bed porosity ε_b = 0.3.
	iii.	Area of one HF channels A_c = 3x10^{-6} m^2.
	iv.	Area of both the sponge-like and finger-like regions of a single HF unit A = 6.1x10^{-6} m^2.
	v.	HF porosity ε_{HF} = 0.43 [118].
	vi.	NH_3 density ρ_f = 0.3 $kg \cdot m^{-3}$ (450°C, 1 atm).
	vii.	Dynamic viscosity of NH_3 μ_f = 2.5x10^{-5} Pa·s (450°C, 1 atm).
	viii.	Effective diffusion D_e = 6.1x10^{-6} $m^2 s^{-1}$ (450°C, 1 atm).

Successively, to estimate the catalyst loading needed, to achieve an NH_3 conversion x_{NH_3}= 99.5% under the operating conditions adopted, thereby the required volume of both the PBR and HFR, the following NH_3 mass balance over a differential element of catalyst loading (*i.e.* dW) was used:

$$Input - Output - Consumption + Production = Accumulation \quad 6.1$$

Where:

- $Input - Output$ is the difference between the molar flowrate of NH_3 at the inlet and at the outlet of the differential element (*i.e.* $-d\dot{F}_{NH_3}$).
- $Consumption$ is the NH_3 disappearance due to the reaction (*i.e.* $r_{NH_3}dW$).
- $Production$ is equal to zero because we are assuming that, at the operation conditions, the reaction is irreversible.
- $Accumulation$ is equal to zero because both reactors are at steady state.

Substituting each of these terms in the Eq. 6.1 the NH_3 mass balance over a differential element of catalyst loading was rewritten as below:

$$-d\dot{F}_{NH_3} - r_{NH_3}dW = 0 \quad 6.2$$

Upon integration of the Eq. 6.2, it was obtained that the design equation for both PBR and HFR can be written as:

$$W = -\rho_b \frac{\dot{V_{NH_3}}}{k} ln\left(1 - x_{NH_3}\right) \quad 6.3$$

Finally, as last step, the pressure drop through the PBR and HFR was estimated using the Ergun equation (Eq. 6.4) and the Hagen–Poiseuille equation (Eq. 6.5), respectively, and the mass transfer limitations for both reactors were estimated by using the definition of the Thiele modulus ϕ^2 (Eq. 6.6) reported below:

$$\frac{-\Delta P}{L_{PBR}} = 150\frac{\mu_f U(1-\varepsilon_b)^2}{d_p^2 \varepsilon_b^3} + 1.75\frac{\rho_f U^2(1-\varepsilon_b)}{\varepsilon_b^3} \quad 6.4$$

$$\frac{\Delta P}{L_{HFC}} = 8\frac{\pi\mu_f \dot{V}_{NH_3}}{A^2} \quad 6.5$$

$$\phi^2 = \frac{NH_3\ reaction\ rate}{NH_3\ diffusion\ rate} = \frac{kC_{NH_3}^{n_r-1}r_p^2}{D_e} \quad 6.6$$

Where d_p and r_p the diameter and the radius of the catalyst pellet, respectively.

As it can be seen from the data reported in Table 6.3, unsurprisingly for both catalysts, the use of the HFR to perform the NH_3 decomposition reaction resulted in improved reaction kinetics (*i.e.* more than 3.5-fold) and minimised mass transfer limitations (*i.e.* around 95% lower) compared to the use of a traditional PBR. As already discussed in the previous section, this phenomenon can be justified by the unique geometry of the HF substrate, which allows overcoming typical problems associated with the use of PBRs [9–11]. In addition to that, both HFRs occupy a lower volume than the corresponding PBRs (*i.e.* more than 65% smaller) and lead to lower ΔP.

Table 6.3. Comparison between the PBR and HFR for on-board H_2 production at 450°C using Ru/Na-NCX and Co/Mo-NCX.

	PBR		**HFR**	
	Ru/Na	Co/Mo	Ru/Na	Co/Mo
$\boldsymbol{k}$ ($h^{-1} \cdot g_{cat}^{-1}$)	$3.1X10^4$	$2.1X10^3$	$3.5X10^5$	$7.6X10^3$
$\boldsymbol{d_p}$ (mm)	1.1	0.8	0.1	0.1
$\boldsymbol{\phi^2}$	0.40	0.4	<<0.01	<<0.01
$\boldsymbol{V}$ (L)	62.7	350.0	3.4	79.3
$\boldsymbol{W_{cat}}$ (kg)	8.1	71.1	1.0	23.8
L (m)	0.9	1.6	0.9	1.6
d (m)	0.3	0.5	-	-
$\mathbf{N_{HF}}$ (-)	-	-	315	4030
$\Delta \boldsymbol{P}$ (bar)	1.1	0.9	$5.1X10^{-3}$	$2.2X10^{-3}$

Similarly, this design study showed that the Ru/Na-based HFR offers the advantages of requiring smaller volume (*i.e.* by around 95%), thus fewer HF units (*i.e.* around 13 times less), and lower catalyst loading (*i.e.* by around 95%) than the Co/Mo-based one. In addition to that, it is worthy to notice that despite leading to a negligible ΔP, the so-designed Co/Mo-based HFR is unfeasible for on-board H_2 production since it does not meet the on-board space constraints (*i.e.* $V>V_{max}$ = 63 L [5]). Likewise, the remarkably high number of HF units required to develop the so-designed Co/Mo-based HFR (*i.e.* N_{HF} = 4030) would make the HF module assembly difficult. If it is assumed that the HF used for the two HFRs is of the same length (*i.e.* L_{HFR} = 0.9m), the

number of units required by the Co/Mo-based one would be even greater, *i.e.* 7225 units.

Note that, in order to minimise the ΔP through the reactor, avoiding mass transfer limitations (*i.e.* $\phi^2 \leq 0.4$), dense pellets thinly coated with a catalyst layer were considered when designing the PBRs. In this respect, as can be seen in Figure 6.4, for the design study at 450°C, the pellet size of Ru/Na-NCX has been optimised without exceeding the on-board space limits, obtaining d_p= 1.1 mm and V_{PBR} = 62.7L. On the contrary, to minimise the ΔP through the Co/Mo-based PBR a minimum pellet size of 0.8 mm, thereby a reactor volume V_{PBR} = 350 L, is required, making it unfeasible to fit the reactor on-board.

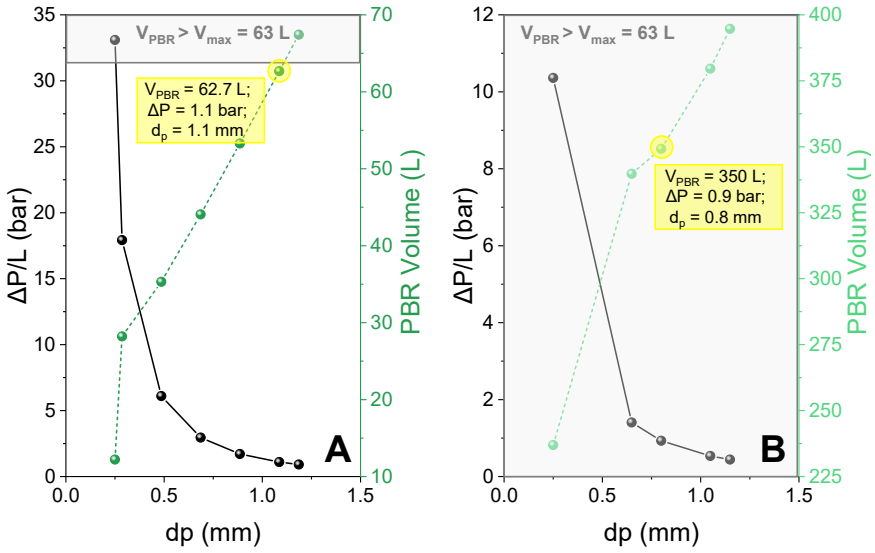

Figure 6.4. Effect of the d_p on the ΔP through the (A) Ru/Na-based and the (B) Co/Mo-based PBRs and their volume.

As mentioned in the introduction of this thesis, the large surface area/volume ratio typical of the HF substrates (*i.e.* > 1000 $m^2 \cdot m^{-3}$ [118]) allows increasing the loading of Co/Mo-NCX to the extent that the catalytic performance of Ru/Na-NCX is matched without significant detriment to mass transfer limitations and costs. Based on that, the effect of the catalyst loading (*i.e.* Co/Mo wt.%) on the reactor volume was investigated, assuming that the performance changes linearly with it. With this scope, the Co/Mo wt.% used were 1.5 wt.%, 3.0 wt.%, and 6.0 wt.%. The effect of changing the operating

temperature (*i.e.* 450°C and 500°C) on the reactor volume was also studied for the different catalyst loadings, in order to find the best combination of Co/Mo wt.%, operating temperature and reactor volume (see Figure 6.5).

Like before, the reactor volume and the catalyst loading required were estimated using the NH_3 mass balance in Eq. 6.3. Similarly, the ΔP through the different reactors was estimated using either the Ergun equation (Eq. 6.4) or the Hagen–Poiseuille equation (Eq. 6.5), and the mass transfer limitations were estimated by using the definition of the Thiele modulus ϕ^2 (Eq. 6.6).

As can be seen in Figure 6.5A, only two PBRs have a smaller volume than the maximum volume allowed by the on-board space constraints. Note that, for each PBR, the pellet size of Co/Mo-NCX catalysts has been optimised in order to minimise the ΔP through the reactors and avoid internal mass transfer limitations (*i.e.* $\phi^2 \leq 0.4$). As shown in Figure 6.5B, the use of 6.0 wt.% metal loading requires a PBR of 62.1 L and 17.8 kg of catalyst at 450°C, and a PBR of 63.0 L and 11.2 kg at 500°C. However, despite both reactors would occupy a similar volume, the optimal Co/Mo-based PBR designed is the one working at 500°C using 6.0 wt.% Co/Mo, since working at 450°C leads to a significantly higher ΔP through the reactor (*i.e.* ~4 times bigger) and requires a higher catalyst loading compared (*i.e.* ~1.5 times more) than working at 500°C (see Figure 6.5D).

On the other hand, as per Figure 6.5C, five HFRs meet the on-board space constraints. Note that for all design studies, the L_{HFR} has been set equal to the length of the optimal Co/Mo-based PBR, *i.e.* L_{PBR} = 0.9 m. To ease the assembly of single HF units into a larger module, the HFR requiring the lowest N_{HF} has been identified as the most suitable for on-board applications (see Figure 6.5B). This choice took also into account that the ΔP through the HFRs, and so their efficiency, did not change significantly with the operating temperature and/or the catalyst loading. Hence, as shown in Figure 6.5D, the optimal Co/Mo-based HFR designed is the one working at 500°C and with 6.0 wt.% Co/Mo.

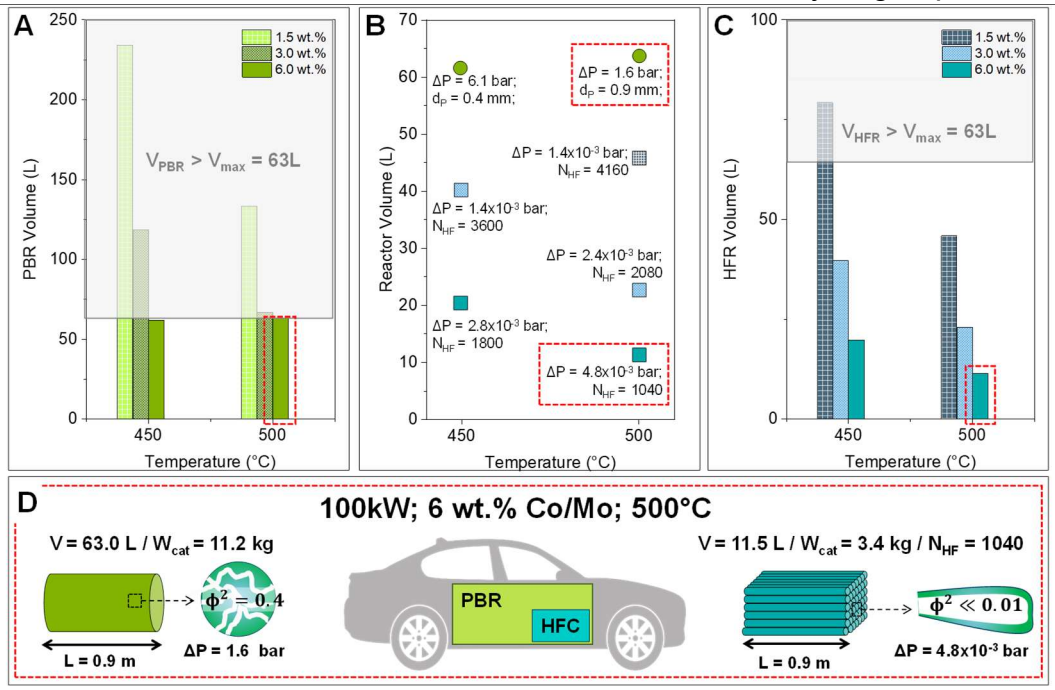

Figure 6.5. (A-C) Effect of the temperature and the catalyst metal loading on the volume of both the PBR and HFR, (D) Optimal design of a PBR and HFR for a car with a power demand of 100 kW (i.e. 72 $m^3 \cdot h^{-1}$(STP) of H_2 supply).

As expected, from the direct comparison between the optimally designed Co/Mo-based PBR and HFR in Figure 6.5D, the latter is more advantageous than the former in terms of cost (*i.e.* 65% less catalyst), space occupied (*i.e.* 80% smaller), and efficiency (*i.e.* >95% less pressure drop). Similarly to before, the use of a traditional PBR for on-board applications turned out to be unfeasible due to its high ΔP.

It is important to emphasise that this study demonstrates the superiority of HFRs not only over conventional PBRs, but also over the more innovative microreactors (see Table 6.4). In this respect, as mentioned before in the introduction of this thesis, over the past years, different reactors for NH_3 decomposition have been designed as an alternative to PBRs with the aim of reducing the reactor size and improving the kinetic of the NH_3 decomposition reaction [22,23,93,94].

To cite an instance, Wang et al. developed a monolithic-base “miniature” NH_3 cracker (*i.e.* overall weight of ≈195 g and volume of ≈50 cm^3) able to produce roughly 158 W equivalents of H_2 via NH_3 decomposition at high temperature

[22]. Despite the "miniature" NH_3 cracker presents a lower ΔP compared to the traditional PBRs, its relatively large size (*i.e.* ~30 L to produce ~100 kW equivalents of H_2), and high operation temperature (*i.e.* conversion of >99.9% at 600°C), make it disadvantageous for on-board H_2 production compared to the HFRs proposed in this work. Furthermore, the accumulation of unused catalyst in the corners of channels is an unavoidable issue in monolithic-base reactor technology, such as the "miniature" NH_3 cracker, which increases their cost and decreases their efficiency, thereby limiting their use [96].

Table 6.4. Comparison between the PBR and HFR herein designed for on-board H_2 production and the reactors reported in the open literature.

	Ru/Na-HFR	**Co/Mo-HFR**	**"Miniature" cracker** [22]	**Microchannel reactor** [94]
$\boldsymbol{V}$ (L)	3.4	11.5	30.0	0.6
$\boldsymbol{W_{cat}}$ (kg)	1.0	3.4	0.8	~ 5.2
$\mathbf{N_{HF}}$ (-)	315	1040	-	-
$\boldsymbol{\phi^2}$	<<1	<<1	-	-
$\Delta \boldsymbol{P}$ (bar·m^{-1})	5.7X10^{-3}	5.3X10^{-3}	0.39	0.45
Met. loading (wt.%)	Ru/Na – 6.5	Co/Mo - 6.0	Ce/Ni – 20	Ru – 8.5
Operating T (°C)	450°C	500°C	600°C	600°C

Likewise, Chiuta et al. developed a super-compact NH_3 -fuelled microchannel reactor unit (*i.e.* a plate consisting of 80 microchannels) wash-coated with a commercial 8.5 wt% Ru-based catalyst for H_2 production [94]. Like the HFR, this type of microchannel reactor presents the advantage of an easier power scale-up via integration of units [23,94]. However, despite its exceptionally small size (*i.e.* <1 L to produce ~100 kW equivalents of H_2), its high operation temperature (*i.e.* conversion of >99.8% at 600°C), high ΔP (*i.e.* 0.45 bar·m^{-1}), and the large noble metal content (*i.e.* 8.5 wt% Ru is far from the current low loading noble metal target) challenge its use for on-board applications.

6.4 Conclusions

This work provided critical information to advance the uptake of H_2 as an alternative to traditional carbon-based automotive fuels, thus contributing

towards the decarbonisation of our energy system during the transition towards 100% renewable energy. The HFRs for NH_3 decomposition open the door for a new line of worthwhile catalytic converters, which will be a sound alternative to traditional catalytic PBRs.

In this respect, it was found that the HFRs offered noteworthy advantages compared to the traditional PBRs, in terms of cost (*i.e.* 70-80% less catalyst), space occupied (*i.e.* 80-95% smaller), and efficiency (*i.e.* lower ΔP and mass transfer limitations). Likewise, all the HFRs showed high thermal stability and catalyst adherence, as demonstrated by the 100 h and 300 h reaction experiments. Furthermore, the tailorable nature of the HFR technology and the easy power scale-up via integration of units facilitates its adoption for automotive applications, without compromising the design flexibility of vehicles. In addition to that, based on the feasibility studies herein carried out, it can be said that the Co/Mo-based HFR represents the most convenient option for on-board H_2 production due to the lower cost of the Co/Mo-NCX compared to Ru/Na-NCX (*i.e.* 17.36 $\$\cdot g^{-1}$ for the Ru, 0.07 $\$\cdot g^{-1}$ for the Co and 0.04 $\$\cdot g^{-1}$ for the Mo [6]). Finally, HFRs have been proved to be favourable compared to the latest micro-reactors developed for the NH_3 decomposition, allowing to work at lower temperatures, ensuring a homogeneous catalyst distribution on the supports, and resulting in lower pressure drop.

Chapter 7 Results and Discussion Part V: Design of a hollow fibre membrane reactor for on-board hydrogen production

This chapter provides a description of the morphology of the palladium membrane synthesised in this work to develop the hollow fibre membrane reactor (MHFR) and a kinetic study of the palladium deposition rate.

In addition, this chapter shows the advantages of using the MHFR over a traditional PBR the catalysts' performance during the NH_3 decomposition reaction, and it includes a feasibility study that compares the traditional PBR, the HFR and the MHFR for on-board H_2 production via NH_3 decomposition.

7.1 Characterisation of the Pd membrane

Representative images of the HF unit after the deposition of the glaze are shown in Figure 7.1A. Similarly, pictures of the glazed HF after each sensitisation/activation loop and corresponding SEM images of their outer surface are shown in Figure 7.1B.

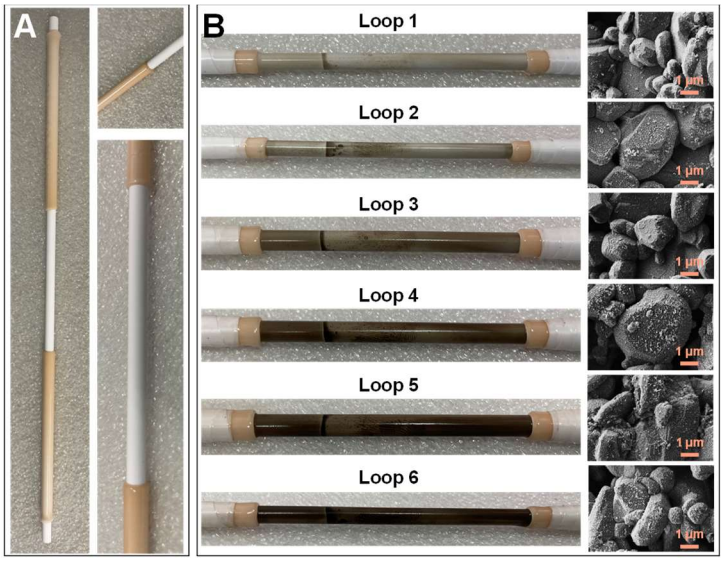

Figure 7.1. Images of the HF unit (A) after the glaze deposition and (B) after each sensitisation/activation loop with corresponding SEM images of their outer surface.

As can be seen, the colour of the outer surface of the HF turned darker after each sensitisation/activation loop as a consequence of the higher amount of Pd seeds deposited onto its surface [136]. This is corroborated by the SEM images in Figure 7.1B which clearly show that the more the number of sensitisation/activation loops are, the higher the number of Pd seeds deposited on the HF substrate.

Likewise, pictures of the HF unit after the two electroless plating (ELP) cycles shown in Figure 7.2A indicated that a homogeneous layer of Pd was successfully deposited on the HF outer surface after each ELP. Similarly, the SEM images of the cross section of the deposited Pd membrane in Figure 7.2B, confirmed the homogeneity of the deposited Pd layer and allowed to estimate its thickness, found to be ~ 11-13 μm.

According to Mardilovich et al, this thickness ensures the absence of leaks on the surface of the Pd membrane, being at least three times bigger than the maximum pore diameter of the HF substrate (*i.e.* ~1.0 μm) [114]. In this regard, before assessing the performance of the MHFR during the NH_3 decomposition reaction, the suitability for H_2 separation of the obtained Pd membrane was tested under Ar atmosphere to ensure the absence of leaks.

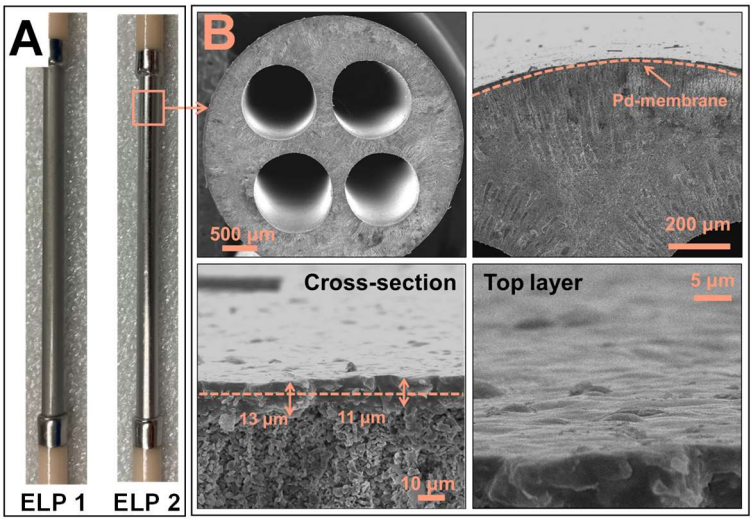

Figure 7.2. (A) Images of the hollow fibre unit after the first and the second ELP (B) SEM images of the deposited Pd-membrane cross section after the second ELP.

However, it can be seen that the membrane obtained in this work is thicker than that reported in the literature (*i.e.* 1 μm - 4.6 μm) for Pd membranes

obtained following the same experimental procedure and using similar supports (*i.e.* ceramic support with comparable porosity) [175,176]. In order to explain these results, the Pd deposition rate under the experimental conditions adopted in this work was determined by carrying out a plating kinetic study, which consisted in estimating the amount of Pd deposited at different ELP times. With this scope, a constant plating area (*i.e.* 6.6 cm^2), ELP solution volume (*i.e.* 36.3 cm^3), and ELP temperature (*i.e.* ~64°C) were maintained during the experiments.

As can be seen in Figure 7.3A, the amount of Pd deposited on the outer surface of the HF substrate increased linearly with the ELP time (*i.e.* deposition rate = 3.7 $\mu m \cdot h^{-1}$). Based on that, the minimum membrane thickness required to avoid leaks on the surface of the Pd membrane (*i.e.* ~3.0 μm) can be obtained after approximately 50 minutes of ELP. Nevertheless, in this work, two 90-minute ELP cycles were performed in order to make sure that a uniform, defect-free membrane, and thermal resistant under the adopted operating conditions, was deposited on the HF substrate. Assuming that the Pd deposition rate does not change after the first ELP cycle, predicted (*i.e.* Figure 7.3A correlation) and experimental Pd membrane thickness (*i.e.* SEM images in Figure 7.2B) show good agreement, being ~11.2 μm and ~ 11-13 μm, respectively, as well as it is thicker than the theoretical minimum thickness (*i.e.* ~ 3 μm).

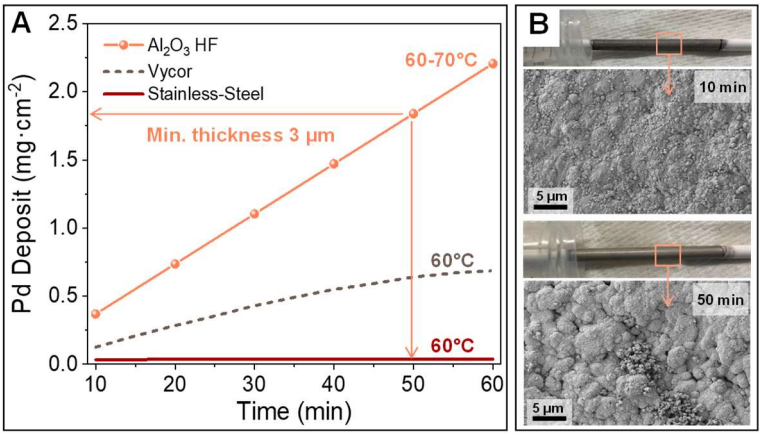

Figure 7.3. (A) Pd deposition rate for different Pd membrane supports and (B) Representative photo and corresponding SEM image of the Pd-layer deposited on the HF outer surface after 10 minutes and 50 minutes of ELP.

A similar linear relationship between ELP time and Pd deposition rate was obtained Mardilovich et al., which found that the Pd deposition rate on a stainless steel support, at 60°C and using an ELP solution volume to plating surface area equal of 3.5, is constant with the time (*i.e.* 1.83 $\mu m \cdot h^{-1}$) for approximately 1 h before depletion of Pd seeds [177]. Similarly, Yeung et al. found that the Pd deposition rate on Vycor at 60°C is maximised in the first 20 minutes of plating (*i.e.* 1.5 $\mu m \cdot h^{-1}$) before rapidly decreasing with the plating time when an ELP solution volume to plating surface area of 2.85 is used [178]. The absence of an induction period in the Pd rate deposition profiles shown in Figure 7.3A can be explained by the activation of the membrane support in the case of the HF and the Vycor, which is a process known to effectively reduce or eliminate the induction time for nucleation of Pd seeds during the deposition of the Pd layer on the support via ELP, or by the conductive nature of the stainless steel [178,179].

Despite the linear trend of the Pd deposition rates reported in Figure 7.3A, the Pd rate of deposition obtained in this work is at least twice the ones reported in other works. These results can be explained due to different factors. For instance, it is well known that the membrane support can affect the Pd deposition kinetic and the membrane thickness, as also confirmed by the different Pd deposition rates observed by Mardilovich et al. and Yeung et al., which used two different membrane supports but similar experimental conditions; therefore it is reasonable to assume that the use of an Al_2O_3 HF as membrane support influenced the Pd rate of deposition.

Likewise, although the Pd to support surface area ratio used in this work for the ELP and those reported in the literature differ [177,178,180], the concentration of Pd in the ELP solutions is the same, suggesting that the significant discrepancy between the rate of Pd deposition here reported and those reported elsewhere can be ascribed to the temperature at which the ELP was carried out. In this respect, as mentioned in Section 2.5.2 of this thesis, the system used in this work to heat the ELP solution to 60°C (*i.e.* a hot stirrer

plate) failed to maintain a constant temperature, resulting in an average temperature of 64-65°C.

Finally, as shown in Figure 7.3B, already after 10 min of ELP, the HF substrate was found to be fully covered by a layer of Pd presenting the typical "cauliflower type" morphology of pure Pd membrane deposited on porous supports [181,182]. Furthermore, it can be seen that the initial Pd clusters up to 2 μm big formed after 10 minutes of ELP increased in size with the ELP time, being up to 20 μm big after 50 minutes.

7.2 Performance studies during the ammonia decomposition reaction using the Pd-based hollow fibre membrane reactor

From the preliminary performance studies of both Ru-based catalysts during the NH_3 decomposition reaction using the PBR (*i.e.* Chapter 4), Ru/Na-NCX has been found to be the most active catalyst. Based on that, and based on the thermodynamic limitations of the NH_3 decomposition reaction, the catalytic activity of Ru/Na-NCX was assessed also using a Pd-based hollow fibre membrane reactor (MHFR) in order to show the effects of using a membrane on the NH_3 conversion levels and prove the possibility to overcome the NH_3 decomposition thermodynamic limitations by means of an H_2 selective membrane. A schematic representation of the MHFR used in this work, which consists of a packed catalyst bed around the Pd membrane deposited on the outer surface of the hollow fibre, is shown in Figure 7.4.

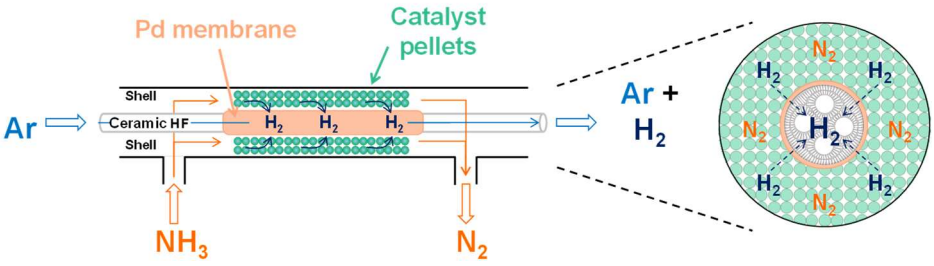

Figure 7.4. Schematic representation of the MHFR.

Figure 7.5A shows the comparison between the performance of both the PBR and the MHFR under the same conditions. The advantage of the membrane reactor is clearly shown, given that throughout the entire temperature range

studied, the NH_3 conversion in the MHFR is higher than that in the PBR. For instance, at 300°C, the NH_3 conversion in the MHFR is about 2 times higher than that in the PBR. This result can be explained due to the extraction of H_2 through the membrane, which according to Le Chatelier's principle, lead to a shift in the thermodynamic equilibrium of the reaction towards higher NH_3 conversions. In this regard, it is well known that the membrane is used to increase NH_3 conversion beyond the limits of thermodynamic equilibrium, enabling membrane reactors to operate at lower temperatures than conventional PBRs. As can be seen on the right side of Figure 7.5A, at temperatures ranging between 300°C and 450°C, the NH_3 conversion in the MHFR exceeds the thermodynamic equilibrium conversion.

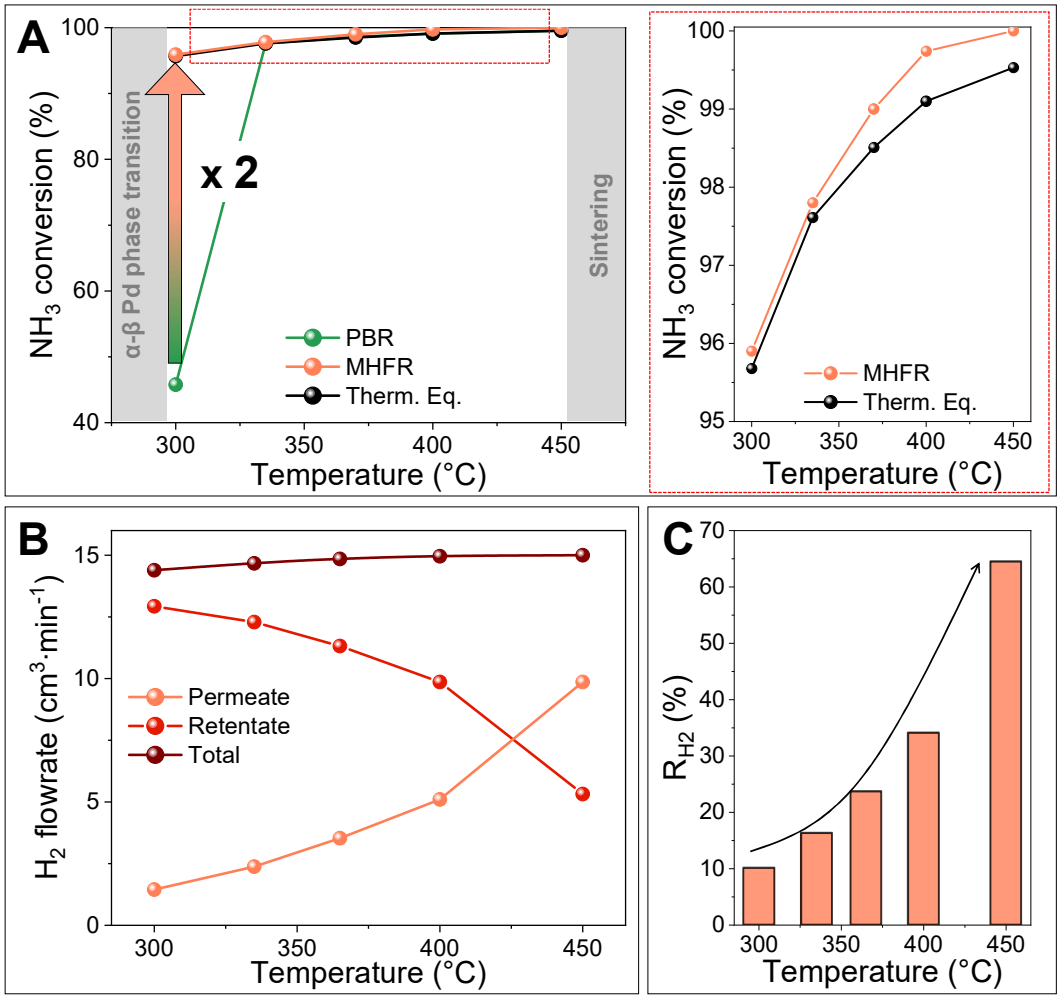

Figure 7.5. (A) NH_3 conversion in the PBR, in the MHFR, and at the thermodynamic equilibrium, (B) H_2 flowrate: total, retentate and permeate, and (C) R_{H_2} at different reaction temperatures.

As expected, the H_2 recovery (R_{H_2}) increased with the temperature (see Figure 7.5B and Figure 7.5C) following an exponential behaviour, going from 10.3% at 300°C to 64.5% at 450°C. In this regard, it is well known that the H_2 permeation through Pd membranes can be promoted by increasing the temperature, due to the increased solubility of H_2, resulting in higher values of R_{H_2} [106].

It is important to point out that permeability tests were not performed on the membrane in this work, although they could have provided additional information on the H_2 permeance, as they were not deemed essential. This decision was based on the fact that, as the permeability of the membrane is mainly influenced by its thickness and composition, as well as by the deposition method used, the H_2 permeance values could be extrapolated from our previous work in which Pd membranes were obtained using the same deposition method as in this work [101,102,115,117].

Finally, the conversion in the MHFR was predicted using the experimental R_{H_2} and the pseudo-equilibrium constant of the MHFR in Eq. 7.1, which has been defined as the ratio between the reaction products retained and the reactants:

$$K_{pred} = \frac{C_{N_2,pred}^{1/2} \times C_{H_2,pred}^{3/2}}{C_{NH_3,pred}}$$

$$= \frac{\left[C_{NH_{3_{in}}} \times \left(\frac{x_{NH_3,pred}}{2}\right)\right]^{1/2} \times \left[C_{NH_{3_{in}}} \times \left(\frac{3x_{NH_3,pred}}{2}\right) \times (1 - R_{H_2})\right]^{3/2}}{C_{NH_{3_{in}}} \times (1 - x_{NH_3,pseudo})} \quad 7.1$$

$$= \frac{\frac{x_{NH_3,pred}}{2}^{1/2} \times \left[\left(\frac{3x_{NH_3,pred}}{2}\right) \times (1 - R_{H_2})\right]^{3/2}}{(1 - x_{NH_3,pred})}$$

Where $x_{NH_3,pred}$ is the predicted NH_3 conversion at the equilibrium in a MHFR.

It is interesting to notice that, by using the R_{H_2} values obtained from the NH_3 decomposition reaction experiment using the MHFR and the x_{NH_3} values achieved during the reaction experiment using the PBR (pink and green light-off in Figure 7.6, respectively), the "predicted MHFR" NH_3 conversion coincides

with the NH_3 conversion attained during the reaction experiment using the MHFR. This result suggested that, given the NH_3 conversion achieved in a PBR, it is possible to predict the NH_3 conversion achievable in a MHFR for different R_{H_2} values.

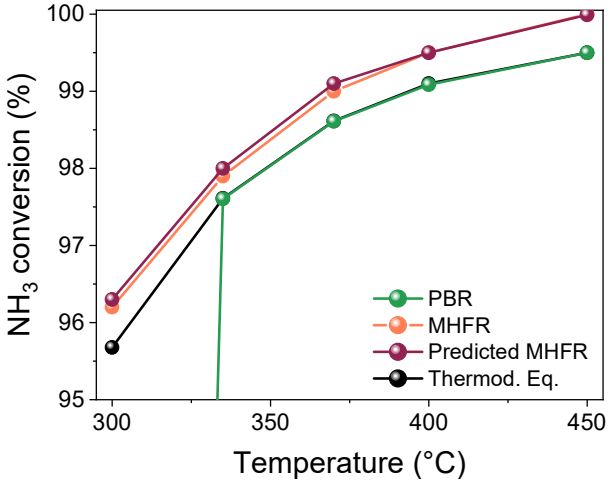

Figure 7.6. Comparison between NH_3 conversions achieved i) in the PBR, ii) at the thermodynamic equilibrium, iii) in the MHFR, and the predicted NH_3 conversion in a MHFR.

7.3 Design of the Pd-based hollow fibre membrane converter for on-board hydrogen production

The design feasibility study for on-board applications of the MHFR was carried out adopting the same assumptions and constraints used for the PBRs and HFRs designed in Section 6.2 (see Table 6.2). In addition to that, it was assumed that the NH_3 decomposition reaction in the MHFR follows the same kinetic as in the PBR. Based on the results reported in the previous section, the design of the MHFR was carried out at 450°C since it ensures an $x_{NH_3,pred}$ = 99.9999 %. In this regard, as discussed in the introduction of this work, the use of a MHFR relies on the possibility to produce high-purity H_2 in order to avoid poisoning the fuel cell installed into the H_2-fuelled vehicles with a threshold of NH_3 <1 ppm.

As for both the PBRs and HFRs, the MHFR volume and the catalyst loading required to produce 72 $m^3 \cdot h^{-1}$ (STP) of H_2, were estimated by using the NH_3 mass balance in Eq. 6.3. Likewise, the ΔP through the MHFR and the mass transfer limitations were estimated by using the Ergun equation (Eq. 6.4) and

the definition of the Thiele modulus ϕ^2 (Eq. 6.6), respectively. The results obtained at different operating temperatures were reported in Table 7.1.

Table 7.1. Design parameters for the MHFR for on-board H_2 production at 450°C and 1 atm, with and without H_2 streams mixing.

	Mixing	***NO Mixing***	***Optimised***
$x_{NH_3,pred}$ (%)	99.9999	99.9999	99.99999
R_{H_2} (%)	64.5	64.5	85.0
$\dot{V_{NH_3}}$ ($m^3 \cdot h^{-1}$ (STP))	48.0	74.5	48.0
d_p (mm)	1.2	0.7	1.1
W_{MHFR} (kg)	3.2	4.9	3.7
V_{MHFR} (L)	61.8	62.1	63.0
L_{MHFR} (m)	0.89	0.89	0.90
$N_{Pd\text{-}HF}$ (-)	107	165	95
ΔP (bar)	0.9	2.3	1.1
ϕ^2 (-)	0.4	0.4	0.4

As can be seen in the schematic representation in Figure 7.7A, since the R_{H_2} = 64.5% at 450°C, only 46.4 $m^3 \cdot h^{-1}$ (STP) of the produced H_2 permeate through the membrane, which is lower than the H_2 required to supply a power demand of 100kW (*i.e.* 72 $m^3 \cdot h^{-1}$ (STP)). Nevertheless, given that the NH_3 concentration at the exit of the reactor is lower than 1 ppm, thus low enough to avoid poisoning H_2 fuel cell, the two outlet streams of H_2, *i.e.* retentate and permeate, can be mixed before feeding them to the fuel cell.

Alternatively as can be seen in Figure 7.7B, to avoid mixing the two outlet streams of H_2, the $\dot{V_{NH_3}}$ can be increased to the extent that $\dot{V_{H_{2,P}}}$ = 72 $m^3 \cdot h^{-1}$ (STP). Based on that, given R_{H_2} = 64.5% at 450°C, the new $\dot{V_{NH_3}}$ was calculated to be equal to resulting equal to 74.5 $m^3 \cdot h^{-1}$ (STP). However, as reported in Table 7.1, despite this configuration allows meeting the on-board space constraints, to avert the mix of the two outlet streams of H_2, a higher catalyst loading (*i.e.* ~ 50% more) and a bigger set of Pd-plated HFs (*i.e.* ~ 60 units more) are needed compared to the MHFR in which the two streams are mixed. In addition to that, despite the catalyst pellets size optimisation (*i.e.* ϕ^2

≤ 0.4 and V ≤ V_{max} = 63 L [5]), the ΔP through the MHFR would increase from 0.9 bar to 2.3 bar if the two outlet streams of H_2 are not mixed. It is also important to point out that this configuration (*i.e.* $\dot{V}_{NH_3}$ = 74.5 $m^3 \cdot h^{-1}$ (STP) and R_{H_2} = 64.5%) result in the wasting of as much as 40 $m^3 \cdot h^{-1}$ (STP) of H_2.

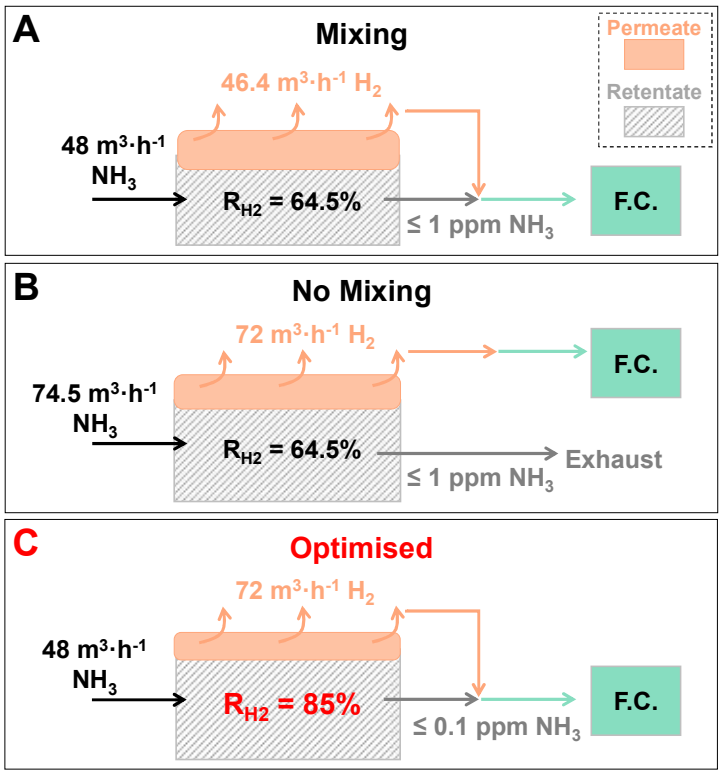

Figure 7.7. Effect of the inlet NH_3 flowrate $\dot{V}_{NH_3}$ on the permeated H_2 flowrate $\dot{V}_{H_{2,P}}$.

Therefore, to avoid wasting pure H_2, without compromising the ΔP through the MHFR, a new reactor design was considered for on-board H_2 production assuming R_{H_2} = 85%, which is the highest so far reported for Pd membranes working at 450°C and 1 atm [176]. As can be seen in Figure 7.7C and Table 7.1, this MHFR not only represents a feasible solution for on-board applications (*i.e.* V ≤ V_{max} = 63 L [5]), but it also ensures that there will be negligible traces of NH_3 at the exit of the reactor (*i.e.* less than 0.1 ppm). In addition, it demands the use of fewer Pd-plated HF units than the configuration in Figure 7.7A (*i.e.* 95 vs 107 units), partly reducing its manufacturing costs.

Note that in order to get a R_{H_2} = 85% at 450°C either a higher sweep gas flow or a thinner Pd membrane compared to those in this work can be used [107,115,175,176]. As mentioned in the previous section, the Pd membrane

herein synthesised, which lead to a R_{H_2} = 64,5% at 450°C, has a thickness 4 times bigger than the minimum theoretical thickness required to avoid leaks (*i.e.* ~ 11-13 μm and 3 μm, respectively) since two 90-minutes ELP cycles were performed to ensure the deposition of a uniform, defect-free membrane, and thermal resistant under the adopted operating conditions, deposited on the HF substrate. However, from the kinetic studies reported in Figure 7.3, a uniform and defect-free membrane with smaller thickness, but less thermal resistance, can be easily obtained already after one ELP cycle of 50 minutes.

Figure 7.8 shows a comparison between the optimised MHFR and both the PBR and the HFR designed in Section 6.3, given that Ru/Na-NCX is the catalyst used and the operating temperature is 450°C. Foremost, it is important to highlight that the MHFR allows achieving a higher NH_3 conversion than both the PBR and HFR under the same operating conditions (*i.e.* 450°C and 1 atm), thereby it presents the advantage over both reactors that it does not need to use an additional refining unit for the products stream to ensure the absence of NH_3 traces in the fuel-cell feed gas. Hence, when using a MHFR for on-board H_2 production, additional infrastructure to fit the adsorption unit in the vehicle is not needed.

Then, from the design studies herein carried out, it was found that the MHFR occupies a similar volume of the PBR (*i.e.* ~ 63 L) and leads to comparable ΔP thought the reactor. Furthermore, although the MHFR entails high manufacturing costs due to the use of a set of Pd-plated HFs (*i.e.* 95 units), it requires less catalyst loading compared to the PBR (*i.e.* 65% less).

Likewise, it was found that the MHFR requires more space and catalyst (*i.e.* ~ 18 times bigger volume and ~4 times more catalyst) than the HFR, and leads to remarkably higher ΔP through the reactor. These results suggest that, despite the disadvantage of the HFR of requiring an additional H_2 purification unit in order to achieve an NH_3 concentration lower than 1 ppm in the exhaust, the HFR could still represent a promising technology for on-board applications, being a good compromise between costs and efficiency.

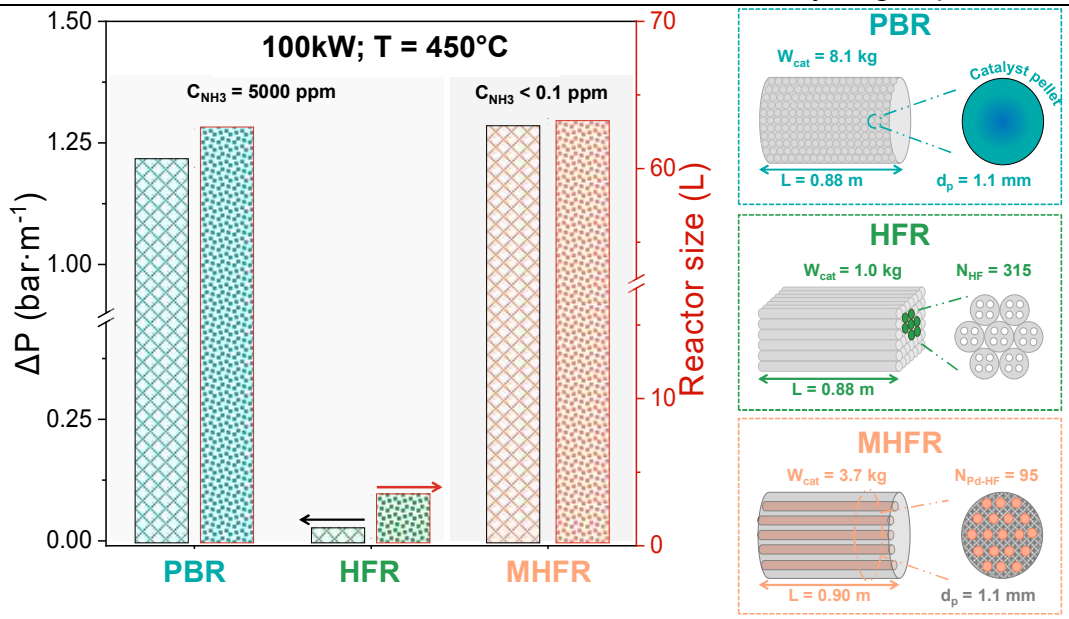

Figure 7.8. Comparison between the design of the PBR, HFR and MHFR for a power demand of 100 kW (i.e. 72 $m^3 \cdot h^{-1}$(STP) of H_2 supply) using Ru/Na-NCX.

Note that the use of an adsorption unit downstream of the HRF cannot be avoided. In this respect, based on the NH_3 thermodynamic limitations [26], to achieve 99.9999% NH_3 conversion using an HFR, a minimum operating temperature of 1000°C is required. However, working at such high temperature represents a severe safety risk due to the possibility of NH_3 auto-ignition (*i.e.* T> 651°C) if in contact with air. Likewise, at this high temperature, the catalysts designed in this work might not be stable.

To conclude, further evaluations on the overall costs and the total volume of both catalytic systems, *i.e.* i) MHFR and ii) HFR plus adsorption unit, has to be considered when comparing them to determine the optimal solution for on-board applications. Similarly, both thermal stability and thermal shock tests need to be performed to further understand the effects of the frequent start-up and shutdown cycles on the efficiency of the Pd membrane, thus further assessing the feasibility of the MHFR for on-board H_2 production.

7.4 Conclusions

Similarly to the findings obtained in Chapter 6, this feasibility study demonstrated the advantages of using a HF-based reactors, specifically in this

chapter a MHFR, over conventional PBRs for the NH_3 decomposition reaction for on-board applications.

In this respect, the MHRF was proved to be advantageous compared to the PBR leading to higher levels of NH_3 conversion under the same operating conditions. The feasibility study showed that also the MHFR herein designed represents a viable technology for the on-board H_2 production due to the advantage of combining in a single unit both the production and the purification of the H_2 outlet stream. However, both thermal stability and thermal shock tests need to be performed to further understand the effects of the frequent start-up and shutdown cycles on the efficiency of the Pd membrane.

Chapter 8 Final conclusions

With climate change heading towards an irreversible increase in global temperature, due in part to rising levels of CO_2 in the atmosphere, carbon-free alternatives to fossil fuels are needed. H_2 is a clean and renewable energy source for on-board applications, with the only product of its use in fuel cells being water. However, its use still presents some challenges due to its storage and transport limitations; therefore, the attention has turned to NH_3 as a potential H_2 storage and carrier molecule.

In this respect, this work aimed to design and assess the performance of a pioneering technology for on-board H_2 production for automotive applications via NH_3 decomposition, *i.e.* Multifunctional Catalytic Hollow Fibre-based Reactors. In this work, the effects of five different catalyst supports, two active phases and the use of a promoter, on the catalysts' performance during the NH_3 decomposition reaction were investigated. The performance of each catalyst was firstly investigated in a PBR, then the best catalyst from each of the two catalytic systems developed (*i.e.* Ru-based and Co/Mo-based), was chosen to be deposited inside the HF substrate to assess the performance of three HFRs and one MHFR. Each component of the catalysts, *i.e.* support, active phase and promoter, was developed separately and investigated in the individual chapters (*i.e.* Chapter 3-5), before being assembled in the HF-based reactors for performance evaluation (*i.e.* Chapter 6).

The work in Chapter 3 included how the five carbon xerogels employed as catalyst support, *i.e.* CX, ACX_{1h}, ACX_{5h}, UCX and NCX, have been synthesised and characterised, as well as how their structural, textural and chemical properties changed with their synthesis method. Investigating the effects of the CO_2 activation treatment on the properties of the supports, it was observed that after 1 h of CO_2 activation treatment, ACX_{1h} exhibited increased surface area and pore volume due to the opening of its micropores via the reverse Boudouard reaction (*i.e.* $CO_2 + C \rightleftarrows 2\ CO$). On the contrary, after 5 h of CO_2 activation treatment, ACX_{5h} exhibited a more ordered structure, thereby a lower surface area and pore volume, due to its partial crystallisation.

Nevertheless, according to the Air-TGA and TPD results, ACX_{5h} offered the advantages of enhanced thermal stability and basicity of ACX_{5h} when compared to both ACX_{1h} and CX (*i.e.* 5-12% higher burning temperature and 70-80% less oxygen surface groups). Likewise, the N-doping of carbon xerogels resulted in carbon materials with a lower surface area, less developed microporosity, and enhanced thermal stability and basicity when compared to non-doped counterparts. Furthermore, based on the N-doping method adopted, *i.e.* co-precursor method for UCX and post-synthesis NH_3/Air activation for NCX, the relative amount of the N functionalities introduced on the carbon xerogel surface changed. As per the XPS spectra deconvolution, the pyrrolic and quaternary N functionalities are predominant in UCX, whereas pyridinic N is predominant in NCX. These differences affected the thermal stability of both UCX and NCX, being the former more stable than the latter due to the fewer pyridine groups on its surface.

In Chapter 4, a comprehensive description of both the un-promoted and Na-promoted Ru-based catalysts was provided. Particular attention was paid to the effect of the properties of the different carbon xerogels used and the addition of Na as a promoter on their catalytic activity during the NH_3 decomposition reaction. This study proved that all carbon xerogels synthesised herein are efficient catalyst supports for the NH_3 decomposition reaction. However, it was found that the enhanced crystallinity, thermal stability and basicity of ACX_{5h}, UCX and NCX lead to an enhanced catalytic performance Ru-ACX_{5h}, Ru-UCX and Ru-NCX, *i.e.* 3.5, 3.2 and 3.9 times higher reaction rates, respectively, compared to Ru-CX. These results suggested that, for the NH_3 decomposition reaction, NCX is the optimal catalyst support for Ru-based catalysts. In addition, higher reaction rates for the NH_3 decomposition during the second reaction experiment were observed, indicating that Ru metal particles with an average particle size higher than 2.5 nm are beneficial for the reaction. Finally, since the metallic Na acted as an electronic promoter due to its electron donor effect on the Ru particles and the Na_2O acted as a structural promoter, preventing the sintering of Ru particles

during the reaction, it was found that the use of Na as a promoter favourably affected the performance of Na-promoted Ru-based catalysts.

Chapter 5 covered the description of the Co/Mo-based catalysts studied in this work. The performance studies showed that all Co/Mo-based catalysts are highly active during the NH_3 decomposition reaction. In particular, Co/Mo-NCX was identified as the optimal catalyst for the NH_3 decomposition reaction, due to its higher basicity and electrical conductivity than CX, lowest presence of oxygen groups on NCX surface, and promoting effects of the N atoms. In addition, this result suggested that, unlike Ru-based catalysts, the ideal metal particle size for Co/Mo-based catalysts is around 2.2 nm.

Based on the results from Chapter 4 and Chapter 5, the design and the assessment of several HF-based reactors have been carried out in Chapter 6, as well as their feasibility study for on-board H_2 production. Specifically, Co/Mo-NCX have been deposited in the HF substrate to develop an HFR, whereas Ru/Na-NXC have been used to develop both an HFR and a MHFR. This study showed, under the same operating conditions and using the same catalyst, all HFRs outperformed traditional PBRs. This result was attributed to the unique geometry of the HF substrate, which is known to improve the efficiency of the catalytic process due to a combination of factors: i) uniform distribution of the catalyst on the substrate, ii) narrower residence time distribution, and iii) minimised internal and external diffusion limitations. Similarly, it was found that the MHFR performed better than the corresponding PBR due to the use of the Pd membrane, which allowed to selectively separate H_2 during the NH_3 decomposition reaction and to achieve higher NH_3 conversion levels.

Likewise, from the feasibility study for on-board applications, it was observed that the HF-based reactors designed in this work, *i.e.* the two HFRs and the MHFR, offer a potential solution for on-board H_2 production via NH_3 decomposition, representing a more compact, efficient and affordable alternative to traditional PBRs. In the first case, despite both reactors needing to be fitted in a vehicle together with an additional NH_3 desorption unit to avoid

poisoning the fuel cell, the HFR was found to increase the efficiency of the catalysts in comparison to the PBR. Furthermore, the HFR showed high thermal stability and catalyst adherence, and offered noteworthy advantages compared to the PBR, in terms of cost (*i.e.* up to 80% less catalyst), space occupied (*i.e.* up to 95% smaller), and efficiency (*i.e.* >99% less pressure drop and mass transfer limitations). In addition, compared to the latest technologies developed for the NH_3 decomposition (*i.e.* microreactors), it allows working at lower operating temperatures and catalyst loading, without compromising the ΔP.

In the second case, it was found that although the MHFR results in higher manufacturing costs due to the use of a set of Pd-plated HFs (*i.e.* 95 units), it requires remarkably less catalyst than the PBR (*i.e.* 65% less) for a similar reactor volume. In addition to that, the MHFR presents the benefit over the PBR that it does not need to use an additional refining unit for the products' stream to ensure the absence of NH_3 traces in the fuel-cell feed gas.

However, further studies need to be done in order to suggest the more convenient on-board H_2 production technology between the HFRs and the MHFRs. In this respect, the overall costs and the total volume of both catalyst systems need to be taken into consideration, including the cost of the catalyst and of the membranes, as well as the volume needed to fit an NH_3 adsorption unit downstream of the HFR. Similarly, both thermal stability and thermal shock tests need to be performed to further understand the effects of the frequent start-up and shutdown cycles on the efficiency of the Pd membrane, thus further assessing the feasibility of the MHFR for on-board H_2 production. To conclude, to exploit the advantages of the HFs as support of both the catalyst and the Pd membrane, combining the advantages of the HFRs with membrane separation, an additional reactor could be developed and assessed during the NH_3 decomposition reaction, in which the catalyst and the membrane are deposited inside and on the outer surface of the HF substrate, respectively (see the Configuration B of the HFMR in Figure 1.10).

References

[1] Greenhouse gas emissions from transport in Europe, (2021). https://www.eea.europa.eu/ims/greenhouse-gas-emissions-from-transport (accessed October 12, 2021).

[2] J.D. Holladay, Y. Wang, E. Jones, Review of developments in portable hydrogen production using microreactor technology, Chem. Rev. 104 (2004) 4767–4790.

[3] A.K. Hill, L. Torrente-murciano, In-situ H2 production via low temperature decomposition of ammonia : Insights into the role of cesium as a promoter, Int. J. Hydrogen Energy. 39 (2014) 7646–7654.

[4] S. Satyapal, J. Petrovic, C. Read, G. Thomas, G. Ordaz, The US Department of Energy's National Hydrogen Storage Project: Progress towards meeting hydrogen-powered vehicle requirements, Catal. Today. 120 (2007) 246–256.

[5] M. Burt, New Mirai hydrogen fuel cell electric vehicle – under the skin, (2020). https://mag.toyota.co.uk/new-mirai-hydrogen-fuel-cell-electric-vehicle/ (accessed November 20, 2021).

[6] Daily Metal Spot Prices, (2022). https://www.dailymetalprice.com/metalprices.php?c=ru&u=kg&d=1 (accessed January 10, 2022).

[7] D. Cheddie, Ammonia as a hydrogen source for fuel cells: a review, InTech, 2012.

[8] S. Chiuta, R.C. Everson, H.W.J.P. Neomagus, P. Van Der Gryp, D.G. Bessarabov, Reactor technology options for distributed hydrogen generation via ammonia decomposition: A review, Int. J. Hydrogen Energy. 38 (2013) 14968–14991.

[9] A History of Hyundai and Fuel Cell Technology, (2020).

https://www1.hyundai.news/uk/brand/a-history-of-hyundai-and-fuel-cell-technology/ (accessed November 20, 2021).

[10] ASTON MARTIN MAKES HYBRID HYDROGEN HISTORY AT NÜRBURGRING, (2013). https://www2.astonmartin.com/en/racing/news/2013/04/29/aston-martin-makes-hybrid-hydrogen-history-at-nürburgring (accessed November 20, 2021).

[11] Everyday testing of BMW i Hydrogen NEXT with hydrogen fuel cell drive train begins., (2021). https://www.press.bmwgroup.com/global/article/detail/T0334225EN/everyday-testing-of-bmw-i-hydrogen-next-with-hydrogen-fuel-cell-drive-train-begins?language=en (accessed November 20, 2021).

[12] M.P. Suh, H.J. Park, T.K. Prasad, D.-W. Lim, Hydrogen storage in metal--organic frameworks, Chem. Rev. 112 (2012) 782–835.

[13] B. Viswanathan, Chapter 10 - Hydrogen Storage, in: B.B.T.-E.S. Viswanathan (Ed.), Elsevier, Amsterdam, 2017: pp. 185–212.

[14] M. Mohan, V.K. Sharma, E.A. Kumar, V. Gayathri, Hydrogen storage in carbon materials—A review, Energy Storage. 1 (2019) e35.

[15] G.D. Berry, J. Martinez-Frias, F. Espinosa-Loza, S.M. Aceves, Hydrogen storage and transportation, (2004).

[16] S.F. Yin, B.Q. Xu, X.P. Zhou, C.T. Au, A mini-review on ammonia decomposition catalysts for on-site generation of hydrogen for fuel cell applications, Appl. Catal. A Gen. 277 (2004) 1–9.

[17] D. Cheddie, Ammonia as a Hydrogen Source for Fuel Cells : A Review, (2012).

[18] K. Fothergill, S. Greenwood, J. Makepeace, I. Wilkinson, Ammonia to Green Hydrogen Project, 33 (2015) 1–70.

[19] M. Aziz, A.T. Wijayanta, A.B. Nandiyanto, Ammonia as Effective Hydrogen Storage: A Review on Production, Storage and Utilization, Energies. 13 (2020).

[20] M.H. Hasan, T.M. Mahlia, M. Mofijur, I.M. Rizwanul Fattah, F. Handayani, H.C. Ong, A.S. Silitonga, A Comprehensive Review on the Recent Development of Ammonia as a Renewable Energy Carrier, Energies. 14 (2021).

[21] S. Chiuta, R.C. Everson, H.W.J.P. Neomagus, L.A. Le Grange, D.G. Bessarabov, A modelling evaluation of an ammonia-fuelled microchannel reformer for hydrogen generation, Int. J. Hydrogen Energy. 39 (2014) 11390–11402.

[22] M. Wang, J. Li, L. Chen, Y. Lu, Miniature NH3 cracker based on microfibrous entrapped Ni-CeO2/Al2O3 catalyst monolith for portable fuel cell power supplies, Int. J. Hydrogen Energy. 34 (2009) 1710–1716.

[23] S. Chiuta, R.C. Everson, H.W.J.P. Neomagus, P. van der Gryp, D.G. Bessarabov, Reactor technology options for distributed hydrogen generation via ammonia decomposition: A review, Int. J. Hydrogen Energy. 38 (2013) 14968–14991.

[24] F.R. García-García, Y.H. Ma, I. Rodríguez-Ramos, A. Guerrero-Ruiz, High purity hydrogen production by low temperature catalytic ammonia decomposition in a multifunctional membrane reactor, Catal. Commun. 9 (2008) 482–486.

[25] A. Engström, Determination of acceptable contaminant levels for PEM fuel cell stacks and poisoning mitigation strategies, (2014).

[26] S.F. Yin, Q.H. Zhang, B.Q. Xu, W.X. Zhu, C.F. Ng, C.T. Au, Investigation on the catalysis of COx-free hydrogen generation from ammonia, J. Catal. 224 (2004) 384–396.

[27] G. Ertl, M. Huber, Mechanism and kinetics of ammonia decomposition

on iron, J. Catal. 61 (1980) 537–539.

[28] W. Tsai, W.H. Weinberg, Steady-state decomposition of ammonia on the ruthenium (001) surface, J. Phys. Chem. 91 (1987) 5302–5307.

[29] E. Shustorovich, A.T. Bell, Synthesis and decomposition of ammonia on transition metal surfaces: bond-order-conservation-Morse-potential analysis, Surf. Sci. Lett. 259 (1991) L791–L796.

[30] T. V Choudhary, C. Sivadinarayana, D.W. Goodman, Catalytic ammonia decomposition: COx-free hydrogen production for fuel cell applications, Catal. Letters. 72 (2001) 197–201.

[31] R. van Hardeveld, A. van Montfoort, The influence of crystallite size on the adsorption of molecular nitrogen on nickel, palladium and platinum: An infrared and electron-microscopic study, Surf. Sci. 4 (1996) 396–430.

[32] C.J.H. Jacobsen, S. Dahl, P.L. Hansen, E. Törnqvist, L. Jensen, H. Topsøe, D. V Prip, P.B. Møenshaug, I. Chorkendorff, Structure sensitivity of supported ruthenium catalysts for ammonia synthesis, J. Mol. Catal. A Chem. 163 (2000) 19–26.

[33] F.R. García-García, J. Álvarez-Rodríguez, I. Rodríguez-Ramos, A. Guerrero-Ruiz, The use of carbon nanotubes with and without nitrogen doping as support for ruthenium catalysts in the ammonia decomposition reaction, Carbon N. Y. 48 (2010) 267–276.

[34] F.R. García-García, E. Gallegos-Suarez, M. Fernández-García, A. Guerrero-Ruiz, I. Rodríguez-Ramos, Understanding the role of oxygen surface groups: The key for a smart ruthenium-based carbon-supported heterogeneous catalyst design and synthesis, Appl. Catal. A Gen. 544 (2017) 66–76.

[35] T.E. Bell, L. Torrente-Murciano, H2 Production via Ammonia Decomposition Using Non-Noble Metal Catalysts: A Review, Top. Catal. 59 (2016) 1438–1457.

[36] J. Ji, X. Duan, G. Qian, X. Zhou, G. Tong, W. Yuan, Towards an efficient CoMo/g-Al2O3 catalyst using metal amine metallate as an active phase precursor: Enhanced hydrogen production by ammonia decomposition, Int. J. Hydrogen Energy. 39 (2014) 12490–12498.

[37] L. Torrente-Murciano, A.K. Hill, T.E. Bell, Ammonia decomposition over cobalt/carbon catalysts—Effect of carbon support and electron donating promoter on activity, Catal. Today. 286 (2017) 131–140.

[38] X.-K. Li, W.-J. Ji, J. Zhao, S.-J. Wang, C.-T. Au, Ammonia decomposition over Ru and Ni catalysts supported on fumed SiO2, MCM-41, and SBA-15, J. Catal. 236 (2005) 181–189.

[39] H. Zhang, Y.A. Alhamed, Y. Kojima, A.A. Al-Zahrani, H. Miyaoka, L.A. Petrov, Structure and catalytic properties of Ni/MWCNTs and Ni/AC catalysts for hydrogen production via ammonia decomposition, Int. J. Hydrogen Energy. 39 (2014) 277–287.

[40] I. Lucentini, A. Casanovas, J. Llorca, Catalytic ammonia decomposition for hydrogen production on Ni, Ru and NiRu supported on CeO2, Int. J. Hydrogen Energy. 44 (2019) 12693–12707.

[41] C.J.H. Jacobsen, S. Dahl, B.S. Clausen, S. Bahn, A. Logadottir, J.K. Nørskov, Catalyst design by interpolation in the periodic table: bimetallic ammonia synthesis catalysts, J. Am. Chem. Soc. 123 (2001) 8404–8405.

[42] S. Yin, Q. Zhang, B. Xu, W. Zhu, Investigation on the catalysis of CO x -free hydrogen generation from ammonia, 224 (2004) 384–396.

[43] J. Zhang, J.-O. Müller, W. Zheng, D. Wang, D. Su, R. Schlögl, Individual Fe−Co Alloy Nanoparticles on Carbon Nanotubes: Structural and Catalytic Properties, Nano Lett. 8 (2008) 2738–2743.

[44] W. Guo, M. Stamatakis, D.G. Vlachos, Design Principles of Heteroepitaxial Bimetallic Catalysts, ACS Catal. 3 (2013) 2248–2255.

[45] D.A. Hansgen, D.G. Vlachos, J.G. Chen, Using first principles to predict bimetallic catalysts for the ammonia decomposition reaction, Nat. Chem. 2 (2010) 484–489.

[46] X. Duan, G. Qian, X. Zhou, D. Chen, W. Yuan, MCM-41 supported Co A Mo bimetallic catalysts for enhanced hydrogen production by ammonia decomposition, Chem. Eng. J. 207–208 (2012) 103–108.

[47] C.J.H. Jacobsen, S. Dahl, A. Boisen, B.S. Clausen, H. Topsøe, A. Logadottir, J.K. Nørskov, Optimal catalyst curves: Connecting density functional theory calculations with industrial reactor design and catalyst selection, J. Catal. 205 (2002) 382–387.

[48] S.F. Yin, B.Q. Xu, C.F. Ng, C.T. Au, Nano Ru/CNTs: A highly active and stable catalyst for the generation of COx-free hydrogen in ammonia decomposition, Appl. Catal. B Environ. 48 (2004) 237–241.

[49] X. Duan, J. Ji, X. Yan, G. Qian, D. Chen, X. Zhou, Understanding Co-Mo Catalyzed Ammonia Decomposition: Influence of Calcination Atmosphere and Identification of Active Phase, ChemCatChem. 8 (2016) 938–945.

[50] H.E. Van Dam, H. Van Bekkum, Preparation of platinum on activated carbon, J. Catal. 131 (1991) 335–349.

[51] Z.H. Zhong, K.I. Aika, The effect of hydrogen treatment of active carbon on Ru catalysts for ammonia synthesis, J. Catal. 173 (1998) 535–539.

[52] K. Aika, H. Hori, A. Ozaki, Activation of nitrogen by alkali metal promoted transition metal I. Ammonia synthesis over ruthenium promoted by alkali metal, J. Catal. 27 (1972) 424–431.

[53] W. Raróg, Z. Kowalczyk, J. Sentek, D. Składanowski, D. Szmigiel, J. Zieliński, Decomposition of ammonia over potassium promoted ruthenium catalyst supported on carbon, Appl. Catal. A Gen. 208 (2001) 213–216.

[54] S.F. Yin, B.Q. Xu, W.X. Zhu, C.F. Ng, X.P. Zhou, C.T. Au, Carbon nanotubes-supported Ru catalyst for the generation of CO x-free hydrogen from ammonia, in: Catal. Today, 2004: pp. 27–38.

[55] X. Duan, J. Zhou, G. Qian, P. Li, X. Zhou, D. Chen, Carbon Nanofiber-Supported Ru Catalysts for Hydrogen Evolution by Ammonia Decomposition, Chinese J. Catal. 31 (2010) 979–986.

[56] R.Z. Sørensen, A. Klerke, U. Quaade, S. Jensen, O. Hansen, C.H. Christensen, Promoted Ru on high-surface area graphite for efficient miniaturized production of hydrogen from ammonia, Catal. Letters. 112 (2006) 77–81.

[57] K.P. DE JONG, J.W. GEUS, Carbon Nanofibers: Catalytic Synthesis and Applications, Catal. Rev. 42 (2000) 481–510.

[58] I. Rossetti, N. Pernicone, L. Forni, Graphitised carbon as support for Ru/C ammonia synthesis catalyst, Catal. Today. 102–103 (2005) 219–224.

[59] M.C.J. Bradford, P.E. Fanning, M.A. Vannice, Kinetics of NH3Decomposition over Well Dispersed Ru, J. Catal. 172 (1997) 479–484.

[60] J. Zhang, H. Xu, Q. Ge, W. Li, Highly efficient Ru/MgO catalysts for NH3 decomposition: Synthesis, characterization and promoter effect, Catal. Commun. 7 (2006) 148–152.

[61] M. Melchionna, S. Marchesan, M. Prato, P. Fornasiero, Carbon nanotubes and catalysis: the many facets of a successful marriage, Catal. Sci. Technol. 5 (2015) 3859–3875.

[62] B. Stöhr, H.P. Boehm, R. Schlögl, Enhancement of the catalytic activity of activated carbons in oxidation reactions by thermal treatment with ammonia or hydrogen cyanide and observation of a superoxide species as a possible intermediate, Carbon N. Y. 29 (1991) 707–720.

[63] H.F. Gorgulho, F. Gonçalves, M.F.R. Pereira, J.L. Figueiredo, Synthesis and characterization of nitrogen-doped carbon xerogels, Carbon N. Y. 47 (2009) 2032–2039.

[64] R. Czerw, M. Terrones, J.-C. Charlier, X. Blase, B. Foley, R. Kamalakaran, N. Grobert, H. Terrones, D. Tekleab, P.M. Ajayan, others, Identification of electron donor states in N-doped carbon nanotubes, Nano Lett. 1 (2001) 457–460.

[65] W. Shen, Z. Li, Y. Liu, Surface Chemical Functional Groups Modification of Porous Carbon, Recent Patents Chem. Eng. 1 (2012) 27–40.

[66] P. Ayala, R. Arenal, M. Rümmeli, A. Rubio, T. Pichler, The doping of carbon nanotubes with nitrogen and their potential applications, Carbon N. Y. 48 (2010) 575–586.

[67] L.M. Ombaka, P.G. Ndungu, V.O. Nyamori, Tuning the nitrogen content and surface properties of nitrogen-doped carbon nanotubes synthesized using a nitrogen-containing ferrocenyl derivative and ethylbenzoate, J. Mater. Sci. 50 (2015) 1187–1200.

[68] S. Ren, F. Huang, J. Zheng, S. Chen, H. Zhang, Ruthenium supported on nitrogen-doped ordered mesoporous carbon as highly active catalyst for NH3 decomposition to H2, Int. J. Hydrogen Energy. 42 (2017) 5105–5113.

[69] S.F. Yin, B.Q. Xu, W.X. Zhu, C.F. Ng, X.P. Zhou, C.T. Au, Carbon nanotubes-supported Ru catalyst for the generation of COx-free hydrogen from ammonia, Catal. Today. 93 (2004) 27–38.

[70] F.R. García-García, B.F.K. Kingsbury, M.A. Rahman, K. Li, Asymmetric ceramic hollow fibres applied in heterogeneous catalytic gas phase reactions, Catal. Today. 193 (2012) 20–30.

[71] F.R. García-García, M.A. Rahman, I.D. González-Jiménez, K. Li, Catalytic hollow fibre membrane micro-reactor: High purity H2production

by WGS reaction, Catal. Today. 171 (2011) 281–289.

[72] C. Lin, J.A. Ritter, Carbonization and activation of sol-gel derived carbon xerogels, Carbon N. Y. 38 (2000) 849–861.

[73] T. Horikawa, J. Hayashi, K. Muroyama, Controllability of pore characteristics of resorcinol--formaldehyde carbon aerogel, Carbon N. Y. 42 (2004) 1625–1633.

[74] M.G. Plaza, F. Rubiera, J.J. Pis, C. Pevida, Ammoxidation of carbon materials for CO2 capture, Appl. Surf. Sci. 256 (2010) 6843–6849.

[75] S.A. Al-Muhtaseb, J.A. Ritter, Preparation and properties of resorcinol--formaldehyde organic and carbon gels, Adv. Mater. 15 (2003) 101–114.

[76] H.T. Gomes, P. V. Samant, P. Serp, P. Kalck, J.L. Figueiredo, J.L. Faria, Carbon nanotubes and xerogels as supports of well-dispersed Pt catalysts for environmental applications, Appl. Catal. B Environ. 54 (2004) 175–182.

[77] S. Lambert, N. Job, L. D'Souza, M.F.R. Pereira, R. Pirard, B. Heinrichs, J.L. Figueiredo, J.P. Pirard, J.R. Regalbuto, Synthesis of very highly dispersed platinum catalysts supported on carbon xerogels by the strong electrostatic adsorption method, J. Catal. 261 (2009) 23–33.

[78] J.P.S. Sousa, M.F.R. Pereira, J.L. Figueiredo, NO oxidation over nitrogen doped carbon xerogels, Appl. Catal. B Environ. 125 (2012) 398–408.

[79] R.P. Rocha, J. Restivo, J.P.S. Sousa, J.J.M. Órfão, M.F.R. Pereira, J.L. Figueiredo, Nitrogen-doped carbon xerogels as catalysts for advanced oxidation processes, Catal. Today. 241 (2015) 73–79.

[80] R.W. Pekala, Organic aerogels from the polycondensation of resorcinol with formaldehyde, J. Mater. Sci. 24 (1989) 3221–3227.

[81] F.J. Maldonado-Hódar, M.A. Ferro-García, J. Rivera-Utrilla, C. Moreno-Castilla, Synthesis and textural characteristics of organic aerogels, transition-metal-containing organic aerogels and their carbonized derivatives, Carbon N. Y. 37 (1999) 1199–1205.

[82] M.S. Contreras, C.A. Páez, L. Zubizarreta, A. Léonard, S. Blacher, C.G. Olivera-Fuentes, A. Arenillas, J.-P. Pirard, N. Job, A comparison of physical activation of carbon xerogels with carbon dioxide with chemical activation using hydroxides, Carbon N. Y. 48 (2010) 3157–3168.

[83] M.B. Barbosa, J.P. Nascimento, P.B. Martelli, C.A. Furtado, N.D.S. Mohallem, H.F. Gorgulho, Electrochemical properties of carbon xerogel containing nitrogen in a carbon matrix, Microporous Mesoporous Mater. 162 (2012) 24–30.

[84] S.A. Messele, O. Soares, J.J.M. Órfão, C. Bengoa, J. Font, Zero-valent iron supported on nitrogen-doped carbon xerogel as catalysts for the oxidation of phenol by fenton-like system, Environ. Technol. 39 (2018) 2951–2958.

[85] N. Job, M.F.R. Pereira, S. Lambert, A. Cabiac, G. Delahay, J.F. Colomer, J. Marien, J.L. Figueiredo, J.P. Pirard, Highly dispersed platinum catalysts prepared by impregnation of texture-tailored carbon xerogels, J. Catal. 240 (2006) 160–171.

[86] B.F. Machado, H.T. Gomes, P. Serp, P. Kalck, J.L. Figueiredo, J.L. Faria, Carbon xerogel supported noble metal catalysts for fine chemical applications, Catal. Today. 149 (2010) 358–364.

[87] F.R. García-García, A. Guerrero-Ruiz, I. Rodríguez-Ramos, A. Goguet, S.O. Shekhtman, C. Hardacre, TAP studies of ammonia decomposition over Ru and Ir catalysts, Phys. Chem. Chem. Phys. 13 (2011) 12892–12899.

[88] W. Raróg-pilecka, D. Szmigiel, Z. Kowalczyk, Ammonia decomposition

over the carbon-based ruthenium catalyst promoted with barium or cesium, 218 (2003) 465–469.

[89] F.R. García-García, A. Guerrero-Ruiz, I. Rodríguez-Ramos, Role of B5-type sites in Ru catalysts used for the NH3 decomposition reaction, in: Top. Catal., 2009: pp. 758–764.

[90] A.K. Hill, L. Torrente-Murciano, Low temperature H2 production from ammonia using ruthenium-based catalysts: Synergetic effect of promoter and support, Appl. Catal. B Environ. 172 (2015) 129–135.

[91] Z. Kowalczyk, M. Krukowski, W. Raróg-Pilecka, D. Szmigiel, J. Zielinski, Carbon-based ruthenium catalyst for ammonia synthesis: Role of the barium and caesium promoters and carbon support, Appl. Catal. A Gen. 248 (2003) 67–73.

[92] S.R. Tennison, Catalytic ammonia synthesis: fundamentals and practice, in: Fundam. Appl. Catal., J.R. Jenni, Plenum Press, New York, 1991.

[93] Christian, M. Mitchell, D.-P. Kim, P.J.A. Kenis, Ceramic microreactors for on-site hydrogen production, J. Catal. 241 (2006) 235–242.

[94] S. Chiuta, R.C. Everson, H.W.J.P. Neomagus, D.G. Bessarabov, Performance evaluation of a high-throughput microchannel reactor for ammonia decomposition over a commercial Ru-based catalyst, Int. J. Hydrogen Energy. 40 (2015) 2921–2926.

[95] N.I. Mahyon, T. Li, R. Martinez-Botas, Z. Wu, K. Li, A new hollow fibre catalytic converter design for sustainable automotive emissions control, Catal. Commun. 120 (2019) 86–90.

[96] M. García-Vázquez, G. Zhang, Z. Hong, X. Gu, F.R. García-García, Micro-structured catalytic converter for residual methane emission abatement, Chem. Eng. J. 396 (2020) 125379.

[97] F.R. García-García, K. Li, New catalytic reactors prepared from symmetric and asymmetric ceramic hollow fibres, Appl. Catal. A Gen. 456 (2013) 1–10.

[98] M. García-Vázquez, P. Marín, S. Ordóñez, K. Li, J. Tan, G. Zhang, F.R. García-García, Scaling up a hollow fibre reactor: A study on non-PGM hollow fibre after-treatments for methane emission control under extreme conditions, J. Environ. Chem. Eng. 9 (2021) 106880.

[99] F.R. García-García, S.C. Tsang, K. Li, Hollow fibre based reactors for an enhanced H2 production by methanol steam reforming, J. Memb. Sci. 455 (2014) 92–102.

[100] M.A. Rahman, F.R. García-García, K. Li, Development of a catalytic hollow fibre membrane microreactor as a microreformer unit for automotive application, J. Memb. Sci. 390–391 (2012) 68–75.

[101] F.R. García-García, L. Torrente-Murciano, D. Chadwick, K. Li, Hollow fibre membrane reactors for high H2 yields in the WGS reaction, J. Memb. Sci. 405–406 (2012) 30–37.

[102] E. Gallegos-Suárez, F.R. García-García, I.D. González-Jiménez, I. Rodríguez-Ramos, A. Guerreo Ruiz, K. Li, Ceramic hollow fibres catalytic enhanced reactors for glycerol steam reforming, Catal. Today. 233 (2014) 21–30.

[103] J.G.S. Marcano, T.T. Tsotsis, Catalytic membranes and membrane reactors, Wiley-VCH Weinheim, 2002.

[104] K. Li, Ceramic membranes for separation and reaction, John Wiley & Sons, 2007.

[105] A. Julbe, D. Farrusseng, C. Guizard, Porous ceramic membranes for catalytic reactors—overview and new ideas, J. Memb. Sci. 181 (2001) 3–20.

[106] S. Yun, S.T. Oyama, Correlations in palladium membranes for hydrogen separation: A review, J. Memb. Sci. 375 (2011) 28–45.

[107] G.J. Grashoff, C.E. Pilkington, C.W. Corti, The purification of hydrogen, Platin. Met. Rev. 27 (1983) 157–169.

[108] A. Basile, F. Gallucci, S. Tosti, Synthesis, characterization, and applications of palladium membranes, Membr. Sci. Technol. 13 (2008) 255–323.

[109] T.B. Flanagan, W.A. Oates, The palladium-hydrogen system, Annu. Rev. Mater. Sci. 21 (1991) 269–304.

[110] H. Li, H. Xu, W. Li, Study of n value and α/β palladium hydride phase transition within the ultra-thin palladium composite membrane, J. Memb. Sci. 324 (2008) 44–49.

[111] S.K. Gade, P.M. Thoen, J.D. Way, Unsupported palladium alloy foil membranes fabricated by electroless plating, J. Memb. Sci. 316 (2008) 112–118.

[112] A. Li, W. Liang, R. Hughes, Fabrication of defect-free Pd/α-Al2O3 composite membranes for hydrogen separation, Thin Solid Films. 350 (1999) 106–112.

[113] D. Alique, D. Martinez-Diaz, R. Sanz, J.A. Calles, Review of supported pd-based membranes preparation by electroless plating for ultra-pure hydrogen production, Membranes (Basel). 8 (2018) 5.

[114] I.P. Mardilovich, E. Engwall, Y.H. Ma, Dependence of hydrogen flux on the pore size and plating surface topology of asymmetric Pd-porous stainless steel membranes, Desalination. 144 (2002) 85–89.

[115] F.R. García-García, M.A. Rahman, B.F.K. Kingsbury, K. Li, A novel catalytic membrane microreactor for COxfree H2production, Catal. Commun. 12 (2010) 161–164.

[116] F.R. García-García, M.A. Rahman, B.F.K. Kingsbury, K. Li, Asymmetric ceramic hollow fibres: New micro-supports for gas-phase catalytic reactions, Appl. Catal. A Gen. 393 (2011) 71–77.

[117] M.A. Rahman, F.R. García-García, M.D.I. Hatim, B.F.K. Kingsbury, K. Li, Development of a catalytic hollow fibre membrane micro-reactor for high purity H2 production, J. Memb. Sci. 368 (2011) 116–123.

[118] Z. Shi, Y. Zhang, C. Cai, C. Zhang, X. Gu, Preparation and characterization of α-Al2O3 hollow fiber membranes with four-channel configuration, Ceram. Int. 41 (2015) 1333–1339.

[119] H.F. Gorgulho, F. Gonçalves, M.F.R. Pereira, J.L. Figueiredo, Synthesis and characterization of nitrogen-doped carbon xerogels, Carbon N. Y. 47 (2009) 2032–2039.

[120] J. Rouquerol, F. Rouquerol, P. Llewellyn, G. Maurin, K.S.W. Sing, Adsorption by powders and porous solids: principles, methodology and applications, 2nd ed., Elsevier Ltd., 2014.

[121] K.S.W. Sing, Reporting physisorption data for gas/solid systems with special reference to the determination of surface area and porosity (Recommendations 1984), Pure Appl. Chem. 57 (1985) 603–619.

[122] D.D. Do, Adsorption Analysis: Equilibria and Kinetics, 1998.

[123] J.L. Figueiredo, Functionalization of porous carbons for catalytic applications, J. Mater. Chem. A. 1 (2013) 9351–9364.

[124] B. Imelik, J.C. Vedrine, Catalyst characterization: physical techniques for solid materials, Springer Science & Business Media, 2013.

[125] S.M. Tougaard, Surface analysis| X-ray photoelectron spectroscopy, in: Encycl. Anal. Sci., Elsevier, 2013: pp. 400–409.

[126] J.F. Watts, J. Wolstenholme, An introduction to surface analysis by XPS

and AES, John Wiley & Sons, 2019.

[127] P.J. Goodhew, J. Humphreys, Electron microscopy and analysis, CRC Press, 2000.

[128] P.S. Kumar, K.G. Pavithra, M. Naushad, Characterization techniques for nanomaterials, in: Nanomater. Sol. Cell Appl., Elsevier, 2019: pp. 97–124.

[129] D.B. Williams, C.B. Carter, Transmission Electron Microscopy: Spectrometry David B. Williams and C. Barry Cart. IV., Plenum, 1996.

[130] J.W. Arblaster, Crystallographic properties of ruthenium, Platin. Met. Rev. 57 (2013) 127–136.

[131] N.R. Lugg, G. Kothleitner, N. Shibata, Y. Ikuhara, On the quantitativeness of EDS STEM, Ultramicroscopy. 151 (2015) 150–159.

[132] A. Popelka, S. Zavahir, S. Habib, Morphology analysis, in: Polym. Sci. Innov. Appl., Elsevier, 2020: pp. 21–68.

[133] W. Kiciński, M. Szala, M. Nita, Structurally tailored carbon xerogels produced through a sol–gel process in a water–methanol–inorganic salt solution, J. Sol-Gel Sci. Technol. 58 (2011) 102–113.

[134] A.-L. Peikolainen, M. Uibu, J. Kozlova, H. Mändar, A. Tamm, A. Aabloo, Carbon xerogel from 5-methylresorcinol-formaldehyde gel: The controllability of structural properties, Carbon Trends. 3 (2021) 100037.

[135] S.C. Wilschefski, M.R. Baxter, Inductively coupled plasma mass spectrometry: introduction to analytical aspects, Clin. Biochem. Rev. 40 (2019) 115.

[136] S.N. Paglieri, J.D. Way, Innovations in palladium membrane research, Sep. Purif. Methods. 31 (2002) 1–169.

[137] J.N. Keuler, L. Lorenzen, Developing a heating procedure to optimise

hydrogen permeance through Pd–Ag membranes of thickness less than 2.2 μm, J. Memb. Sci. 195 (2002) 203–213.

[138] P.A. Webb, An introduction to the physical characterization of materials by mercury intrusion porosimetry with emphasis on reduction and presentation of experimental data, Micromeritics Instrum. Corp, Norcross, Georg. (2001).

[139] H. Ma, Mercury intrusion porosimetry in concrete technology: tips in measurement, pore structure parameter acquisition and application, J. Porous Mater. 21 (2014) 207–215.

[140] O. Levenspiel, Chemical reaction engineering, John Wiley & Sons, 1999.

[141] H.S. Fogler, S.H. Fogler, Elements of chemical reaction engineering, Pearson Educación, 1999.

[142] T. Baird, J.R. Fryer, B. Grant, Carbon formation on iron and nickel foils by hydrocarbon pyrolysis—reactions at 700 °C, Carbon N. Y. 12 (1974) 591–602.

[143] M. Canal-Rodríguez, N. Rey-Raap, J.Á. Menéndez, M.A. Montes-Morán, J.L. Figueiredo, M.F.R. Pereira, A. Arenillas, Effect of porous structure on doping and the catalytic performance of carbon xerogels towards the oxygen reduction reaction, Microporous Mesoporous Mater. (2019) 109811.

[144] W. Kiciński, M. Bystrzejewski, M.H. Rümmeli, T. Gemming, Porous graphitic materials obtained from carbonization of organic xerogels doped with transition metal salts, Bull. Mater. Sci. 37 (2014) 141–150.

[145] R.W. Pekala, J.C. Farmer, C.T. Alviso, T.D. Tran, S.T. Mayer, J.M. Miller, B. Dunn, Carbon aerogels for electrochemical applications, J. Non. Cryst. Solids. 225 (1998) 74–80.

[146] L. Zubizarreta, A. Arenillas, J.P. Pirard, J.J. Pis, N. Job, Tailoring the

textural properties of activated carbon xerogels by chemical activation with KOH, Microporous Mesoporous Mater. 115 (2008) 480–490.

[147] N. Mahata, M.F.R. Pereira, F. Suárez-García, A. Marinez-Alonso, J.M.D. Tascón, J.L. Figueiredo, Tuning of texture and surface chemistry of carbon xerogels, J. Colloid Interface Sci. 324 (2008) 150–155.

[148] A.M.T. Silva, B.F. Machado, J.L. Figueiredo, J.L. Faria, Controlling the surface chemistry of carbon xerogels using HNO3-hydrothermal oxidation, Carbon N. Y. 47 (2009) 1670–1679.

[149] N. Job, R. Pirard, J. Marien, J.P. Pirard, Porous carbon xerogels with texture tailored by pH control during sol-gel process, Carbon N. Y. 42 (2004) 619–628.

[150] K.Y. Kang, B.I. Lee, J.S. Lee, Hydrogen adsorption on nitrogen-doped carbon xerogels, Carbon N. Y. 47 (2009) 1171–1180.

[151] R.W. Pekala, F.-M. KONG, A synthetic route to organic aerogels-mechanism, structure, and properties, Le J. Phys. Colloq. 50 (1989) C4--33.

[152] D. Salinas-Torres, A.F. Léonard, V. Stergiopoulos, Y. Busby, J.J. Pireaux, N. Job, Effect of nitrogen doping on the pore texture of carbon xerogels based on resorcinol-melamine-formaldehyde precursors, Microporous Mesoporous Mater. 256 (2018) 190–198.

[153] W. Shen, Z. Li, Y. Liu, Surface chemical functional groups modification of porous carbon, Recent Patents Chem. Eng. 1 (2008) 27–40.

[154] M.S. Shafeeyan, W.M.A.W. Daud, A. Houshmand, A. Shamiri, A review on surface modification of activated carbon for carbon dioxide adsorption, J. Anal. Appl. Pyrolysis. 89 (2010) 143–151.

[155] J.R. Pels, F. Kapteijn, J.A. Moulijn, Q. Zhu, K.M. Thomas, Evolution of nitrogen functionalities in carbonaceous materials during pyrolysis,

Carbon N. Y. 33 (1995) 1641–1653.

[156] B. Yang, C. Yu, Q. Yu, X. Zhang, Z. Li, L. Lei, N-doped carbon xerogels as adsorbents for the removal of heavy metal ions from aqueous solution, Rsc Adv. 5 (2015) 7182–7191.

[157] Q. Zhu, S.L. Money, A.E. Russell, K.M. Thomas, Determination of the fate of nitrogen functionality in carbonaceous materials during pyrolysis and combustion using X-ray absorption near edge structure spectroscopy, Langmuir. 13 (1997) 2149–2157.

[158] J. Chen, Z.H. Zhu, S. Wang, Q. Ma, V. Rudolph, G.Q. Lu, Effects of nitrogen doping on the structure of carbon nanotubes (CNTs) and activity of Ru/CNTs in ammonia decomposition, Chem. Eng. J. 156 (2010) 404–410.

[159] A.F. Zainul Abidin, K.S. Loh, W.Y. Wong, A.B. Mohamad, Nitrogen-doped carbon xerogels catalyst for oxygen reduction reaction: Improved structural and catalytic activity by enhancing nitrogen species and cobalt insertion, Int. J. Hydrogen Energy. 44 (2019) 28789–28802.

[160] D.J. Morgan, Resolving ruthenium: XPS studies of common ruthenium materials, Surf. Interface Anal. 47 (2015) 1072–1079.

[161] V. Dimitrov, T. Komatsu, R. Sato, Polarizability, optical basicity and O1s binding energy of simple oxides, J. Ceram. Soc. Japan. 107 (1999) 21–26.

[162] K. Jurewicz, K. Babeł, A. Źiółkowski, H. Wachowska, Ammoxidation of active carbons for improvement of supercapacitor characteristics, Electrochim. Acta. 48 (2003) 1491–1498.

[163] A.K. Bhattacharya, D.R. Pyke, R. Reynolds, G.S. Walker, C.R. Werrett, The use of O1s charge referencing for the X-ray photoelectron spectroscopy of Al/Si, Al/Ti and Al/Zr mixed oxides, J. Mater. Sci. Lett. 16 (1997) 1–3.

[164] F.R. García-García, M. Fernández-García, M.A. Newton, I. Rodríguez-Ramos, A. Guerrero-Ruiz, Following the evolution of Ru/Activated carbon catalysts during the decomposition-reduction of the Ru(NO)(NO3)3 precursor, ChemCatChem. 5 (2013) 2446–2452.

[165] Q. Su, L. Gu, Y. Yao, J. Zhao, W. Ji, W. Ding, C.T. Au, Layered double hydroxides derived Nix(MgyAlzOn) catalysts: Enhanced ammonia decomposition by hydrogen spillover effect, Appl. Catal. B Environ. 201 (2017) 451–460.

[166] L.F. Mabena, S.S. Ray, S.D. Mhlanga, N.J. Coville, Nitrogen-doped carbon nanotubes as a metal catalyst support, Appl. Nanosci. 1 (2011) 67–77.

[167] I.C. Gerber, P. Serp, A Theory/Experience Description of Support Effects in Carbon-Supported Catalysts, Chem. Rev. (2019).

[168] H. Jin, H. Zhang, H. Zhong, J. Zhang, Nitrogen-doped carbon xerogel: A novel carbon-based electrocatalyst for oxygen reduction reaction in proton exchange membrane (PEM) fuel cells, Energy Environ. Sci. 4 (2011) 3389–3394.

[169] L. Perini, C. Durante, M. Favaro, V. Perazzolo, S. Agnoli, O. Schneider, G. Granozzi, A. Gennaro, Metal–Support Interaction in Platinum and Palladium Nanoparticles Loaded on Nitrogen-Doped Mesoporous Carbon for Oxygen Reduction Reaction, ACS Appl. Mater. Interfaces. 7 (2015) 1170–1179.

[170] B. Tomić-Tucaković, D. Majstorović, D. Jelić, S. Mentus, Thermogravimetric study of the kinetics of Co3O4 reduction by hydrogen, Thermochim. Acta. 541 (2012) 15–24.

[171] P. Arnoldy, J.C.M. De Jonge, J.A. Moulijn, Temperature-programed reduction of molybdenum (VI) oxide and molybdenum (IV) oxide, J. Phys. Chem. 89 (1985) 4517–4526.

[172] K.H. Carpenter, G.E. Whorley, T.W. Lennard, Reduction of MoO3 and ammonium molybdates by ammonia in a rotary furnace, (1985).

[173] N. Fischer, E. Van Steen, M. Claeys, Preparation of supported nano-sized cobalt oxide and fcc cobalt crystallites, Catal. Today. 171 (2011) 174–179.

[174] L. Lelong, R. Rastoin, Fuel Cell, (n.d.). https://energies.airliquide.com/resources-planet-hydrogen/fuel-cell#:~:text=PEM fuel cells consume about,for every 100 miles covered. (accessed November 20, 2021).

[175] A.G. Gil, M.H.M. Reis, D. Chadwick, Z. Wu, K. Li, A highly permeable hollow fibre substrate for Pd/Al2O3 composite membranes in hydrogen permeation, Int. J. Hydrogen Energy. 40 (2015) 3249–3258.

[176] V. Cechetto, L. Di Felice, J.A. Medrano, C. Makhloufi, J. Zuniga, F. Gallucci, H2 production via ammonia decomposition in a catalytic membrane reactor, Fuel Process. Technol. 216 (2021) 106772.

[177] P.P. Mardilovich, Y. She, Y.H. Ma, M. Rei, Defect-free palladium membranes on porous stainless-steel support, AIChE J. 44 (1998) 310–322.

[178] Y.S. Cheng, K.L. Yeung, Effects of electroless plating chemistry on the synthesis of palladium membranes, J. Memb. Sci. 182 (2001) 195–203.

[179] T.N. Khoperia, Investigation of the substrate activation mechanism and electroless Ni–P coating ductility and adhesion, Microelectron. Eng. 69 (2003) 391–398.

[180] M. Kitiwan, D. Atong, Effects of porous alumina support and plating time on electroless plating of palladium membrane, J. Mater. Sci. Technol. 26 (2010) 1148–1152.

[181] Ø. Hatlevik, S.K. Gade, M.K. Keeling, P.M. Thoen, A.P. Davidson, J.D.

Way, Palladium and palladium alloy membranes for hydrogen separation and production: History, fabrication strategies, and current performance, Sep. Purif. Technol. 73 (2010) 59–64.

[182] A. Basile, Handbook of membrane reactors: fundamental materials science, design and optimisation, Elsevier, 2013.